Advanced Design and Control Concepts for Actuators Based on Shape Memory Alloy Wires

Dissertation

zur Erlangung des Grades

des Doktors der Ingenieurwissenschaften

der Naturwissenschaftlich-Technischen Fakultät

der Universität des Saarlandes

von

Paul Motzki

Saarbrücken

2018

Tag des Kolloquiums: 04.09.2018

Dekan: Univ.-Prof. Dr. Guido Kickelbick

Berichterstatter/innen: Prof. Dr.-Ing. Stefan Seelecke

Prof. Dr.-Ing. Georg Frey

Prof. Dr. Doron Shilo

Vorsitz: Prof. Dr.-Ing. Rainer Müller

Akad. Mitarbeiter/in: PD Dr.-Ing. Dr. rer. nat. Anne Jung

Kurzfassung

Intelligente Materialien eröffnen durch ihre einzigartigen Formfaktoren ganz neue Designmöglichkeiten und ihre Eigenschaft, Aktorik mit Sensorik zu kombinieren, kann in multifunktionalen Systemen zu bisher ungenutzten Mehrwerten führen. Gleichzeitig führt die hiermit verbundene Komplexität zu neuen Herausforderungen bei der Entwicklung und Ansteuerung von Systemen, sodass es bisher trotz der Vielzahl an Vorteilen noch vergleichsweise wenige kommerzielle Produkte gibt. Diese Dissertation setzt sich als Ziel, diese Herausforderungen zum einen durch die Entwicklung einer systematischen Konstruktionsmethodik als auch durch die beispielhafte Illustration von Konstruktionslösungen anzugehen. Sie konzentriert sich dabei speziell auf das Technologiefeld der Formgedächtnislegierungen (FGL) und erläutert nach einer grundlegenden Einführung in den Entwurf von FGL-Aktorsystemen die intelligente Kopplung von FGL-Aktordrähten mit bistabilen, nichtlinearen Federelementen. Durch diese Kombination lassen sich die oft zitierten Nachteile von FGL – langsame Aktuierung und Energieineffizienz – für viele Anwendungen eliminieren. Ein zweiter Weg zu hoher Geschwindigkeit und Energieeffizienz liegt in der Ansteuerung mit Pulsen bei hohen elektrischen Spannungen.

Zusammenfassend zeigt diese Arbeit innovative und gleichzeitig systematische Konzepte zur Entwicklung von FGL-Aktoranwendungen auf und möchte damit einen Beitrag zur weiteren zukünftigen Verbreitung dieser noch jungen Technologie leisten.

Abstract

Versatility and variability in form factor of smart materials, combined with their actuation and sensing abilities, allow for the design and construction of multifunctional systems. These systems add value to industrial and consumer products. Despite the considerable number of advantages, only a few smart-material-based actuator-sensor-systems are commercially available, mainly due to challenges in design, fabrication, and control of these materials. This dissertation attacks these challenges by providing a systematic design framework, as well as exemplary illustrations of design solutions. Special focus of this work is on the technological field of shape memory alloys (SMA). After a basic introduction to the design of SMA actuator systems, the intelligent combination of SMA actuator wires with bi-stable, nonlinear spring elements is described. This combination eliminates oftentimes-quoted disadvantages of SMAs – slow actuation and energy-inefficiency – for a wide range of applications. A second approach for the realization of high-speed actuation and energy-efficiency is the activation of SMA wires with high voltage pulses, which leads to actuation times in the millisecond-range and energy-savings up to 80 % in comparison to the suppliers' recommendations.

In summary, this thesis demonstrates innovative, and at the same time systematic concepts for the design and control of SMA actuator systems. Thus, it aims at contributing to future spreading of this still young technology.

Der erste Schluck aus dem Becher der Wissenschaft führt zum Atheismus,
aber auf dem Grund des Bechers wartet Gott.

Werner K. Heisenberg
(1901-1976)

To Stephanie Akua, Maureen Akosua, and Zola Afia.

Acknowledgements

I would first like to acknowledge my wife Stephanie for supporting me through all these years. Her efforts and accomplishments cannot be put in words, allowing me to pursue my academics aside my passion for athletics and at the same time starting a family and gifting me with two wonderful and lovely daughters. At this point, I owe thanks to my parents and siblings, my uncle and aunt Harald and Brigitte, my mother-in-law as well as my brother-in-law and sister-in-law and their families for making our family life as desirable as it can be.

At our lab, I must give thanks to Alex York for giving me an easy start into my doctoral project. Also, thanks go to all my co-workers and my student research assistants who all contributed to the results of this dissertation, especially Benedikt Holz, Thomas Würtz, Marvin Schmidt, Julian Kunze and Dominik Scholtes to only name a few.

Special thanks go to Steffen Hau and my uncle Harald for reviewing my early drafts of this work and to Prof. Georg Frey for agreeing to oversee my defense and review this dissertation.

Finally, I would like to thank Prof. Stefan Seelecke for giving me the opportunity to work and pursue my PhD at his lab and giving me full trust from the very start. The flexibility and freedom I was granted during my time as a PhD student as well as his advice and guidance paved the way to my success in my academic and all my non-academic areas of life.

Table of Contents

1   Introduction

In times of the next industrial revolution and the general widespread demand for more functionality in products, engineers are faced with more complex and challenging tasks. On the one hand, "Industry 4.0" stands for the digitalization of manufacturing processes and includes automation, cyber-physical systems, the Internet of Things and further technologies for assembly assistance like human-robot-cooperation, on the path to more flexible and adaptive "smart factories". On the other hand, commercial products in the fields of consumer electronics, household and domestic appliances, biomedicine, automotive and aerospace aim to add more functionality to generate added-value in comparison to competitors. For the realization of novel or improved products, more and more engineers start looking into smart materials to replace state-of-the-art actuators or sensors or to design new multifunctional actuator-sensor-systems. These smart or active materials like shape memory alloys (SMAs) or electro-active polymers (EAPs) change their properties in response to external fields, which can either be exploited to produce movement and force for actuation or for quantitative sensor measurements. Aside from their multi-functionality, smart materials can offer significant savings in weight and construction space because of their high energy and power densities. Smart material actuator systems oftentimes offer very energy-efficient solutions in comparison to electric, electromagnetic, hydraulic or pneumatic actuators and operate without noise and emissions. Even further, completely new actuator designs and implementation become possible due to the materials' specific and flexible form factors. Current topics of interest such as predictive maintenance and condition monitoring can be addressed by using the sensing abilities in smart material actuators and even further, this "self-sensing" may be utilized in position control algorithms without the use of external sensors.

Despite all of the mentioned benefits, there are only relatively few established products on the market using smart material actuators or sensors. Shape memory alloy technology has been known for decades and the manufacturing processes of SMA material have become very reliable. Especially nickel-titanium (NiTi, Nitinol) is nowadays produced with consistent properties such as phase transformation temperature and transformation strain. SMA components are commercially available at reasonable cost and some commercial applications have already proven their functionality and durability in operation. Several reasons the implementation of SMA actuators in applications is still not more widespread

are challenges in design and fabrication with SMA wires because of their non-linear and hysteretic thermo-mechanical material properties. Additional challenges come with the control of SMA actuator systems, as there are no standardized power electronics available for these materials. Finally, drawbacks of SMA actuators like their limited stroke, low frequency or energy-inefficiency lead to engineers still preferring state-of-the-art actuators like electric or pneumatic drives.

The objectives of this dissertation are to provide methods and guidelines for the design and fabrication of SMA actuators, and to eliminate the drawbacks of frequency limitations, low stroke output and poor energy-efficiency by an advanced actuator design and an alternative control concept. The two applications of an SMA vacuum gripper and an SMA robotic end-effector are used as case studies for the design and fabrication of SMA linear and rotary actuators. In the following, an advanced SMA actuator design using bi-stable spring elements is introduced. This advanced concept allows the design of energy-efficient, high-frequency SMA actuators with high output strokes. The last chapter focuses on an advanced control method, which also leads to very fast and energy-efficient actuation by using high-voltage pulses for the SMA wire activation. This high-speed activation turns out to result in stroke output enhancements as well.

2 Fundamentals

The material category of shape memory alloys can be divided into the two sub-categories of thermal shape memory alloys (SMA) and (ferro-)magnetic shape memory alloys (FSMA, MSM). This dissertation focuses exclusively on actuator design using thermal shape memory alloys. The following chapter is oriented on [1]–[6].

2.1 Thermal Shape Memory Alloys

The first reported observations of a shape memory effect go back to 1932, when the Swedish physicist Arne Ölander discovered a "rubberlike" behavior on an Au-47.5Cd alloy [7], [8]. The actual term "shape memory effect" was first used by Chang and Read in 1951 [9], [10]. In 1963, the U.S. Naval Ordinance Laboratory published first investigations of the shape memory effect in binary nickel-titanium [11]. Nickel-titanium (NiTi, Ni-Ti, Nitinol) since has emerged as the most popular shape memory alloy for technical use because of its good mechanical properties such as high mechanical strength, corrosion resistance and biocompatibility [4], [7], [12]–[15].

The thermal shape memory effect (SME) describes the ability of a material to "remember" its initial form and return to it, even after strong deformation [3], [16], [17]. The underlying mechanism is a reversible phase transformation. The SME can be observed mainly in metallic alloys, but is also present in ceramics (e.g. ZrO_2) and polymers (e.g. PTFE) [12], [16], [18].

Metallic shape memory alloys (SMAs) undergo a stress- and temperature-induced phase transformation from a cold temperature phase called martensite to a high temperature phase called austenite [2], [16], [19]. These changes of the crystal lattice structure in the microscale lead to macroscopic changes of the material properties and physical shape [20], [21]. In the austenite phase (A), the crystal has a body centered cubic lattice (BCC), as shown in Figure 2.1. The martensite phase in contrast shows monoclinic crystals [12], [22]. These crystals can have two orientations and are referred to as martensite plus (M^+) and martensite minus (M^-). In absence of external loads, these two crystal orientations form a twinned martensite. If an external load is applied, the martensite can be detwinned and the crystals are flipped. A pulling force for example can lead to configuration of 100 % M^+, which would also be visible in a macroscopic "quasi-plastic" elongation. This example and other possible effects are illustrated in Figure 2.2. The three basic effects that can be

observed in SMAs are the One-Way SME, the Two-Way SME and the effect of "Pseudoelasticity". These effects will be explained in more detail below. Figure 2.2 also shows that phase transformation can be induced by mechanical stress or by temperature.
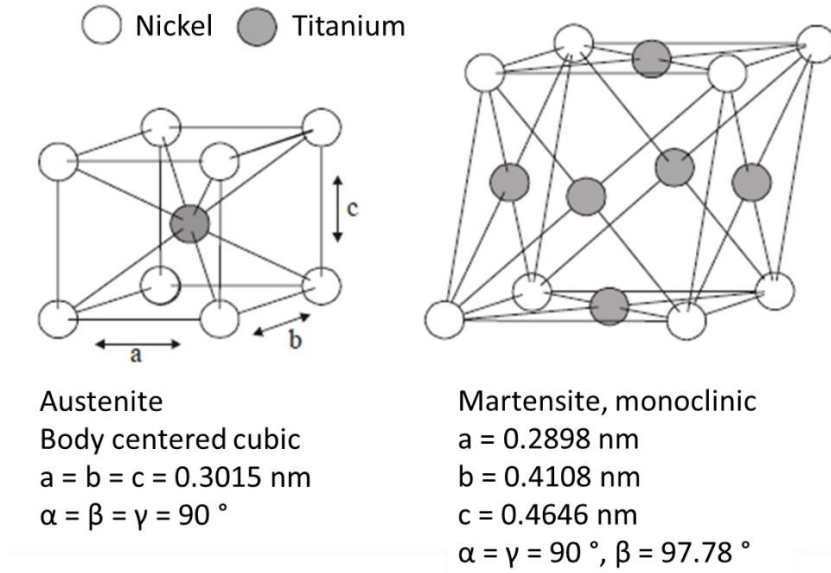

Figure 2.1: Crystal lattice structures of NiTi in its martensite and austenite phase [12].
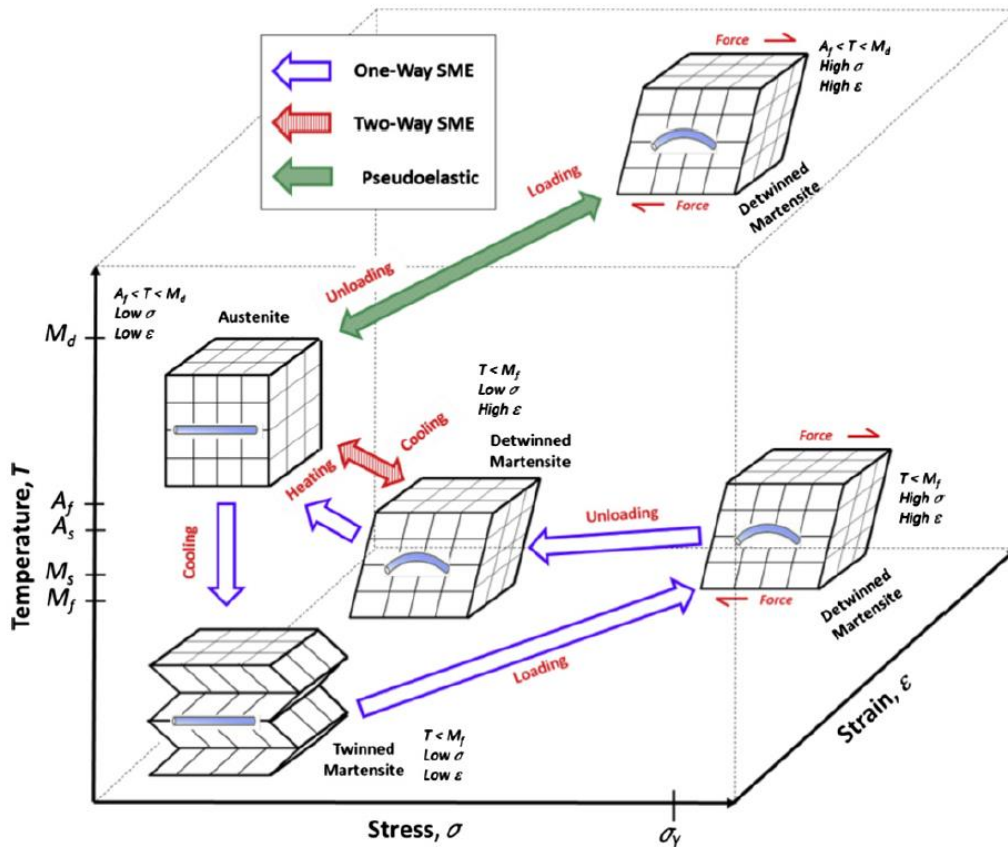

Figure 2.2: Schematic of different SMA crystal lattices and possible phase transformations [18].

The temperature induced phase transformation from martensite to austenite is described by four characteristic temperatures (Figure 2.3). The transformation from martensite to austenite starts at the temperature A_s (austenite start) and is completed at A_f (austenite finish). The reverse transformation through cooling is characterized accordingly by the temperatures M_s (martensite start) and M_f (martensite finish). The SMA material is completely austenitic at temperatures above A_f and fully martensitic at temperatures below M_f. The region between those two temperatures is characterized by temperature dependent volume fractions of both phases. The reversible temperature induced phase transformation shows a hysteresis in the order of 10-50 K [4].
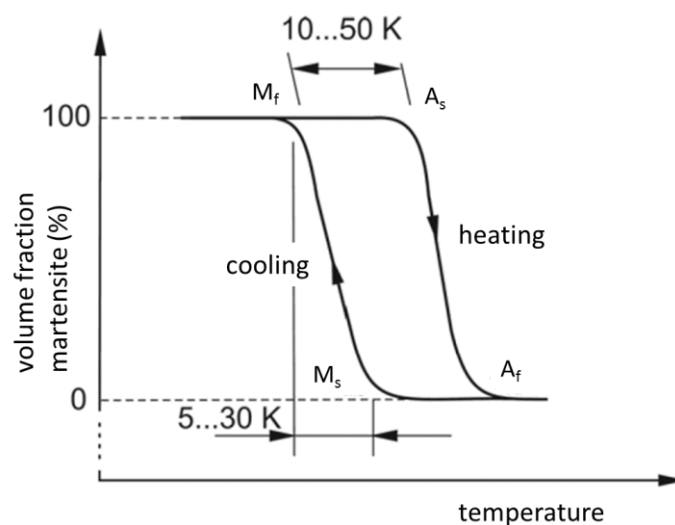

Figure 2.3: Characteristic temperatures for a phase transformation from martensite to austenite [4], [17].

2.1.1 One-Way SME

Below the temperature M_f, deformations up to a critical level lead to a reversible martensite transition from twinned martensite to a detwinned configuration. These deformations are called "quasi-plastic", because the SMA material remains in its detwinned (deformed) state even without external forces. Heating of the SMA above the temperature A_f brings the material back to its original shape in the austenitic phase. If the ensuing cooling phase takes place under load-free conditions, the crystal lattice will return to a twinned martensite but without any change of the macroscopic shape. In summary, the SMA "remembers" its initial shape when heated, but does not perform any shape change during cooling. That is the reason for this effect being referred to as the One-Way SME [3], [4], [23].

The characteristic behavior is illustrated in Figure 2.4. Point ① describes the load-free, twinned martensite phase. Applying an external force leads to an elastic deformation until ② is reached. Between ② and ③, the detwinning takes place as the result of increasing stress. The subsequent relaxation results in a residual deformation (point ④). Heating of the SMA leads to a phase transformation to austenite between points ⑤ and ⑥ and the material returns to its original shape, before transforming back to twinned martensite (point ①) upon cooling down.
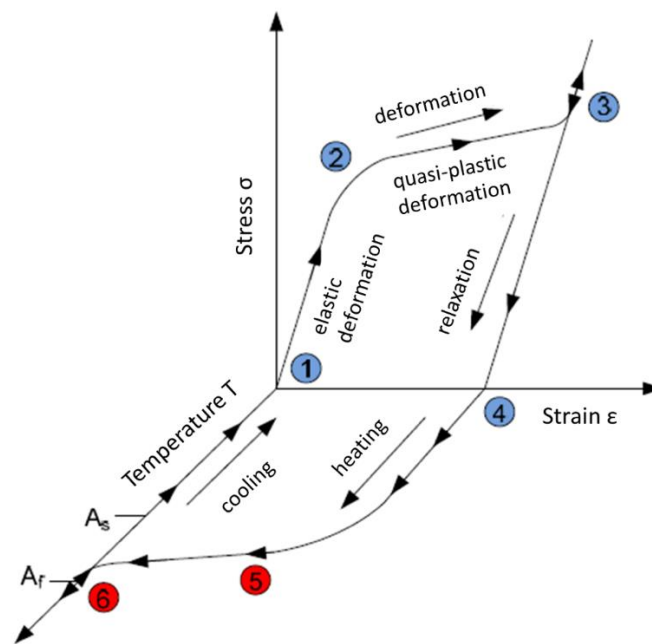

Figure 2.4: Stress-strain-temperature diagram for the One-Way SME [3].

2.1.2 Two-Way SME

In contrast to the One-Way SME, the Two-Way SME describes the ability of SMA material to "remember" a certain shape in its austenitic high temperature phase and also in its martensitic cold temperature phase. A distinction is made between intrinsic and extrinsic Two-Way SME.

The intrinsic Two-Way SME is based on internal stresses caused by lattice defects or dislocation structures. These lead to a preferred martensite configuration in the cooled down state, which can be very different from the twinned martensite with 50 % M^+ and 50 % M^-. Lattice defects can be purposefully generated by irreversible plastic deformation or by so-called training, which e.g. can be a cyclic heating under defined mechanical stress [3], [4].

The extrinsic Two-Way SME can be described as a continuous repetition of the One-Way SME. An external load like a weight or a spring force is used to constantly generate deformation in the martensitic phase, so that temperature cycling causes a transition between defined states in each of the two phases (Figure 2.5).

As in Figure 2.4, point ① describes the initial state of twinned martensite. The external load leads to an elastic deformation (point ②) and an ensuing quasi-plastic deformation through detwinning of the martensite (point ③). Now, instead of returning to a stress-free state, the external force stays present and the SMA is heated. The phase transformation to austenite starts at point ④ and is finished at point ⑤. Because of the external load, cooling of the SMA does not result in a twinned martensite configuration, instead the material returns to the deformed martensitic state in point ③. Repeated heating and cooling results in cycling between points ③ and ⑤.
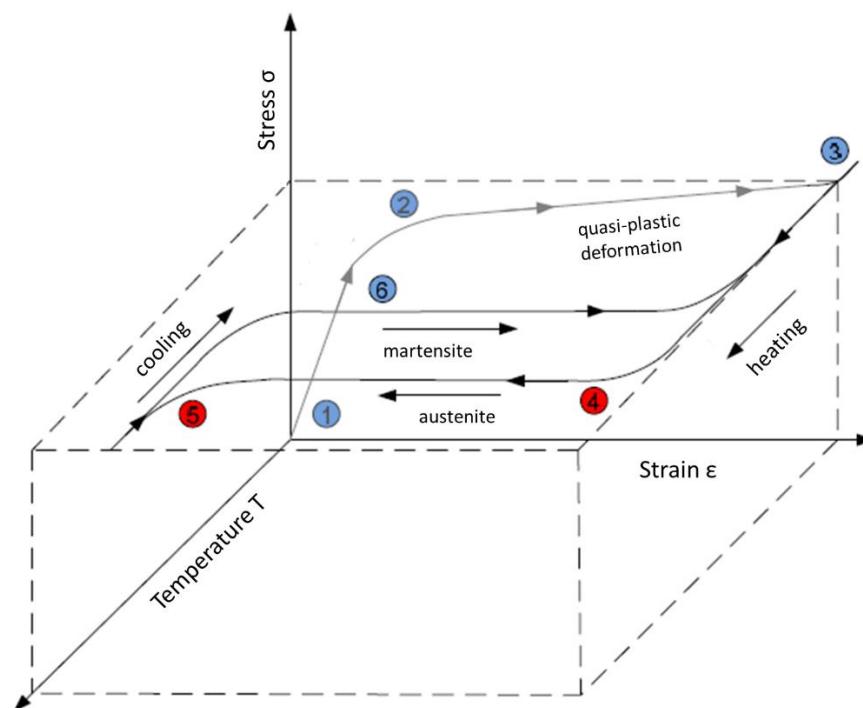

Figure 2.5: Stress-strain-temperature diagram for the extrinsic Two-Way SME [3].

2.1.3 **Pseudoelasticity**

The pseudoelastic effect describes stress-induced phase transformation without an externally driven heating and cooling of the SMA material. The typical transition temperature A_f of an SMA depends on its alloy composition. There are SMAs with a transformation temperature A_f below room temperature, which leads to an austenitic crystal

structure in a load-free configuration. Applying an external force leads to a phase transformation into martensite, which comes along with material strains up to 12 % without any plastic deformation. That is why these SMAs are also called "superelastic" [4], [23]. If the external force is removed, the SMA will return to its initial configuration in the austenite phase. Higher temperatures lead to higher stresses for the martensitic phase transformation. The pseudoelastic effect is schematically demonstrated in Figure 2.6. The initial material configuration is defined by a load-free state in the austenite phase (point ①). Applying an external force first leads to elastic deformation until point ②. If the force is increased further, the martensitic phase transformation takes place until point ③ is reached. Beyond point ③, the SMA has transformed to an oriented martensite phase. Increasing forces from this point lead to an elastic deformation with a different Young's modulus, a relaxation on the contrary lead to phase transformation back to austenite, which starts in point ④ and ends in the initial starting configuration (point ①).
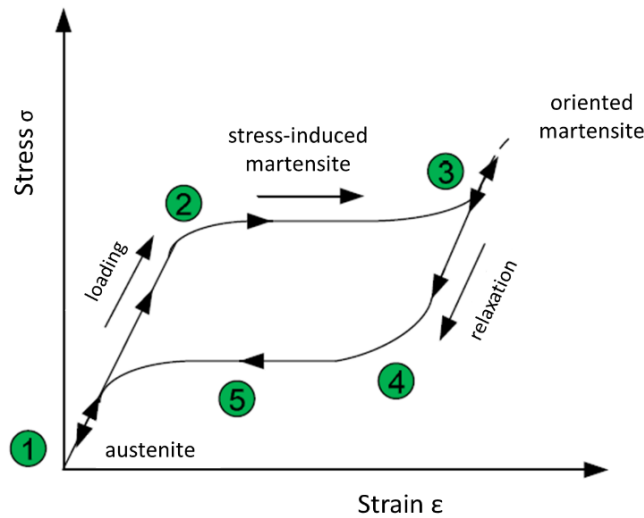

Figure 2.6: Stress-strain diagram for Pseudoelasticity [3].

2.1.4 Self-Sensing

While the contraction of an activated SMA wire can be used for actuator design, the temperature induced phase transformation also results in a change of the wire's electrical resistance. The resistance R_{SMA} of an SMA wire can be calculated with the linear approximation:

$$R_{SMA}(T) = \rho_{NiTi}(T) \cdot \frac{l_{SMA}(T)}{A_{SMA}(T)} \cdot \left(\alpha_{NiTi} \cdot (T - T_0) + 1 \right). \tag{2.1}$$

The specific electrical resistivity $\rho_{NiTi}(T)$ depends on the fractions of martensite and austenite since their specific resistivity is slightly different. However, the geometrical changes of the SMA wire during the transformation to austenite dominate the resistance behavior as the SMA wire length l_{SMA} decreases and its cross section A_{SMA} increases. Finally, the electrical resistance of metals changes with temperature, which is described by the temperature coefficient of resistivity α_{NiTi}. Note, that α_{NiTi} is an empirical parameter only valid for a small temperature range around the reference temperature T_0. Figure 2.7 shows the qualitative behavior of the electrical resistance for the thermal activation of an SMA wire. First, the resistance increases because of the increase in temperature (section a). When the phase transformation and the contraction of the SMA wire start, the geometrical changes dominate and the resistance decreases (section b). After complete phase transformation, the resistance starts to increase again, if the SMA wire is heated further (section c). This resistance behavior also explains the different shapes of the stress-strain characteristics in Figure 2.8. If the SMA wire is activated at a constant voltage (left-hand side), the increase of its electrical resistance during the phase transformation from austenite to martensite leads to a decrease in electrical power and thus temperature. A lower temperature is indicated by a decrease in mechanical stress during the transformation. In contrast, if the electrical current is constant during activation (center), the electrical power increases even more during the transformation to martensite because of the increasing resistance. The increase in mechanical stress during the transformation indicates a temperature increase. To guarantee a constant temperature during the phase transformation, the electrical power input has to be held at a constant level (right-hand side).
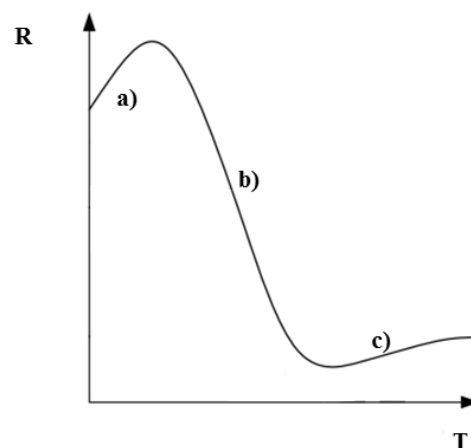

Figure 2.7: Schematic of the SMA wire's electrical resistance R behavior in relation to its temperature T [17].
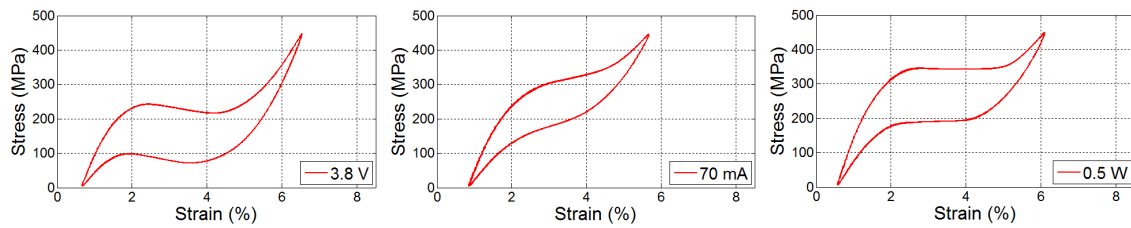
Figure 2.8: Stress-strain diagrams for a 76 µm wire at constant voltage (left-hand side), at constant current (center) and at constant power (right-hand side) [24].

The change of resistance during phase transformation can be used for sensing purposes. This multifunctionality of combined actuator- and sensor-capabilities is typical for so-called "smart materials" and is often referred to as "Self-Sensing". Self-Sensing means, that there is no need for additional sensors in an application to provide monitoring of the actuator functionality. Even further, the Self-Sensing in SMA wires can be utilized for feedback control algorithms. As illustrated in Figure 2.9, despite the hysteretic mechanical behavior of SMA wires, the resistance shows a near linear relationship to the wire contraction during the phase transformation. That means, that the SMA wire length can be directly linked to a certain electrical resistance, which can be used for position control of SMA actuators [25]–[30].
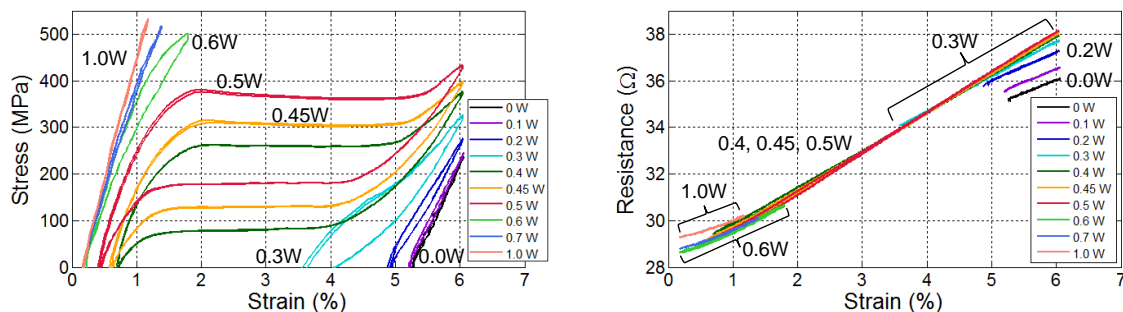

Figure 2.9: Stress-strain characteristics for different constant power values and related resistance-strain characteristics of a 76 µm SMA actuator wire [24].

2.2 SMA Applications

Because of their benefits regarding construction space, weight and the possibility of completely new actuator design, SMA actuators have found their way into a number of applications [31]. The company Actuator Solutions GmbH (ASG) is a specialist for mass production of SMA actuator components. Their focus is on the areas of miniaturized optical camera systems and pneumatic and fluidic valves. Their fully automated production lines produce more than 10 million SMA actuators per year [32], [33]. Besides this exceptional example, SMA actuators have also become very popular in the fields of industrial-,

automotive-, biomedical-, aerospace- and MEMS applications [34]–[73]. The industrial and automotive sectors are looking into SMA solutions for robotics and work piece manipulation [60]–[62], [65], [72], [74]–[77]. Especially light-weight grippers based on SMA actuators are of special interest [63], [64], [78]–[84]. In analogy to the human body, a lot of these grippers use a humanoid finger design, in which SMA wires are used like muscle fibers [36], [38], [39], [85]–[89]. Aside from industrial applications, these grippers are subject to research for biomedical products like hand prostheses. Other bio-inspired applications that use SMA wires as metal muscles include imitations of a fish [73], a jellyfish [90], [91] an earthworm [37] or a bat [35], [46], [57], [68], [92]. Because of the biocompatibility of Nitinol, SMAs are very popular in the biomedical sector. Although the majority of biomedical applications uses super-elastic SMAs for example in stents [42], there are several interesting applications for actuator wires, like catheters or inhalation systems [34], [43], [44], [54], [55], [69], [70]. The high energy density and miniaturizability of SMAs has led to several applications in the MEMS field [40], [41], like microgrippers [12], [93], [94], microvalves [49] and thin-film based actuators [23], [45], [47], [52].

In this work, two applications in the field of industrial gripping and material handling are used as case studies for applied SMA actuator design. An SMA based vacuum gripper system and an SMA reconfigurable robotic end-effector are used as examples for systematic design approaches for linear and rotary SMA actuators.

3 Applied SMA Actuator Design – Linear Spring Systems

Essential work in the fields of design and fabrication with SMA actuator wires has been presented in [95]. The examples used in [95] focus on the use of SMA wires in flexure hinges. In these bending configurations, the flexures are utilized as the returning mechanism for the SMA wires. Commercial state-of-the-art SMA actuators usually rely on a system consisting of an SMA wire working against a linear spring. This chapter presents design routines including graphical methods at the example of two case studies. The exemplary SMA actuators have been chosen from the fields of material handling and industrial gripping which have gained considerable relevance in recent years [94], [96], [97]. It is shown, how linear as well as rotary actuator principles can be realized with linear spring systems and how the critical properties output stroke, energy-efficiency and actuation frequency can be addressed by design.

3.1 SMA Actuators

This work focuses on actuator design based on SMA wires as the core component. Essential work in the field of actuator design and fabrication based on SMA wires has been described in [95], [98]–[105]. SMA actuator wires (NiTi wires) have the highest energy density of all known actuator components [43], [66], [67], [89], [90], [93] on the order of 10^7 J/m^3 [4] and a power density on the order of 50 kW/kg [74]. The thermal activation of SMA wires in technical applications is realized through Joule heating by an electric current. A defined electric current heats up the SMA wire to typical transformation temperatures of 70 °C or 90 °C and the transition to the austenitic phase causes a 3-5 % contraction of the SMA wire [14], [15]. This implies that the SMA wire has to be pre-stretched by an external load to enable repeated actuation. Typical bias mechanisms for actuators are mechanical springs or a second SMA wire in an antagonistic configuration. Because of the hysteretic material characteristics of SMA wires, the understanding of the interaction of the SMA wire with the restoring spring element is crucial for the design of a functional actuator. After activation, the SMA wire has to cool down before the restoring element stretches it again, so that it is ready for the next activation. This usually passive cooling by convective airflow is the limiting factor for the maximum actuator frequency. The cooling time of an SMA wire is directly related to its diameter, because the diameter defines the surface-to-volume ratio of the wire. This means that thinner SMA wires cool faster and thus are able to operate at higher frequencies. The second often-mentioned disadvantage of high energy

consumption refers to applications, in which the SMA wires have to stay activated and thus heated for longer time intervals.

For the design of SMA actuators, a systematic approach, which is based on a solving quasi-static problem, is used. The concept always follows three steps:

(1) **Kinematic study of all system elements**

(2) **Study of the system kinetics including free body diagrams and equations of the equilibrium of forces**

(3) **Determination of the design parameters using the specific material characteristics and graphical methods**

A simple system of an SMA wire coupled with a mechanical spring and mass m is chosen as an example to showcase the system interaction and the role of the SMA hysteresis [106], using the systematic approach introduced above. First, an SMA wire is stretched quasi-plastically for $x_{SMA,0}$ to reach a state of 100 % M$^+$. It is then put into a mechanically parallel configuration with a linear spring. At room temperature T_0, this configuration is stress-free. In a next step, a mass m is added, which further stretches both the SMA wire and the linear spring (Figure 3.1).
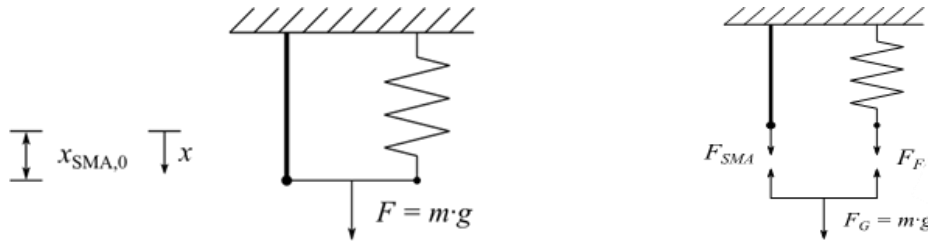

Figure 3.1: Generalized structure of an SMA actuator system containing a linear spring and a mass. The schematic is used to illustrate the free body diagram and the equilibrium of forces [106].

Kinematic Study

The kinematic study of the system leads to

$$x = x_{SMA} = x_F$$
$$\Delta x_{SMA} = \Delta x_F = x - x_{SMA,0}.$$

(3.1)

Kinetic Study

The system is described by the equilibrium of forces

$$\sum F = 0 \rightarrow F_{SMA} = F_G - F_F \tag{3.2}$$

with

$$
\begin{aligned}
F_G &= m \cdot g \\
F_{SMA} &= f\left(x_{SMA}, T\right) \\
F_F &= k \cdot \Delta x_F.
\end{aligned}
\tag{3.3}
$$

With the determined kinematic relations, all the forces can be calculated in relation to variable x:

$$
\begin{aligned}
F_G &= m \cdot g \\
F_{SMA} &= f\left(x, T\right) \\
F_F &= k \cdot \left(x - x_{SMA,0}\right).
\end{aligned}
\tag{3.4}
$$

Determination of the Design Parameters

For a clear illustration, the resulting stress-temperature diagram $\sigma(T)$ and strain-temperature diagram $\varepsilon(T)$ are determined with a graphical solution. These diagrams are used to determine output stroke and forces of a desired actuator system. For simplification, a perfect single crystal SMA characteristic is used. To demonstrate the influence of the SMA wire pre-strain, two different cases are described.

In case 1, the spring-mass characteristic intersects the SMA characteristic above the hysteresis at room temperature T_0 (Figure 3.2 a). In this state, the SMA is fully martensitic (M$^+$). The SMA wire is then heated to temperature $T_1 > T_0$ (Figure 3.2 b). The transformation stress increases proportionally with the temperature and the size of the hysteresis stays constant. The equilibrium intersection is point ① and the SMA wire is still 100 % martensitic. Further heating to $T_2 > T_1$ (Figure 3.2 c) triggers the phase transformation to austenite. The equilibrium intersection is point ① and the SMA wire is partially martensitic and austenitic. The intersection point in Figure 3.2 (d) describes the fully austenitic SMA wire at $T_3 > T_2$. In the ensuing cooling phase, the SMA wire's temperature is reduced to $T_4 = T_2$, but the intersection is at point ②, still in a fully austenitic state (Figure 3.2 e). At $T_5 = T_1$, the intersection at point ② runs along the upper limit of the hysteresis and transformation from austenite to martensite (M$^+$) takes place (Figure 3.2 f),

before the initial fully martensitic state is reached at $T_6 = T_0$ (Figure 3.2 g). The identified intersection points can now be transferred into the strain-temperature diagram $\varepsilon(T)$ and stress-temperature diagram $\sigma(T)$. As shown in Figure 3.3, the actuator system alternates reversibly between an activated and a deactivated state with a temperature hysteresis.
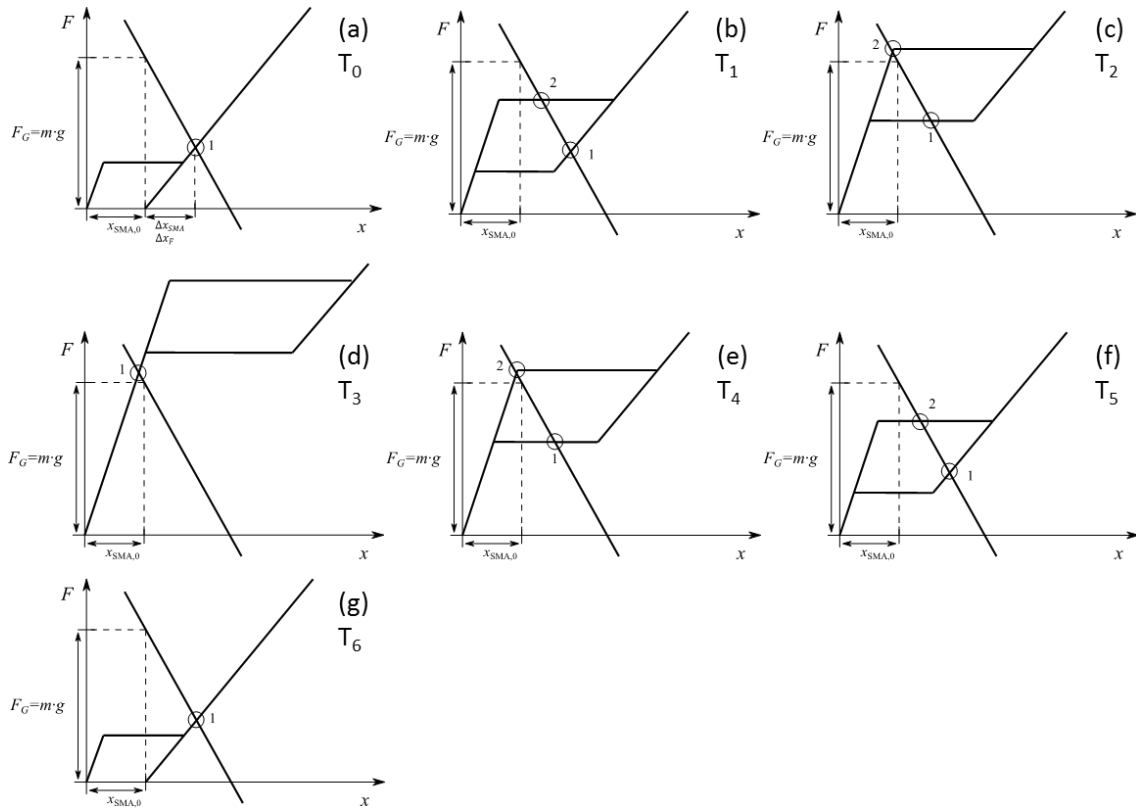

Figure 3.2: Force-displacement equilibrium between a single crystal SMA wire and a spring-mass characteristic during thermal loading and unloading. SMA pre-stress is higher than the upper limit of its hysteresis [106].
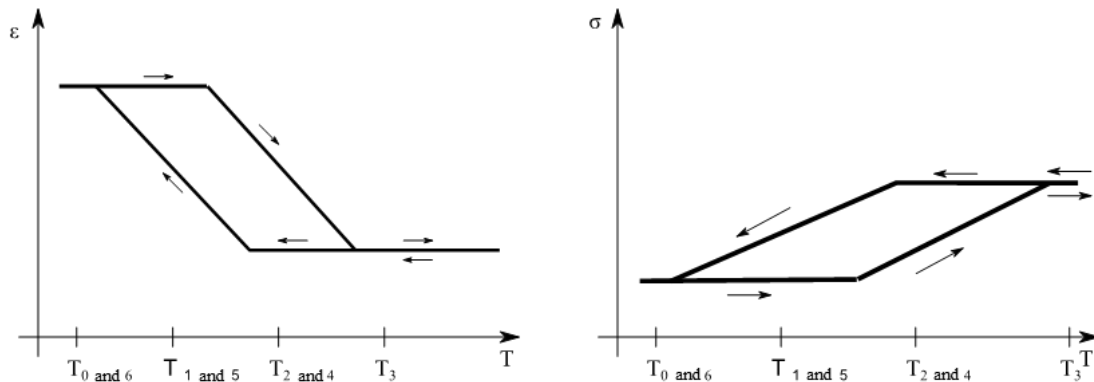
Figure 3.3: Strain-temperature diagram $\varepsilon(T)$ and stress-temperature diagram $\sigma(T)$ for an SMA actuator system with a linear spring. SMA pre-stress is higher than the upper limit of its hysteresis [106].

In case 2, a lower mass m is used so that the spring-mass characteristic intersects the SMA characteristic below the upper limit of the hysteresis at room temperature T_0 (Figure 3.4 a). The SMA wire is fully martensitic (M^+). At $T_1 > T_0$ and $T_2 > T_1$, the intersection is at point ① on the lower limit of the hysteresis and the SMA wire is partially martensitic and austenitic (Figure 3.4 b and c). Heating up to $T_3 > T_2$ leads to a complete phase transformation to austenite (Figure 3.4 d).
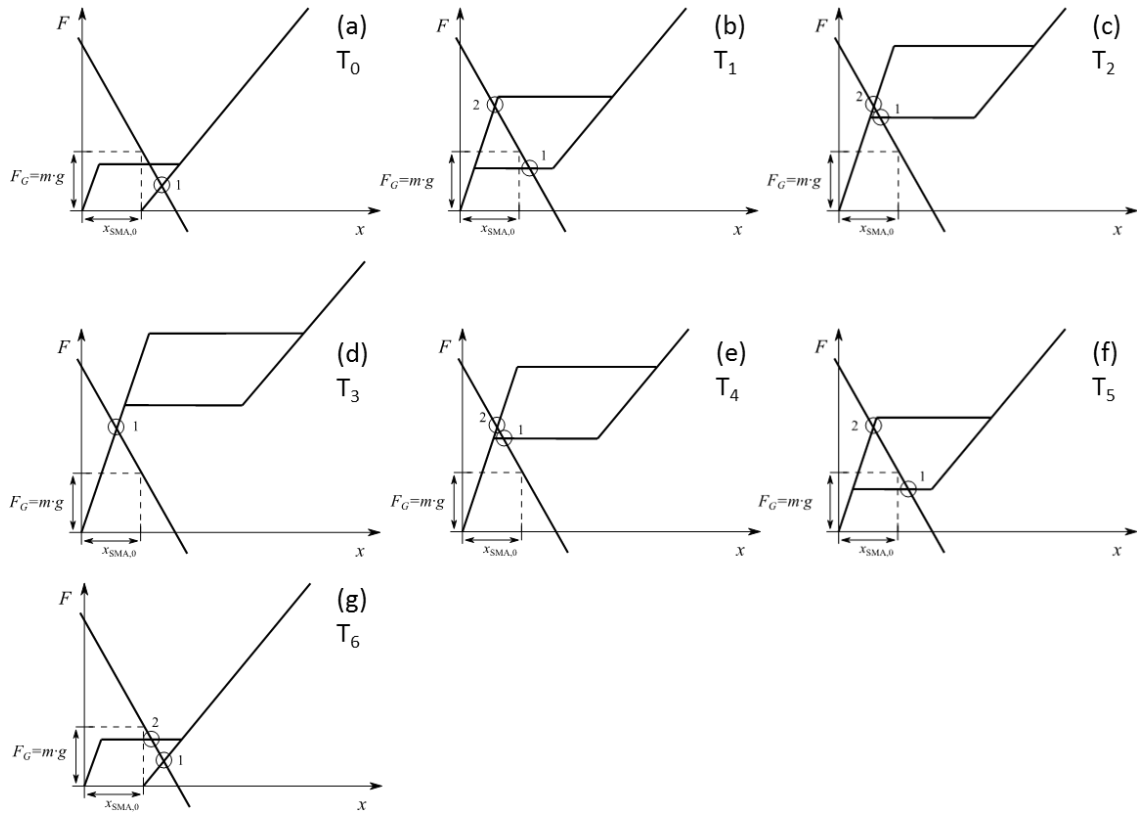

Figure 3.4: Force-displacement equilibrium between a single crystal SMA wire and a spring-mass characteristic during thermal loading and unloading. SMA pre-stress is lower than the upper limit of its hysteresis [106].
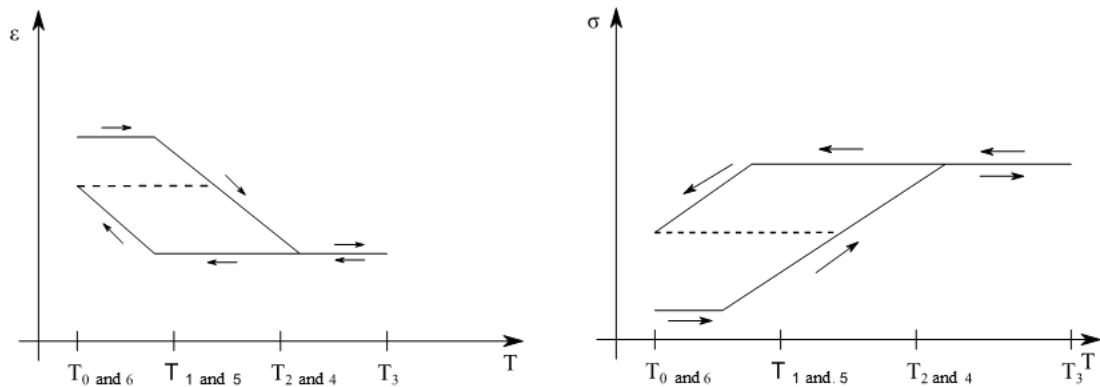

Figure 3.5: Strain-temperature diagram $\varepsilon(T)$ and stress-temperature diagram $\sigma(T)$ for an SMA actuator system with a linear spring. SMA pre-stress is lower than the upper limit of its hysteresis [106].

During the cooling, the intersection is always at point ②, so that at $T_4 = T_2$ and at $T_5 = T_1$, the SMA wire is still fully austenitic (Figure 3.4 e and f). Further cooling to room temperature $T_6 = T_0$ does not lead to a complete transformation back to M$^+$, as Figure 3.4 (g) indicates. The intersection stays at point ② and the initial starting point ① is not reached anymore. The resulting strain-temperature diagram $\varepsilon(T)$ and stress-temperature diagram $\sigma(T)$ are displayed in Figure 3.5. The system is unable to reach its initial starting values after one temperature cycle. This example illustrates the effect of the hysteresis in combination with the bias system in an SMA actuator. If the pre-stress of the SMA wire is too low, the actuator is going to lose actuation strain after the first activation cycle.

It should be noted that the force-deformation curves in Figure 3.2 and Figure 3.4 are assuming a perfect single-crystal SMA material. In reality, an SMA wire has a polycrystalline structure, containing many crystals with different orientations and properties. This fact leads to smoother transitions for the phase transformation as shown in the sample curves in Figure 3.6.
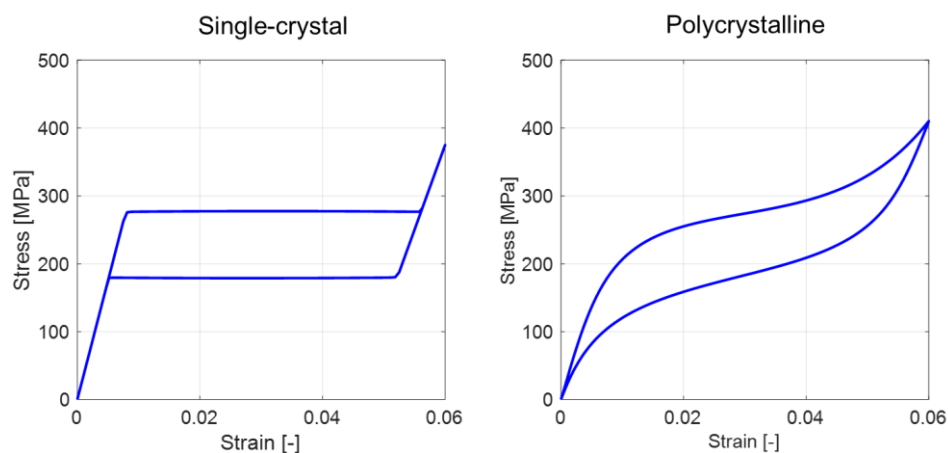

Figure 3.6: Single-crystal approximation vs. polycrystalline SMA material behavior.

3.2   Design Example 1: SMA Suction Cup

In material handling and assembly industry, vacuum grippers are widely used for the handling of plane work pieces [107]. State-of-the-art vacuum gripper systems use the Venturi effect for vacuum generation, so they need a continuous supply of energy from a central compressed air system [108]. Oftentimes, these compressed air systems are one of the biggest cost factors in production. With an SMA based system, there is no need for pressured air, which results in significant savings in energy and thus expenses. Additionally, further advantages of the SMA technology including lowered noise level, unaffected air quality and lowered system costs, weight and dimensions can be exploited.

The original idea and the first prototype of an SMA based suction cup has been presented in [64]. In this concept, an SMA wire is used to actively deform a flat membrane and thus create a vacuum between said membrane and a plane surface (Figure 3.7, left-hand side). The two disadvantages of SMA wire actuators explained in section 3.1 apply to this first suction cup concept as well. After gripping and while holding a work piece, the SMA wire is constantly activated and energy is lost as heat to the environment. The actuation frequency of this prototype is also very limited because the SMA wire takes several seconds to cool down. The improved prototype presented in this chapter attacks these disadvantages by using a different kinematic concept in combination with a thinner SMA wire diameter. The improved kinematic concept is displayed in Figure 3.7 (right-hand side). In the suction cup's initial state, the membrane is already deformed by the linear spring. Activation of the SMA wire forces the membrane into a flat configuration ready to grip a work piece. In this concept, the SMA wire is only activated for a pulse before gripping and to release a work piece and no energy is lost during the holding phase. By winding the SMA wire between the upper and lower fixture multiple times, the forces of all mechanically parallel SMA wire sections add up and a smaller SMA wire diameter can be chosen, which improves the dynamic behavior of the actuator. This section is mainly based on [60], [63], [64], [72], [75], [109], [110].
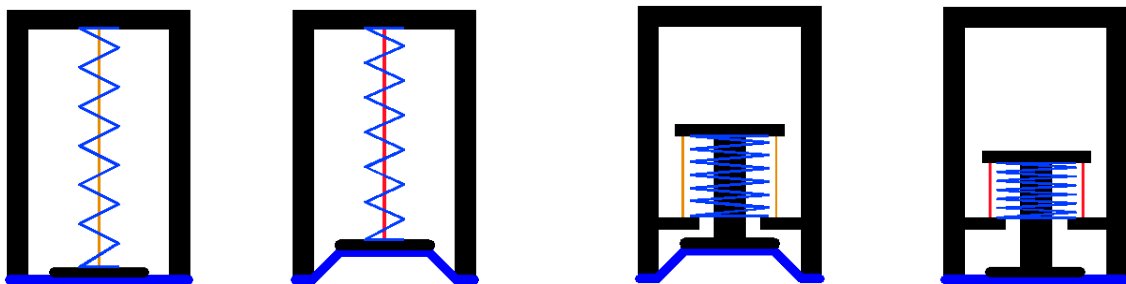

Figure 3.7: Two kinematic concepts for SMA based suction cups. Either the SMA wire actively deforms the flat membrane and creates a vacuum (left-hand side) or the linear spring is used for the vacuum generation (right-hand side) [110].

3.2.1 Suction Cup Design and Manufacturing

The improved prototype of the SMA suction cup is introduced in this section, starting with an introduction of the overall system followed by a description of the actuator assembly. The main part focuses on the systematic design process including the system kinematics, an equilibrium of forces, as well as the force-displacement characteristics. Based on this physical system description and target specifications for resulting vacuum forces and actuator frequencies, the desired combination of SMA wire and linear spring can be selected.

3.2.1.1 **Overall System Description**

The prototype design of the SMA suction cup is shown in Figure 3.8. The membrane is connected to the lower fixation, which is also used for mechanical connection via a screw thread to a gripping mechanism like a robotic end-effector. The membrane is connected to the upper fixation with a threaded rod. The two nuts in the upper fixation are used to adjust the membrane's relative position to guarantee a flat state of the membrane when the SMA wires are activated. The compression of the spring between the upper and the lower fixation is adjusted with two adjustment screws. The mechanically parallel configuration of the SMA wire is realized by winding of a single SMA wire between the upper and the lower fixation.
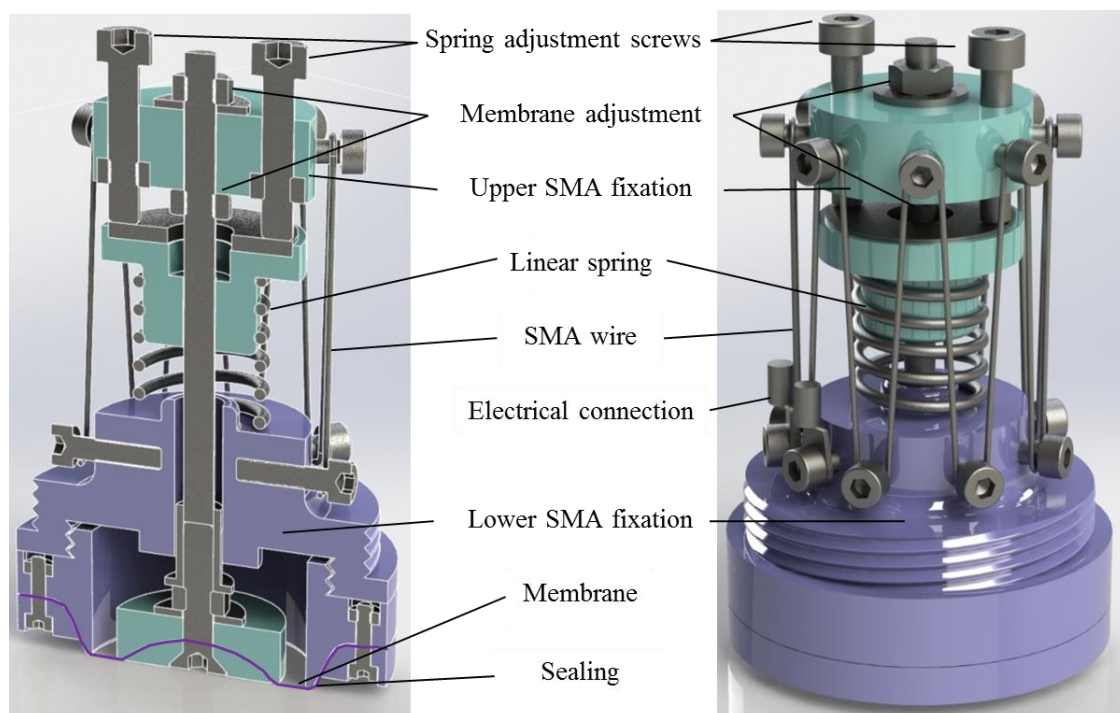

Figure 3.8: CAD model of the SMA suction cup prototype.

3.2.1.2 **SMA Actuator Assembly**

To guarantee reproducibility, the SMA wire length is measured in its austenitic, near load-free state in a special measuring setup. The SMA wire is then inserted into a PTFE tubing for electrical and thermal isolation and crimped with ring terminals on both ends. After the SMA wire has been prepared, the suction cup can be assembled and adjusted (Figure 3.9). After assembly, the actuator is activated for 50 cycles and adjusted again. This "training" is necessary because the remnant strain in SMA wires changes over the first few cycles and thus the equilibrium points of the forces shift. The assembly starts with the lower fixation (step 1) on which the linear spring (step 2). After that, the threaded rod is connected to the

membrane and the upper fixation is connected to the opposing end of the rod (step 3). In step 4, the spring is manually compressed and held in a compressed state by a mounting aid, so that the SMA wire can be winded in a load-free state. The mounting aid is then removed (step 5) and the SMA wire is loaded and stretched.

After this basic assembly, all components have to be adjusted to ensure functionality of the actuator. For this purpose, the SMA wire is activated which causes a contraction of the SMA wire and a compression of the spring (step 6). In this state, the membrane has to be brought into a flat configuration with the help of the threaded rod and the adjustment nuts (step 7). Finally, the linear spring is brought to the required compression via its adjustment screws (step 8). The assembled prototype is displayed in Figure 3.10. Besides the metal parts and the rubber membrane, this prototype uses 3D-printed plastic components printed by an Objet Connex500^{TM}.
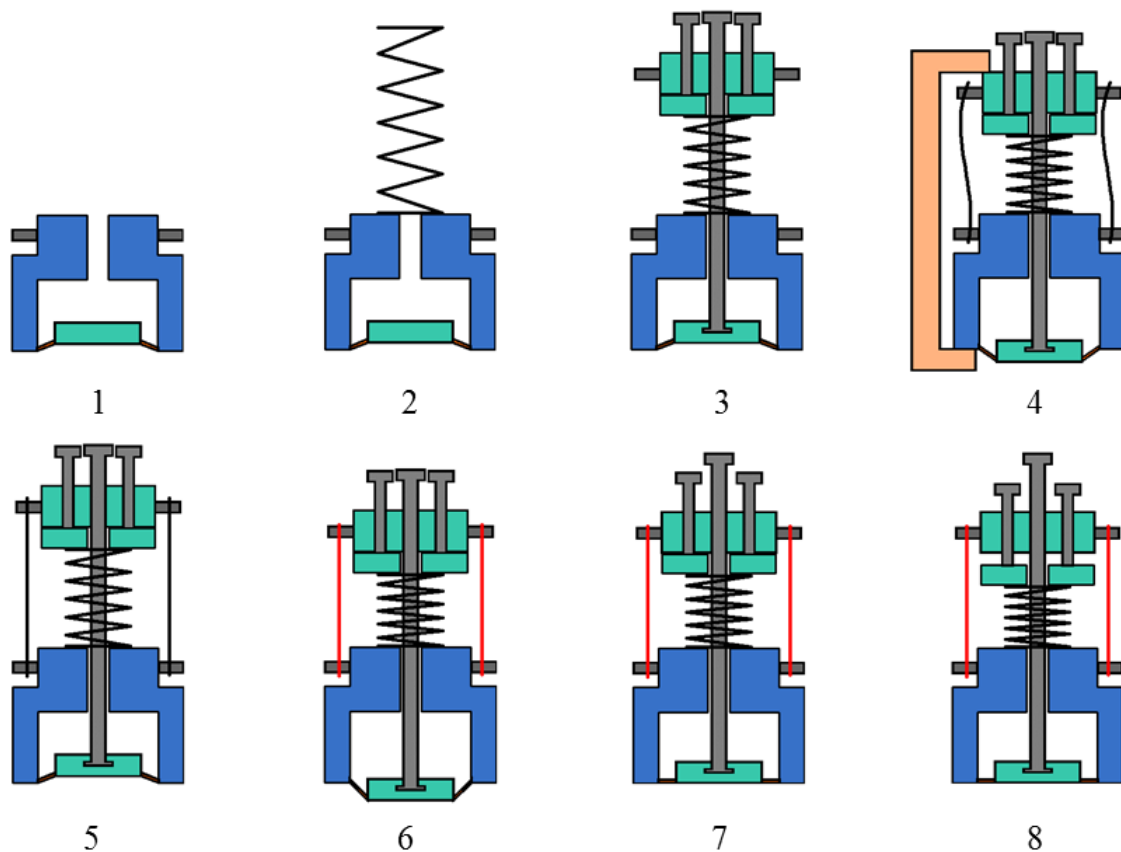

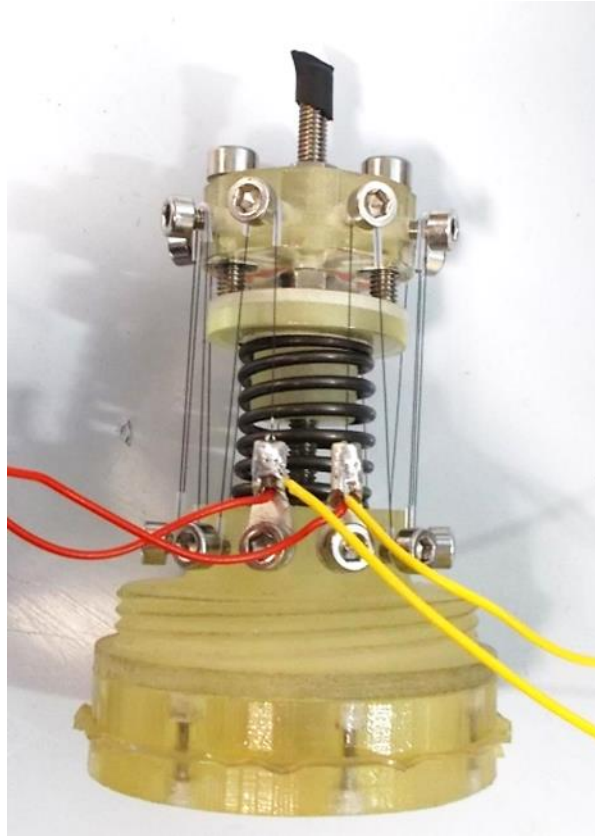**Figure 3.9:** Step-wise assembly of the SMA suction cup prototype.

Figure 3.10: Assembled prototype of the SMA suction cup.

3.2.1.3 SMA Actuator Design

The design process of the SMA suction cup is divided in three phases. First, the system kinematics are analyzed, followed by a study of the equilibrium of forces and an identification of the force characteristics. Finally, these equations are used to determine the design parameters with respect to the target specifications.

Kinematic Study

The suction cup design results in simple kinematic relationships as shown in Figure 3.11. A displacement Δx of the central piston causes the same displacement for the SMA stroke, the spring compression and the membrane displacement. For the two relevant states, which are the activated suction cup position (index a, SMA wires cold) and deactivated or flat suction cup position (index f, SMA wires heated), the kinematic equations are:

$$\Delta x = x_{mem,a} - x_{mem,f}$$
$$\Delta x = x_{spr,a} - x_{spr,f} \tag{3.5}$$
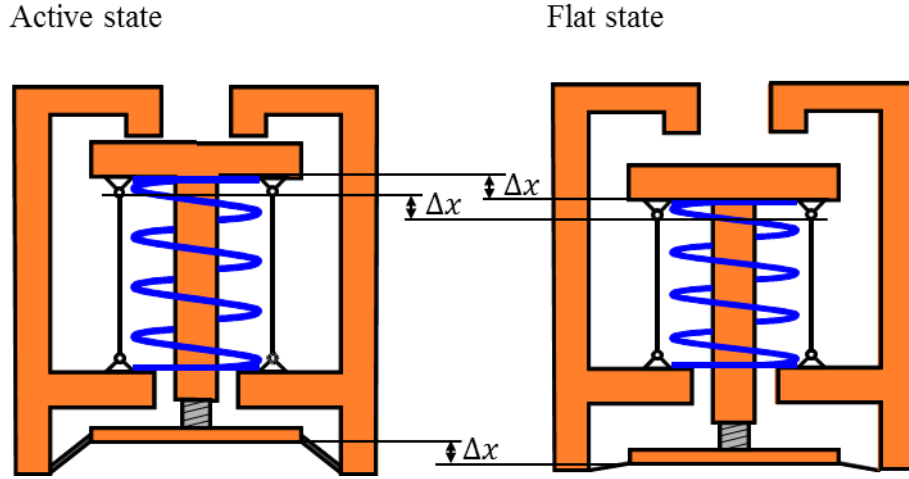$$\Delta x = x_{sma,a} - x_{sma,f}$$

Figure 3.11: Kinematic relationships in the SMA suction cup's activated and deactivated position.

Kinetic Study

The kinetic study includes an equilibrium of forces and the analysis of the different force components $F_{vac}\left(x_{mem,a}, x_{mem,f}\right)$, $F_{spr}\left(x_{spr,a}, x_{spr,f}\right)$ and $F_{sma}\left(x_{sma,a}, x_{sma,f}\right)$ with respect to their quasi-static force-displacement characteristics. The free body diagram (Figure 3.12) considers the situation of a gripped workpiece that causes external forces (Figure 3.12 a). The force relationships relevant for the actuator design are displayed in Figure 3.12 (c) and Figure 3.12 (e). The equilibrium of forces at the workpiece (c) is described by

$$F_{vac} = F_{rim} + F_{ext}. \tag{3.6}$$

F_{rim} describes the contact force, which is always greater than zero ($F_{rim} > 0$), which leads to the following requirement to hold a workpiece:

$$F_{vac} > F_{ext}. \tag{3.7}$$

The equilibrium of forces at the piston (Figure 3.12 e) results in

$$F_{spr} - F_{sma} - F_{mem} = F_{vac}. \tag{3.8}$$

The membrane forces F_{mem} [111], [112] are negligible in comparison to the other force components in this case, as shown in [110], so that the relevant force relationship can be described with
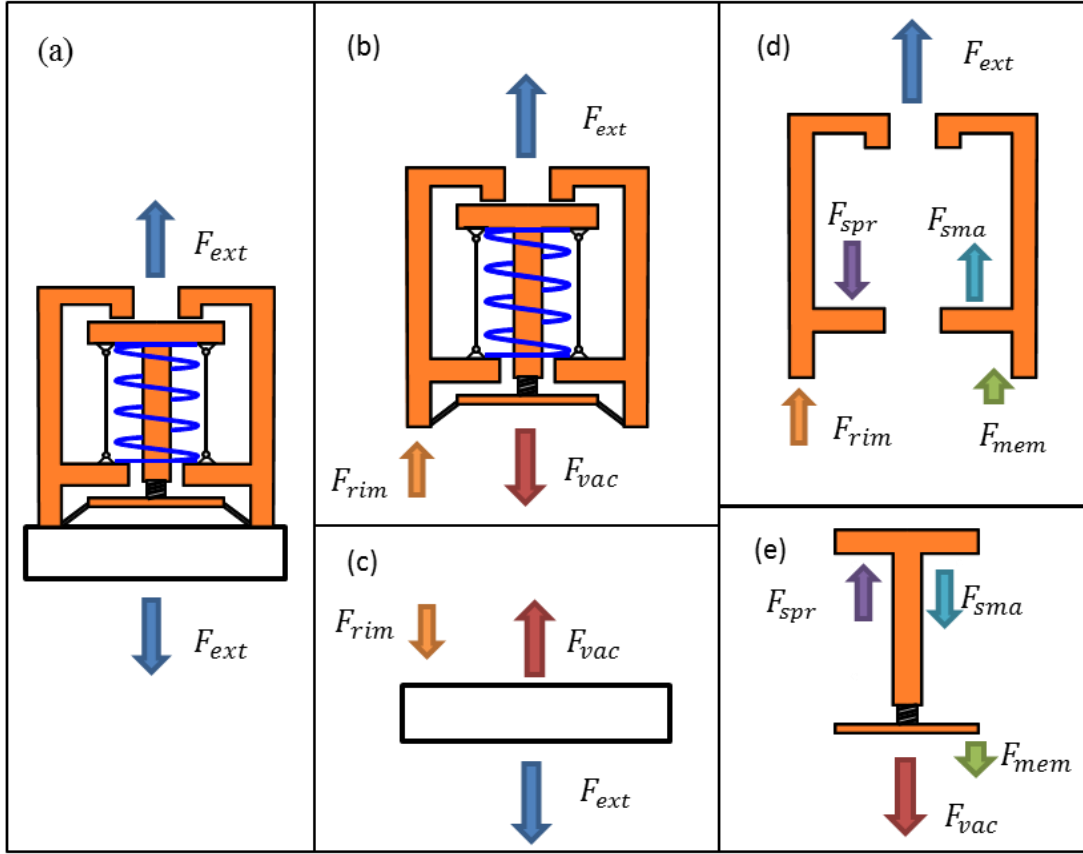
$$F_{spr} - F_{sma} = F_{vac}. \tag{3.9}$$

23

Figure 3.12: Free body diagram of the SMA suction cup components.

If the suction cup is in its flat state, the vacuum force F_{vac} equals zero ($F_{vac,f} = 0$). The equilibrium of forces for the activated and the flat state is determined by

$$
\begin{aligned}
F_{spr,f} - F_{sma,f} &= 0 \\
F_{spr,a} - F_{sma,a} &= F_{vac}.
\end{aligned}
\tag{3.10}
$$

As part of the kinetic study, the three force-displacement characteristics $F_{vac}\left(x_{mem,a}, x_{mem,f}\right)$, $F_{spr}\left(x_{spr,a}, x_{spr,f}\right)$ and $F_{sma}\left(x_{sma,a}, x_{sma,f}\right)$ have to be determined.

Vacuum Force

The vacuum force of a membrane with the outer radius R is calculated by

$$
F_{vac} = R^2 \pi \left(p_{atm} - p_a \right)
\tag{3.11}
$$

with the atmospheric pressure p_{atm} and the internal pressure p_a. To relate the change in pressure to a change in the volume underneath the membrane, the Boyle-Mariotte law for constant temperatures $p \cdot V = const$ is used. If the membrane is in a flat state, a volume V_f is inclosed at atmospheric pressure p_{atm}. If the membrane is then deflected by an external

force, the volume changes to V_a and the internal pressure changes to p_a. With Boyle-Mariotte, this leads to

$$\frac{p_a}{p_{atm}} = \frac{V_f}{V_a}. \tag{3.12}$$

The internal pressure p_a in (3.11) can be eliminated with (3.12), so that the vacuum force is calculated with

$$F_{vac} = R^2 \pi \, p_{atm} \left(1 - \frac{V_f}{V_a}\right). \tag{3.13}$$

The volume under the membrane in its flat state ($x_{mem,f} = 0$) equals the dead volume V_0 ($V_f = V_0$). For the volume in the activated state, two approximations can be made (Figure 3.13). For the cylinder approximation, the volume in the activated state equals

$$V_{a,min} = V_0 + \pi r^2 \Delta x. \tag{3.14}$$

The cone volume approximation results in

$$V_{a,max} = V_0 + \pi \frac{1}{3}\left(r^2 + rR + R^2\right)\Delta x. \tag{3.15}$$
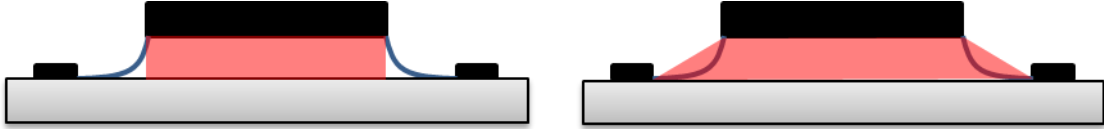

Figure 3.13: Cylinder (left-hand side) and cone (right-hand side) approximation of the membrane geometry in its activated state.

The approximations of the volume (3.14) and (3.15) can now be used in the equation for the vacuum force (3.13) to generate approximations for the minimum and maximum theoretically achievable vacuum forces:

$$F_{vac,min} = R^2 \pi \, p_{atm} \left(1 - \frac{V_f}{V_{a,min}}\right) = R^2 \pi \, p_{atm} \left(1 - \frac{V_0}{V_0 + \pi r^2 \Delta x}\right), \tag{3.16}$$

$$F_{vac,max} = R^2 \pi \, p_{atm} \left(1 - \frac{V_f}{V_{a,max}}\right) = R^2 \pi \, p_{atm} \left(1 - \frac{V_0}{V_0 + \pi \frac{1}{3}\left(r^2 + rR + R^2\right)\Delta x}\right). \tag{3.17}$$

Depending on the design parameter, either one of the two approximations (3.16) and (3.17) is used to calculate the vacuum force in a worst-case scenario. For a given gripping force, the cylinder approximation (3.16) is used to calculate the inner and outer radii of the membrane, whereas for the estimation of spring forces and SMA forces the cone approximation (3.17) is used because they are working against the vacuum force. Figure 3.14 shows an example for the different behavior of the membrane force depending on the approximation in relation to the membrane stroke. The parameters in this example are declared as

$$R = 15\,mm$$
$$r = 10\,mm$$
$$V_0 = 500\,mm^3.$$
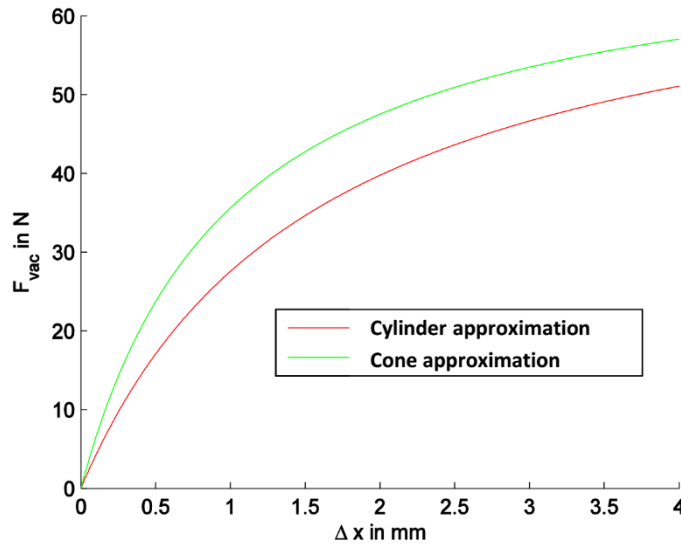
Figure 3.14: Example for the pessimistic and optimistic approximation of the vacuum force F_{vac} in relation to the stroke of the membrane Δx.

Spring Force

The spring acts in this actuator system like an energy storage system. When the SMA wire cools down and elongates, the spring deflects the membrane until it reaches the activated state. The resulting forces are based on linear spring behavior

$$F_{spr} = k\,\Delta x_{spr} = k\,(L_{spr,0} - x_{spr}), \tag{3.18}$$

so that the spring forces for both membrane states can be calculated with

$$F_{spr,a} = k\left(L_{spr,0} - x_{spr,a}\right)$$
$$F_{spr,f} = k\left(L_{spr,0} - x_{spr,f}\right). \tag{3.19}$$

SMA Force

The SMA force in the activated and the flat state is determined by the total SMA cross-section A_{SMA} and the mechanical stress σ:

$$F_{sma,a} = \sigma_a \, A_{sma},$$
$$F_{sma,f} = \sigma_f \, A_{sma}. \tag{3.20}$$

In this actuator design, the complex stress-strain behavior of SMAs is approximated by linear relationships (single crystal behavior). Considering a complete phase transformation between the activated and the flat state, the stress-strain characteristics are specified by

$$\sigma_f = \sigma_A = E_A \, \epsilon_A = E_A \left(\frac{x_{sma,f}}{L_{sma,0}} - 1\right),$$
$$\sigma_a = \sigma_M = E_M \left(\epsilon_M - \epsilon_T\right) = E_M \left(\frac{x_{sma,a}}{L_{sma,0}} - 1 - \epsilon_T\right). \tag{3.21}$$

E_A and E_M describe the Young's modulus of the SMA wire in its austenitic and martensitic state, ε_A and ε_M the according material strains in that phase. In the activated (martensitic) state, the transformation strain ε_T is additionally taken into account. The material parameters E_A, E_M and ε_T are obtained from the suppliers' data sheets [14], [15] and from measurement data [24].

A summary of the physical description of the actuator system is given in Table 1. These system equations are used in the following section to determine the unknown design parameters for the SMA suction cup.

Determination of the Design Parameters

For the determination of the design parameters listed in Table 2, specifications regarding the suction cup functionality and design have to be made. The central specification is the desired maximum gripping force F_{hold}, which is depending on the vacuum quality S. The desired vacuum quality S is described by

$$S = 1 - \frac{p_a}{p_{atm}}. \tag{3.22}$$

That means $S = 1$ equals a perfect vacuum. The desired actuation frequency is directly related to the cooling behavior of the SMA wire and thus the wire diameter. Therefore, the desired cooling time t_{cool} is another important specification.

Table 1: Summary of the physical description of the SMA actuator system in the SMA suction cup used for the determination of the design parameters.

	Activated State	Flat State
Equilibrium of Forces	$F_{spr,a} - F_{sma,a} = F_{vac}$	$F_{spr,f} - F_{sma,f} = 0$
Spring Force	$F_{spr,a} = k\,(L_{spr,0} - x_{spr,a})$	$F_{spr,f} = k\,(L_{spr,0} - x_{spr,f})$
Vacuum Force	$F_{vac} = R^2\,\pi\,p_{atm}\left(1 - \dfrac{V_f}{V_a}\right)$	-
Maximum Volume Activated	$V_{a,max} = V_0 + \pi\dfrac{1}{3}(r^2 + r\,R + R^2)\,\Delta x$	$V_f = V_0$
Minimum Volume Activated	$V_{a,min} = V_0 + \pi\,r^2\,\Delta x$	
SMA Force	$F_{sma,a} = \sigma_a\,A_{sma}$	$F_{sma,f} = \sigma_f\,A_{sma}$
SMA Stress	$\sigma_a = E_M\left(\dfrac{x_{sma,a}}{L_{sma,0}} - 1 - \epsilon_T\right)$	$\sigma_f = E_A\left(\dfrac{x_{sma,f}}{L_{sma,0}} - 1\right)$
Kinematics	$\Delta x = x_{spr,a} - x_{spr,f}$ $\Delta x = x_{sma,a} - x_{sma,f}$	

Table 2: Design parameters for the complete description of the SMA suction cup.

R	Outer membrane radius
r	Inner membrane radius
$L_{spr,0}$	Unloaded spring length
k	Spring rate
$x_{spr,f}$	Spring length in flat state
N_{sma}	Number of SMA wires
$L_{sma,0}$	Austenitic SMA wire length
D_{sma}	SMA wire diameter

As shown in section 3.1 and [14], the stroke output of an SMA actuator system with a linear spring is directly dependent on the linear spring characteristic. Stiff springs lead to lower stroke output whereas a near constant force leads to maximum contraction of the SMA wire. The parameter Q describes the ratio between the spring force in the activated and the flat state and is thus a measure for the constancy of the spring force during actuation:

$$Q = \frac{F_{spr,a}}{F_{spr,f}}.$$

(3.23)

Like S, values for Q range from 0 to 1, whereas 1 stands for a (for linear springs not achievable) constant force during actuation. The specifications in this example are summarized in Table 3.

Table 3: Design specifications for the SMA suction cup prototype.

F_{hold}	Minimal gripping force	> 55 N
S	Vacuum quality parameter	> 0.8
t_{cool}	SMA wire cooling time	< 2 s
Q	Spring force constancy parameter	> 0.9

The outer membrane radius R is determined with (3.11), (3.22) and the specification for the gripping force F_{hold}:

$$F_{vac} = R^2 \pi p_{atm} S > F_{hold}$$
$$\Leftrightarrow R > \sqrt{\frac{F_{hold}}{\pi p_{atm} S}}.$$

(3.24)

To create high gripping forces, a high value for the inner radius r is desired in (3.16) and (3.17), but at the same time the difference $R - r$ is limited because of the approximation of negligible membrane forces. This approximation can only be made in this case for values $r \leq 0.66R$. To guarantee highest possible gripping forces, r is selected at its maximum value of $0.66R$.

The stroke of the membrane Δx is calculated for the worst-case scenario with the pessimistic volume estimation (3.14):

$$S = 1 - \frac{p_a}{p_{atm}} = 1 - \frac{V_0}{V_{a,min}} = 1 - \frac{V_0}{V_0 + \pi\, r^2\, \Delta x}$$

$$\Leftrightarrow \Delta x = \frac{V_0\, S}{(1-S)\,\pi\, r^2}.$$

(3.25)

The dead volume V_0 can be calculated or determined by the CAD software after the specific membrane construction is designed. With this, all required membrane parameters are identified and the vacuum forces for the minimum (3.16) and maximum (3.17) approximations can be calculated.

With the membrane stroke Δx, the SMA wire length $L_{sma,0}$ can be identified. All SMA parameters are calculated based on the single crystal assumptions (3.21). First , the material parameters E_A, E_M and ε_T are graphically determined with measurement data from [24] (Figure 3.15). The Young's moduli in the austenitic and martensitic phase are approximated by linear fits in Figure 3.15, the transformation strain ε_T is presumed as 5 % [14], [15].
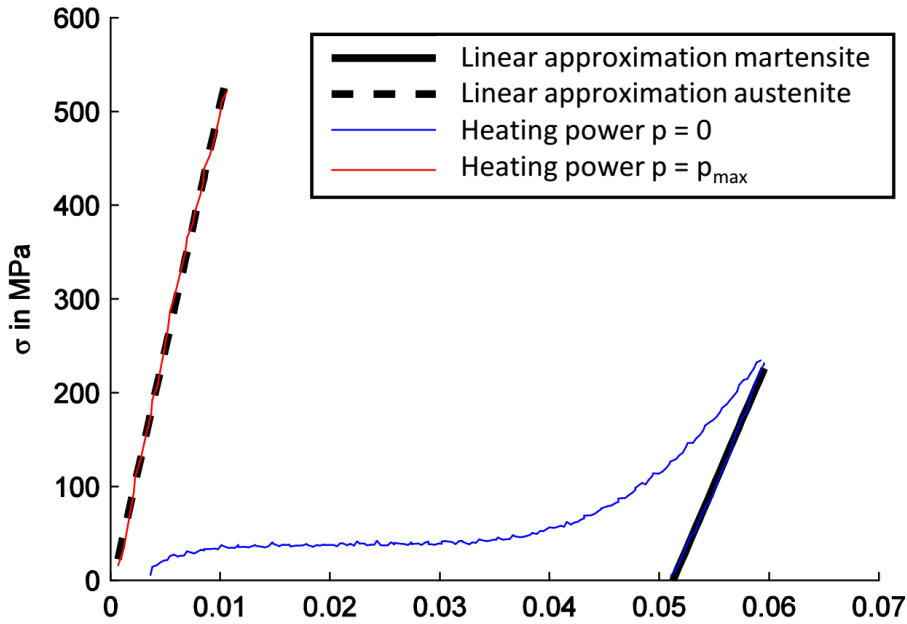
Figure 3.15: Measured stress-strain characteristic of a 76 µm SMA wire for two constant heating powers [24].

In addition, the suppliers' data sheets suggest a minimum material stress of $\sigma_{min} = 69MPa$ to guarantee the return to a complete M⁺ phase after cooling. The reported yield strength of the SMA wires equals $\sigma_{max} = 345MPa$ for limited total lifetime cycles [14], [15]. The mechanical stresses in the SMA wire in the suction cup's activated and flat state (σ_a, σ_f) are chosen with respect to these restrictions, while taking into account a safety margin for

the reverse phase transformation. The declaration of these material parameters allows to solve the linear system of equations (3.5) and (3.21) with the unknown variables $x_{sma,f}$, $x_{sma,a}$ and $L_{sma,0}$:

$$
\begin{pmatrix}
E_M & 0 & -\left(E_M\left(1+\epsilon_T\right)+\sigma_a\right) \\
0 & E_A & -\left(E_A+\sigma_f\right) \\
1 & -1 & 0
\end{pmatrix}
\begin{pmatrix}
x_{sma,a} \\
x_{sma,f} \\
L_{sma,0}
\end{pmatrix}
=
\begin{pmatrix}
0 \\
0 \\
\Delta x
\end{pmatrix}.
\tag{3.26}
$$

The specific values of the material parameters are summarized in Table 4:

Table 4: Material parameters for the design of the SMA suction cup.

σ_{min}	65 MPa
σ_{max}	345 MPa
E_M	27 GPa
E_A	52 GPa
ϵ_T	5 %
σ_a	100 MPa
σ_f	345 MPa

For the calculation of the spring forces, the force equilibrium (3.10) is combined with the maximum possible vacuum force (3.17). The ratio of the SMA forces $F_{sma,a}$ and $F_{sma,f}$ equals the ratio of the material stresses σ_a and σ_f (3.20):

$$
\frac{F_{sma,a}}{F_{sma,f}} = \frac{\sigma_a}{\sigma_f} = \frac{F_{spr,a} - F_{vac,max}}{F_{spr,f}}.
\tag{3.27}
$$

With (3.23) for the spring constancy, (3.27) can be converted to

$$
\frac{F_{spr,a}}{F_{spr,f}} = \frac{\sigma_a}{\sigma_f} + \frac{F_{vac,max}}{F_{spr,f}} < Q.
\tag{3.28}
$$

The spring can now be selected with the requirement of a minimum force in its compressed configuration (flat state of the suction cup):

$$
F_{spr,f} > F_{spr,f,min} = \frac{F_{vac,max}}{Q - \dfrac{\sigma_a}{\sigma_f}}.
\tag{3.29}
$$

The selection of the spring has to take into account the geometrical constraints of the suction cup design, like maximum outer diameter and compressed length of the spring. The spring force in its compressed configuration should be higher but as close as possible to the minimum $F_{spr,f,min}$. The selection of a suitable spring defines the spring parameters k and $L_{spr,0}$.

For the selection of the SMA wire, the total SMA cross section A_{sma} has to be determined. The difference of the spring forces (3.19) in the activated and flat state equals

$$F_{spr,f} - F_{spr,a} = k\,\Delta x. \tag{3.30}$$

The force equilibrium (3.10) together with the SMA forces (3.20) and the difference of the spring forces (3.30) again create a linear system of equations, that has exactly one physically meaningful solution:

$$\begin{pmatrix} \sigma_a & -1 & 0 & 0 & 0 \\ \sigma_f & 0 & -1 & 0 & 0 \\ 0 & -1 & 0 & 1 & 0 \\ 0 & 0 & -1 & 0 & 1 \\ 0 & 0 & 0 & -1 & 1 \end{pmatrix} \begin{pmatrix} A_{sma} \\ F_{sma,a} \\ F_{sma,f} \\ F_{spr,a} \\ F_{spr,f} \end{pmatrix} = \begin{pmatrix} 0 \\ 0 \\ F_{vac} \\ 0 \\ k\,\Delta x \end{pmatrix}. \tag{3.31}$$

Linear equation systems like (3.26) and (3.31) can easily be solved with the help of software tools like MATLAB.

With the parameters identified above, the spring lengths in both suction cup states ($x_{spr,f}, x_{spr,a}$) can be calculated with (3.19) and (3.5):

$$x_{spr,f} = L_{spr,0} - \frac{F_{spr,f}}{k}$$
$$x_{spr,a} = x_{spr,f} + \Delta x. \tag{3.32}$$

Last parameters necessary for the suction cup design are the SMA wire diameter D_{sma} and directly linked to that the total number of SMA wires N_{sma}. The wire diameter depends on the required cooling time t_{cool} and is chosen with the help of the manufacturer specifications [14], [15]. Wire diameters relevant for this application and resulting cooling times are displayed in Table 5:

Table 5: Cooling times for different SMA wire diameters [14].

SMA wire diameter	Cooling time
0.1 mm	0.9 s
0.13 mm	1.4 s
0.15 mm	1.7 s
0.2 mm	2.7 s

After choosing the SMA wire diameter, the number of SMA wires is determined with

$$N_{sma} > \frac{A_{sma}}{\left(\dfrac{D_{sma}}{2}\right)^2 \pi}. \tag{3.33}$$

A summary of the determined design parameters in the case of the SMA suction cup is given in Table 6.

Table 6: Calculated and selected parameter values for the design of the SMA suction cup.

	Design parameter	Calculated value	Selected value
R	Outer membrane radius	14.7 mm	15 mm
r	Inner membrane radius	9.7 mm	10 mm
$L_{spr,0}$	Unloaded spring length	51.5 mm	
k	Spring rate	2.97 N/mm	
$x_{spr,f}$	Spring length in flat state	20.8 mm	20 mm
N_{sma}	Number of SMA wires	14,8	16
$L_{sma,0}$	Austenitic SMA wire length	43.1 mm	40 mm
D_{sma}	SMA wire diameter	0.15 mm	

The design scheme demonstrated at the example of the suction cup application can be transferred and used for the design of any linear SMA actuator system using a linear spring. The implementation of the equations in a software tool like MATLAB allows the variation of the parameters during design to find application specific combinations.

3.2.2 **Suction Cup Validation**

The validation setup is displayed in Figure 3.16. The SMA wire heating is realized by a constant current supply. The voltage measurement on the SMA wire is realized via four-wire measurement. An absolute pressure sensor (HYDAC HDA 4346) is used to measure the vacuum created by the suction cup. The actuator stroke is measured with a laser displacement sensor at the upper fixation. Control of the experiments as well as the data acquisition are realized by a National Instruments (NI) cRIO system and LabView.

Figure 3.17 shows measurement results for five activation cycles of the SMA suction cup. The SMA wire is heated for 5 s and then deactivated for 6 s. The actuator reaches a stroke of 1.4 mm, which results in a vacuum pressure of 480 Pa. The voltage measurement can be used to calculate the electrical resistance of the SMA wire and thus use the self-sensing capability for probable monitoring of the vacuum quality.

The average values for actuator displacement, electrical resistance of the SMA wire and vacuum pressure for cycles 2-5 are displayed in Figure 3.18. Additionally, the vacuum pressure is plotted in relation to the actuator stroke. This plot also contains the resulting vacuum pressure estimated with the cone (green) volume approximation (3.15) and the cylinder (red) volume approximation (3.14).
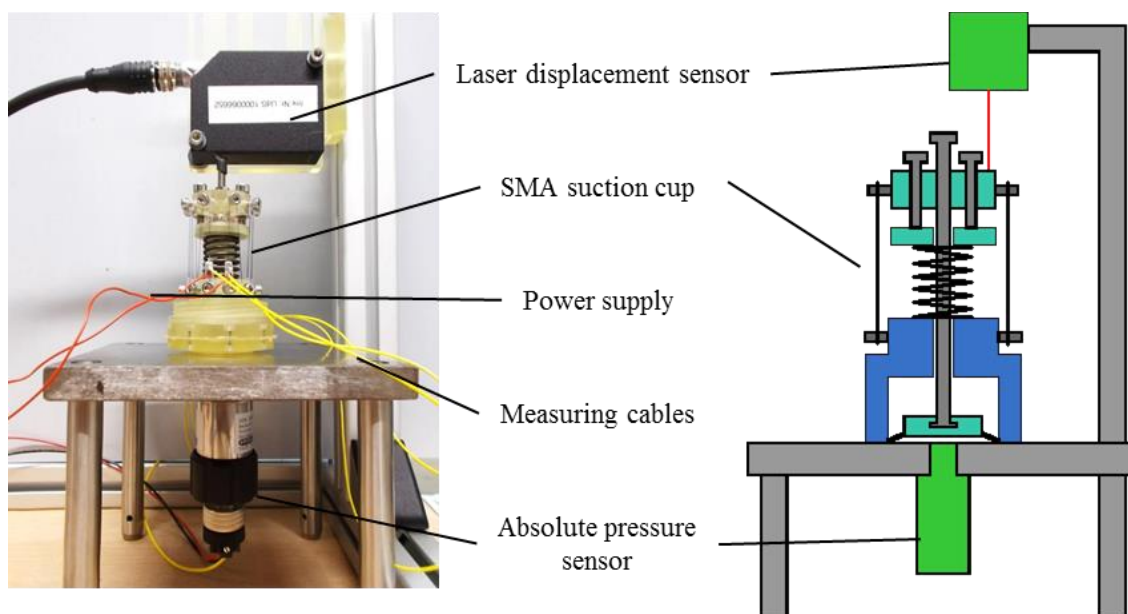
Figure 3.16: Picture and schematic of the validation setup for the SMA suction cup.

The desired vacuum quality of $S = 0.8$, which equals a vacuum pressure of 800 Pa is not reached with a measured pressure of 480 Pa. One reason for this discrepancy is that the desired stroke of 2 mm is not reached. The presumed SMA wire stroke of 5 % in the design should be corrected to 3-4 %, which is a more realistic value for SMA wires in the presented

system configuration. Another reason for the lower vacuum quality could be a wrong estimation of the dead volume V_0. The hysteretic behavior in the pressure signal is likely caused by a deformation of the elastic membrane sealing during activation. The assumption of isothermal conditions during the activation might cause an additional error. The measured cooling times of about 2.5 s are very close to the original specification of 2 s.
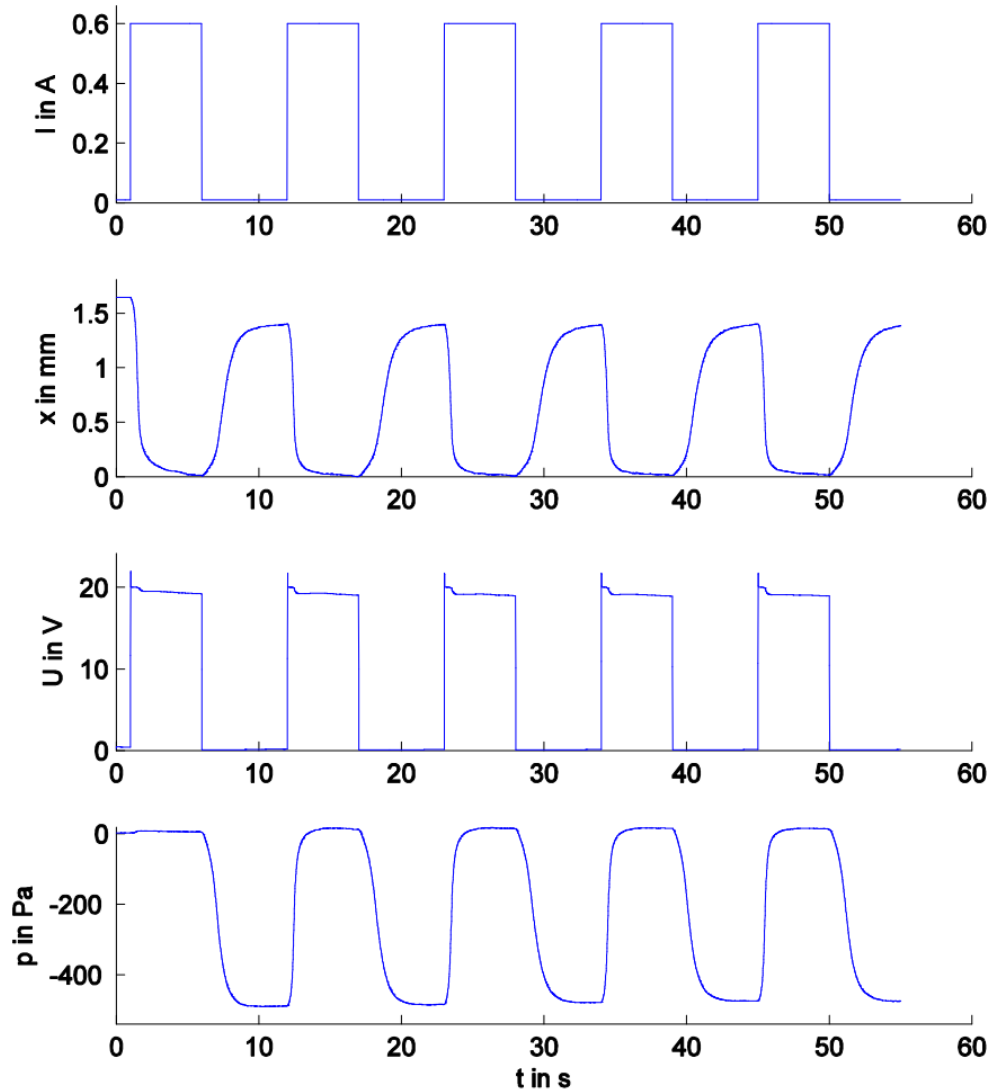
Figure 3.17: Measurement data for five activation cycles of the SMA suction cup. Recorded quantities from top to bottom are: Electrical current [A], actuator displacement [mm], voltage drop on the SMA wire [V] and vacuum pressure [Pa].
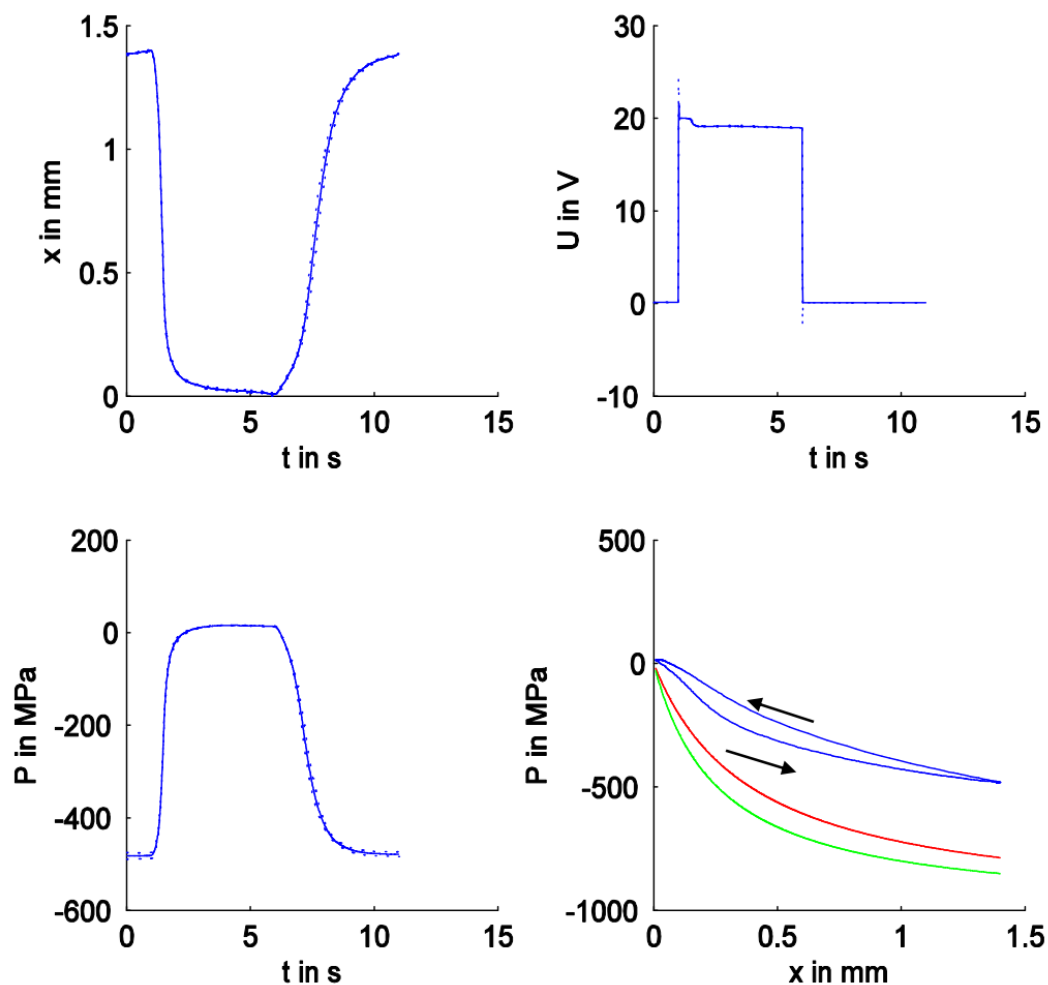
Figure 3.18: Average values for cycles 2-5 of the measurement data for the SMA suction cup. Bottom right shows the vacuum pressure in relation to the actuator stroke (blue) and the vacuum estimations using the cylinder (red) and the cone (green) approximation.

3.3 Design Example 2: SMA End-effector

The development of novel material handling systems and industrial grippers has gained considerable relevance in recent years. Because of low production costs in Asia, industrial manufacturing and assembly has to become more efficient in western countries to maintain international competitiveness. The keywords "Industry 4.0" and "Smart Factory" describe these efforts, using automation, cyber-physical systems and internet of things in manufacturing technologies [113]–[116]. Assembly assistance and human-robot-cooperation have become central fields of research [117], [118]. One goal within "Industry 4.0" aims at making factories and assembly lines more flexible and adaptive, to react to market changes with a simple reconfiguration process. Therefore, also handling systems are required to perform more complicated and complex manipulation tasks. For the handling of plane workpieces, so-called end-effectors or suction spiders are used (Figure 3.19 a) [119]. These systems are attached on the top of industrial robots and consist

of custom fitted suction cup arrangements, so that one end-effector is only used for one specific workpiece geometry. If an assembly robot is used for different workpiece geometries, for example in several production lines, usually the whole end-effector on the robot is replaced by another one that is specifically designed for the new workpiece shape. The stop of production during this exchange process can be very cost intensive. The idea of making an end-effector reconfigurable increases flexibility in production and prevents costly down times because gripper systems have the ability to be adapted automatically to various workpiece geometries. Shape memory alloy actuators are the technology of choice for this application because actuator weight and construction space are very limited. High weights on the top of robots result in critical mass moments of inertia during movement and have to be avoided [107]. Therefore, using conventional drives (electric, pneumatic) for the reconfiguration process of an end-effector is not a viable option. Additionally, the "self-sensing" abilities of SMA wires add more functionality, which can be utilized for possible condition monitoring tasks and position control.

The application of a reconfigurable end-effector is used as a case study for the design of an SMA wire based rotary actuator. Different concepts for rotary actuators based on SMA technology have been presented in several publications [120]–[127]. The concepts introduced in this section demonstrate how the selection of the crucial design parameters affects the rotational output angle. Additionally, a special design, which allows energy-free holding of defined intermediate positions along the rotation radius is presented to attack the disadvantage of continuous heating of the SMA wires. The methods and results presented in this section are based on [62], [63], [65], [72], [75], [77], [128].

3.3.1 End-effector Design and Manufacturing

This section gives a detailed description of the end-effector design, manufacturing and assembly process. First, the overall system is introduced. The SMA actuators have to be integrated into the aluminum structure to enable the desired rotational movements of the gripping arms working against tension springs. Central focus points of the ensuing assembly are the mechanical connection as well as the electrical connection and insulation of the SMA wires. The design process follows the schematic approach of section 3.1, starting with a kinematic analysis, followed by system kinetics including a moment equilibrium. Finally, a graphical method is used for the determination of the design parameters.

3.3.1.1 **Overall System Description**

The basic end-effector design and functionality is displayed in Figure 3.19 (b) and (c). The whole end-effector has an outer diameter of 315 mm. The modular design allows the partial assembly and test of a quarter piece before bringing all four quarters together to a complete
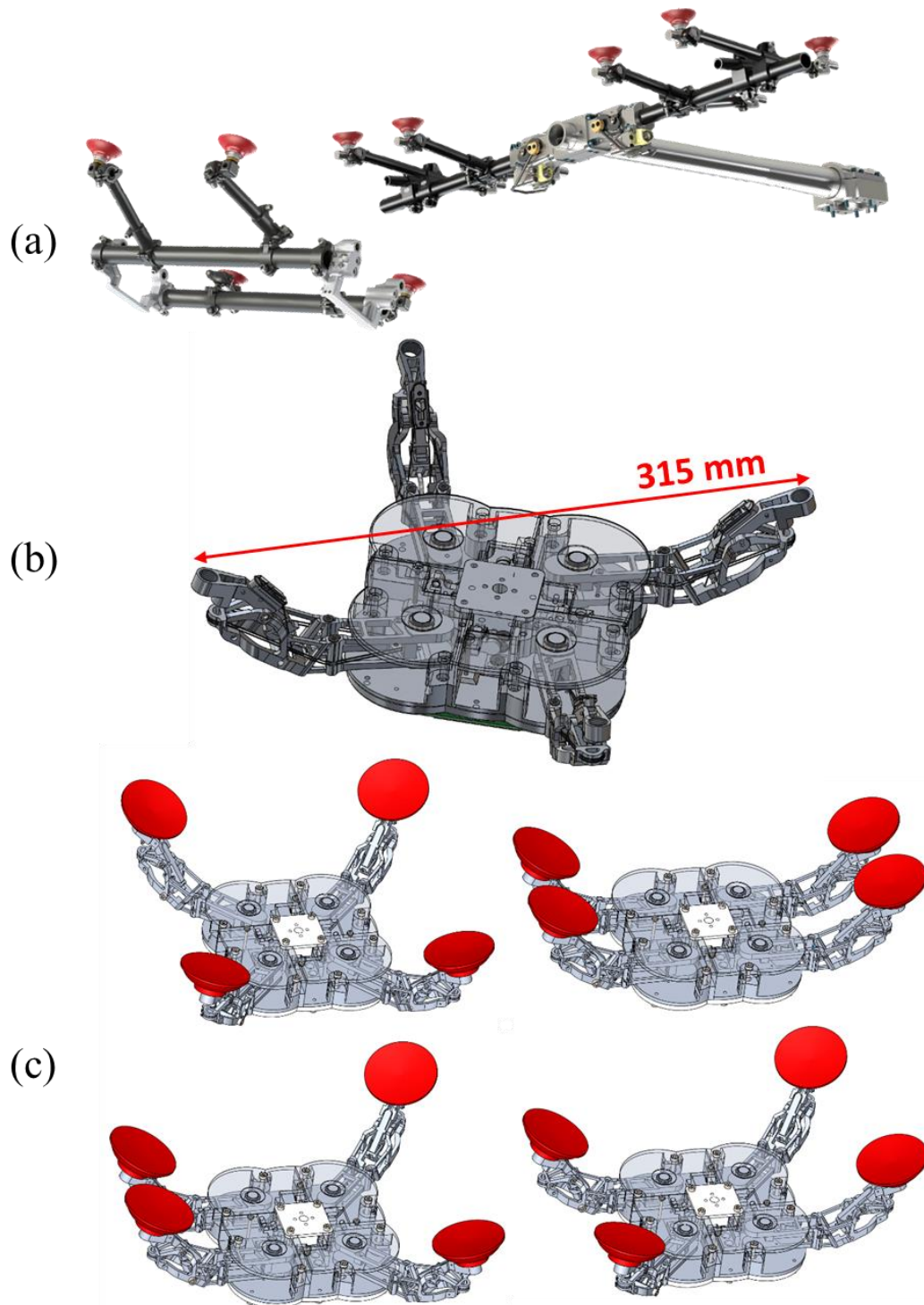
Figure 3.19: State-of-the-art manually adjustable end-effectors (a) [119], the CAD model of the presented end-effector, showcasing its overall dimensions (b) and its reconfiguration functionality with each of the four gripping arms capable of a 90 ° rotational movement in-plane and a 30 ° tilting movement out-of-plane (c).

prototype. Each of the four gripping arms is able to perform a 90 ° rotation in-plane and a 30 ° tilting motion out-of-plane for the handling of workpieces with curved surfaces. Each gripping arm is controlled independently, which allows various end-effector configurations for the handling of a variety of workpiece shapes (Figure 3.19 c). The end-effector components are machined out of aluminum to carry a static load of 10 kg.

A basic overview of the integration of the SMA actuators and the tension springs as their bias mechanism is given in Figure 3.20. The upper part (a) gives an overview of the SMA wire guiding for both DOFs and the attachment of the SMA wires and the return springs. The SMA-spring configuration of the first DOF is illustrated in (b). The SMA wire is guided past the arm's pivot point to the top of the arm and back. A contraction of the SMA wire causes a moment and the tension spring is elongated during the rotation of the arm. A similar configuration is used for the second DOF (Figure 3.20 c). Additionally, the tilting actuator is combined with a locking mechanism that allows energy-free rest positions at the rotational positions of 10 ° and 20 ° (Figure 3.20 d). The rotating tilting arm pushes a snapping wedge back against a pressure spring. Two teeth define the energy-free rest positions. To return to the initial position, the tilting arm is fully rotated to the 30 ° position. From this position, the snapping wedge is guided around the tilting arm teeth on its way back to the initial position. The power supply connection is the center of the end-effector. At the top of the tilting arms, any desired gripping system such as vacuum grippers can be added.

3.3.1.2 SMA Actuator Assembly

The assembly of the SMA actuators includes SMA wire attachment (crimping, clamping, gluing), electrical connection and insulation of the SMA wires, thermal management and applying the correct pre-strain and pre-stress.

The SMA wires are mechanically attached with screws by clamping the wire between washers (Figure 3.21). This clamping method allows an easy exchange of the SMA wires in this prototype. The electrical connection wires are directly soldered to brass washers and nuts (Figure 3.21, lower part) in a way that the electrical and mechanical connections are always separated from each other. This also helps the assembly process or the exchange of a broken SMA wire. To ensure electrical insulation of the aluminum structure, PTFE tubing is used to guide the SMA wire where it touches the structure (Figure 3.21, upper part). PTFE is also suitable for thermal insulation, so the aluminum structure does not act as a heat sink for the SMA wire.
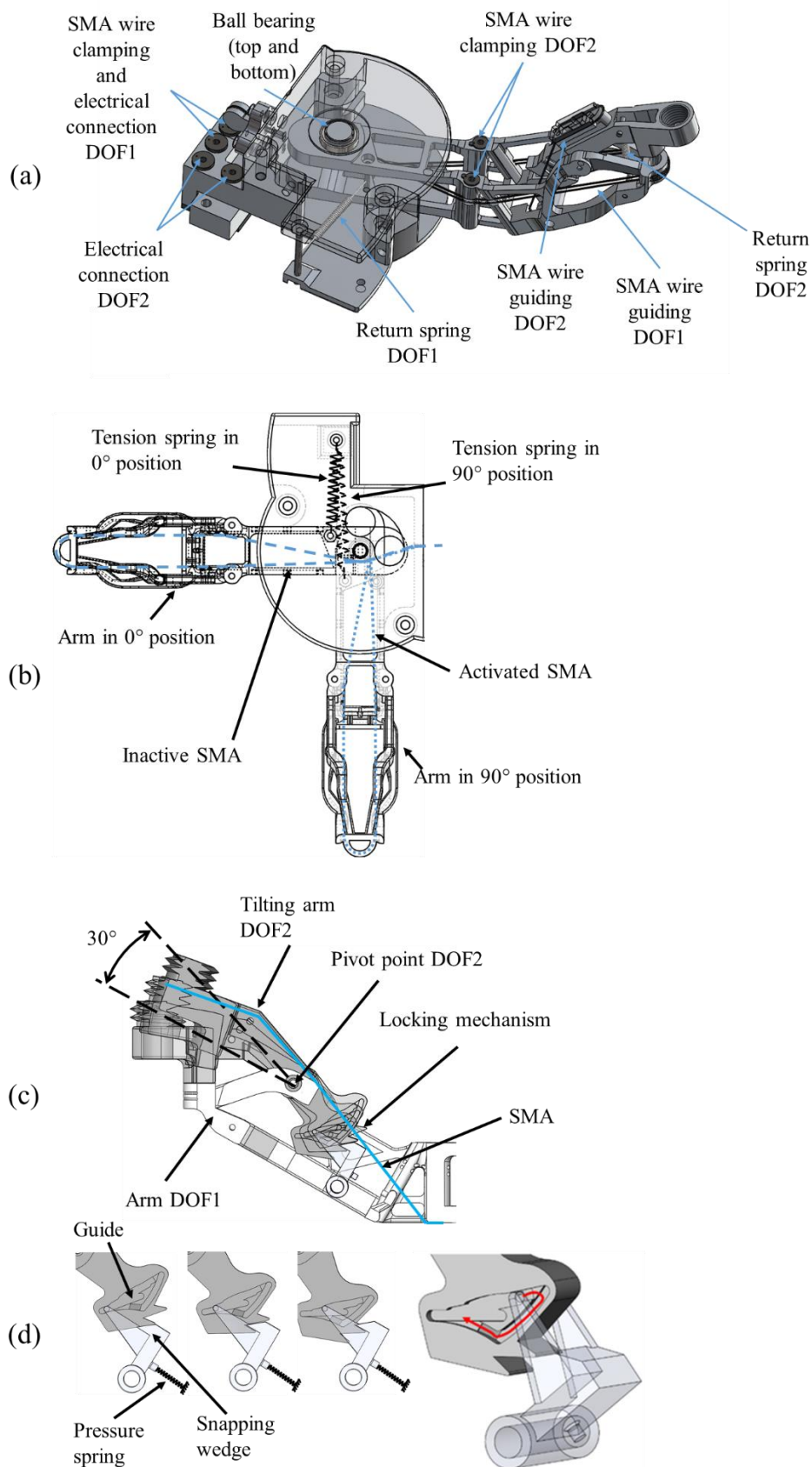
Figure 3.20: CAD model and schematic illustrations of the SMA wire and tension spring integration into the end-effector arm. The SMA wire of the first DOF runs to the top of the arm and back twice to multiply the resulting SMA force (a). The top view schematic (b) [65] shows the SMA wire guiding of DOF1. The tilting arm of DOF2 (c) [65] is combined with a locking mechanism (d) [65].

The clamping screws are electrically insulated by little 3D-printed plastic tubes printed by an Objet Connex500™ using VeroClear™ material (Figure 3.21, lower part). The SMA wire of the first DOF is wrapped around the top of the gripping arm twice to produce a higher total SMA force. That allows the use of thinner SMA wire diameters and thus better actuator dynamics because of faster cooling times. The total displacement is not affected by the SMA wire wrapping, since only the effective SMA wire length (Figure 3.21, upper part) is relevant for estimating the SMA stroke. A special "tension device" (Figure 3.21, lower part) is designed for two reasons. It guides the SMA wire at this end of the arm and at the same time can be used to control the pretension in the SMA wire.
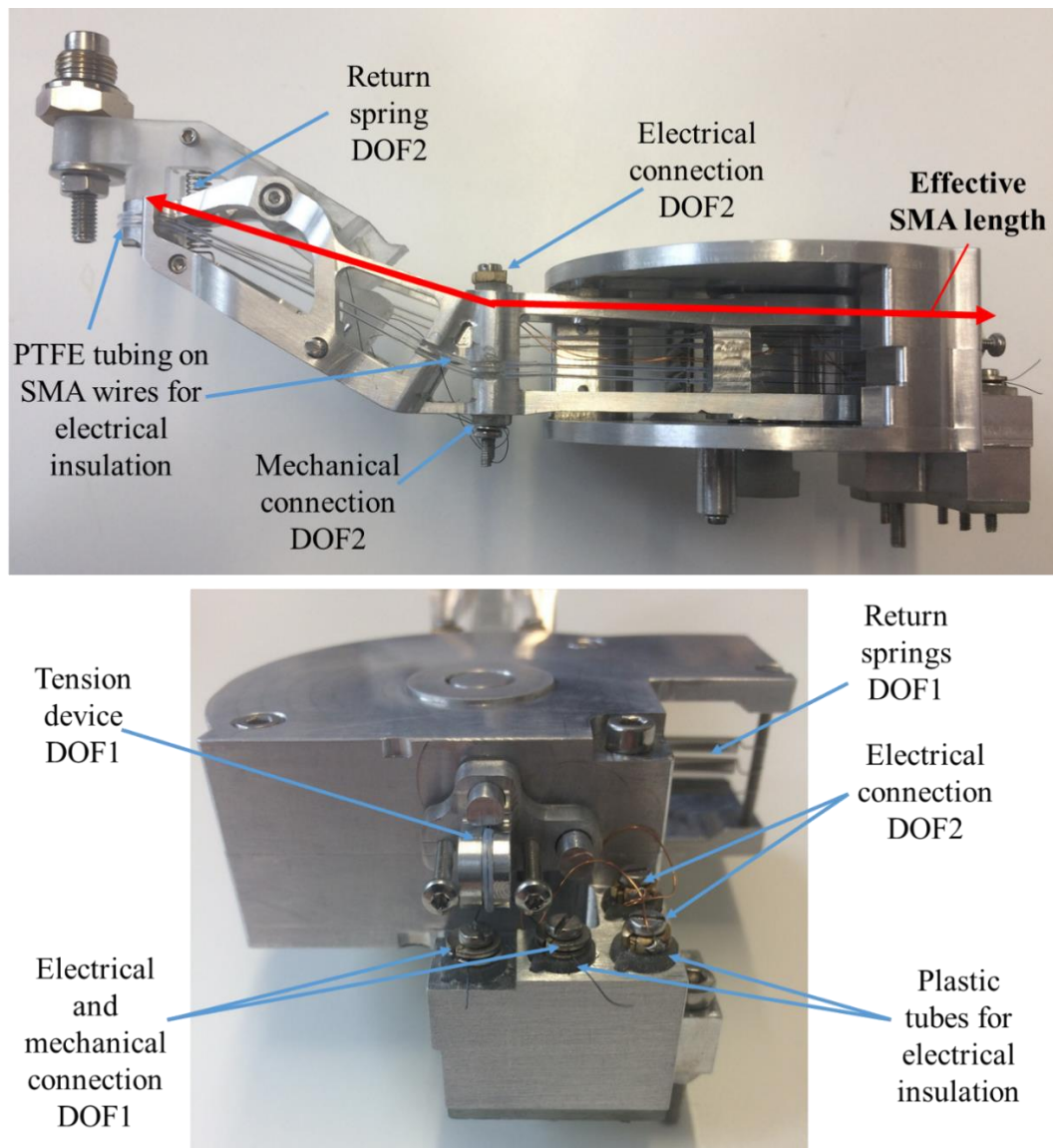
Figure 3.21: Picture of one assembled end-effector arm. The side view (upper part) shows the SMA wire guiding as well as the second DOF's mechanical and electrical connections. The rear view (lower part) gives a detailed view of the central electrical connection for the power supply. The tension device is used to control the SMA wire pretension in the first DOF.

To guarantee the functionality, it is crucial to integrate the SMA wires with the correct pre-strain and pretension. In this case, the SMA wire length is first measured in its unloaded, activated austenitic state, because this is the only reproducible reference length. After cooling and returning to its martensitic state, the wire is stretched for 4 % of the measured austenitic length before integrating it into the end-effector. The fine-tuning of the pretension in the application is realized with this tension device via two adjustment screws.

3.3.1.3 SMA Actuator Design

The design process again is divided into three phases. In a first step, the kinematics of the system have to be studied and understood. Based on those results, the kinetic relationships, meaning the forces and moments can be analyzed in a second phase, regarding the necessary SMA wire forces. Finally, the SMA wire diameter can be chosen with respect to these forces and desired actuation speeds. The following section exemplary details the design of the rotary actuator for the first DOF, but can be utilized for the second DOF analogically.

Kinematic Study

The kinematic study is necessary to identify the crucial design parameters that dictate the movement behavior of the rotational actuator. In this actuation principle, the distance from the SMA wire to the pivot point of the hinged joint is the deciding parameter that influences torque and rotational angles. The closer the SMA wire is guided to the pivot point, the more rotational movement is gained from the SMA wire's contraction, but at the same time, the moment gained from the SMA force decreases with reduced distance. The overall geometry of the end-effector is given in this application and the SMA actuation mechanism needs to fit into it. Therefore, in the presented design, the total effective SMA wire length for the first DOF is $l_{SMA} = 145$ mm. That means the design has to aim at producing a rotation output of 90 ° at the given SMA wire stroke, but still providing a maximum possible torque. To find a good operating point, the kinematics are displayed in Figure 3.22. The figure shows the gripping arm in its initial position with the SMA wire deactivated (upper part) and the end position in its activated state (lower part). The crucial design parameters that affect the SMA wire's distance to the pivot point during the rotational motion are identified and defined as d_{h0} and d_{v0}. They describe the horizontal and the vertical distances of the end of the SMA wire guiding within the gripping arm in the initial deactivated state. The parameters s_h and s_v describe the horizontal and vertical distances of the pivot point to the SMA wire guiding within the end-effector's base. The goal of the kinematic study is to find a relationship between d_{h0}, d_{v0}, s_h and s_v. The free length of the SMA wire in both, the

activated and the deactivated state is indicated in Figure 3.22. The difference between the free lengths in those two states represents the necessary SMA contraction for the rotational angle of 90 °. In both states, this free length can be calculated with the Pythagorean Theorem. In the initial deactivated state (Figure 3.22, upper part), the free length x_0 can be calculated with

$$x_0 = \sqrt{\left(s_h + d_{h0}\right)^2 + \left(s_v + d_{v0}\right)^2}. \tag{3.34}$$

The free length x_1 in the activated position (Figure 3.22, lower part) is calculated via

$$x_1 = \sqrt{\left(s_h + d_{v0}\right)^2 + \left(s_v - d_{h0}\right)^2}. \tag{3.35}$$

The resulting SMA stroke for this rotational movement is defined as

$$\Delta x = x_0 - x_1 = \sqrt{\left(s_h + d_{h0}\right)^2 + \left(s_v + d_{v0}\right)^2} - \sqrt{\left(s_h + d_{v0}\right)^2 + \left(s_v - d_{h0}\right)^2}. \tag{3.36}$$
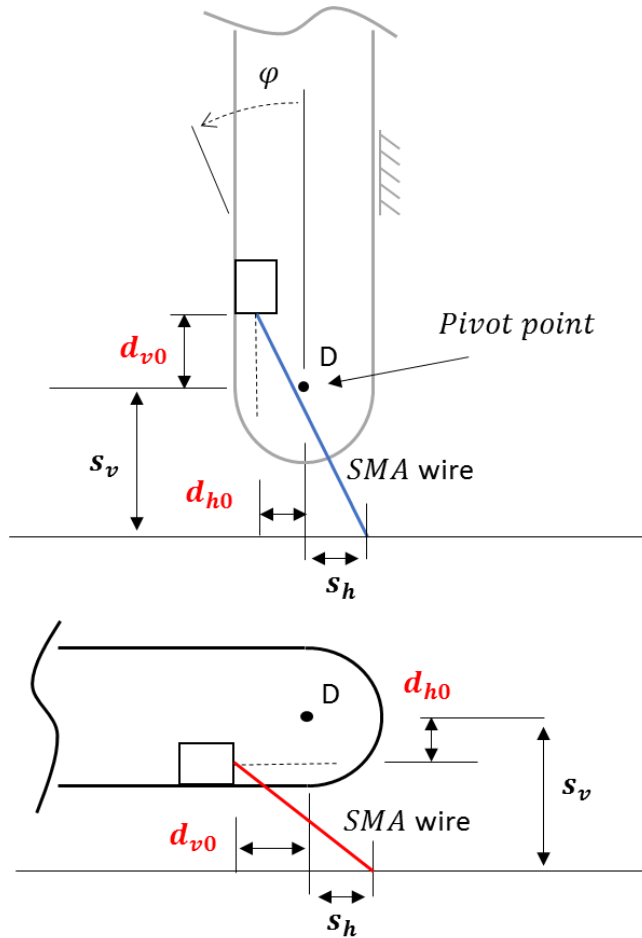
Figure 3.22: Sketch of the gripping arm in deactivated state (upper part) and activated part (lower part) to illustrate the kinematic relationships.

If the SMA stroke Δx is considered as given in (3.36), it is possible to declare two of the four parameters (e.g. d_{h0} and d_{v0}) as the known design parameters and make the remaining two (e.g. s_h and s_v) variables, depending on the specific design task. In this example, the known parameters are selected as $s_h = 1.24$ mm and $s_v = 18$ mm mainly for machining reasons. The given SMA wire stroke in this example is determined as $\Delta x = 0.03 \cdot l_{SMA} = 4.35$ mm. A stroke of 3 % is a typical choice for SMA actuators to guarantee adequate performance and lifetime cycles [15]. The parameters d_{h0} and d_{v0} are the only unknowns in (3.36), which means they are directly linked to each other. The solution to this problem can be found graphically (Figure 3.23) with a program implemented in MATLAB. The relationship between d_{h0} and d_{v0} and their correlation to the needed SMA wire stroke for a full rotation is displayed in Figure 3.23 (upper part). As expected, the necessary stroke increases with higher values for these parameters. To visualize the fact that the maximum SMA stroke is given in this scenario, a plane parallel to the x-y-plane cuts the graph at the z-value of 4.35 mm (Figure 3.23, center part). The resulting intersection curve (Figure 3.23, lower part) represents the relationship between the two design parameters. In the next step it is analyzed, how the selection of these parameters affect the SMA forces during activation.

Kinetic Study

The study of the kinetics in this system looks at the forces and moments for a quasi-static case with the goal of finding values for the design parameters d_{h0} and d_{v0} that lead to low and preferably constant SMA forces. The equilibrium of moments includes the moments caused by the force of the tension spring and the force of the SMA wire. Friction forces are neglected in this example with respect to the bearings of the gripping arm. Also the weight of the gripping arm will cause different weight forces depending on the end-effector positioning. In the present example, it is assumed that the end-effector is held in a horizontal position for the reconfiguration process. In the application, this process always takes place without additional external loads. The SMA actuator wire is never exposed to additional stress, because once a workpiece is gripped, the end-effector structure carries the workpiece load.

In a first step, the force characteristics of the spring and the resulting moments are identified. Figure 3.24 (upper part) illustrates the kinetic system and the geometrical relationships. The attachment point of the spring at the end-effector base is described with x_{spr} ($x_{spr} = 0$) and y_{spr}. The pivot point "D" of the gripping arm defines the parameters x_{arm} and y_{arm}. The attachment point of the spring at the gripping arm is marked with "M".
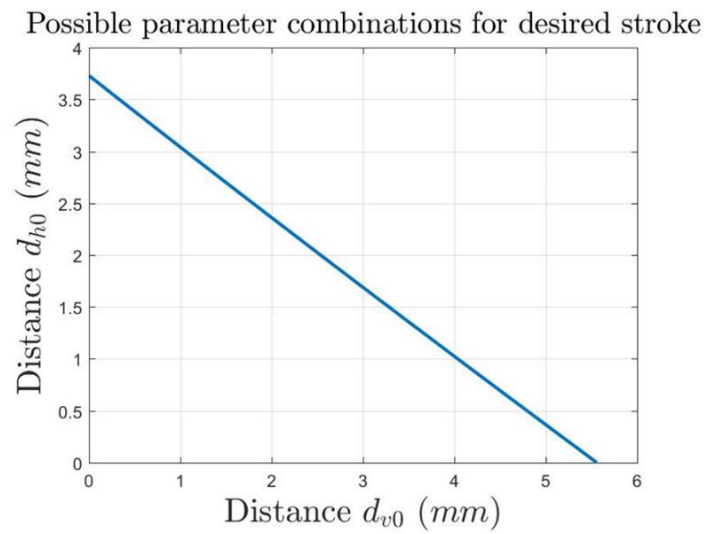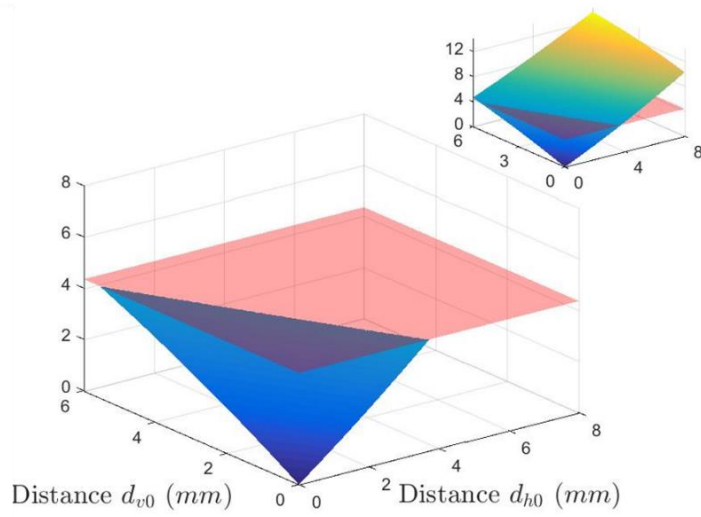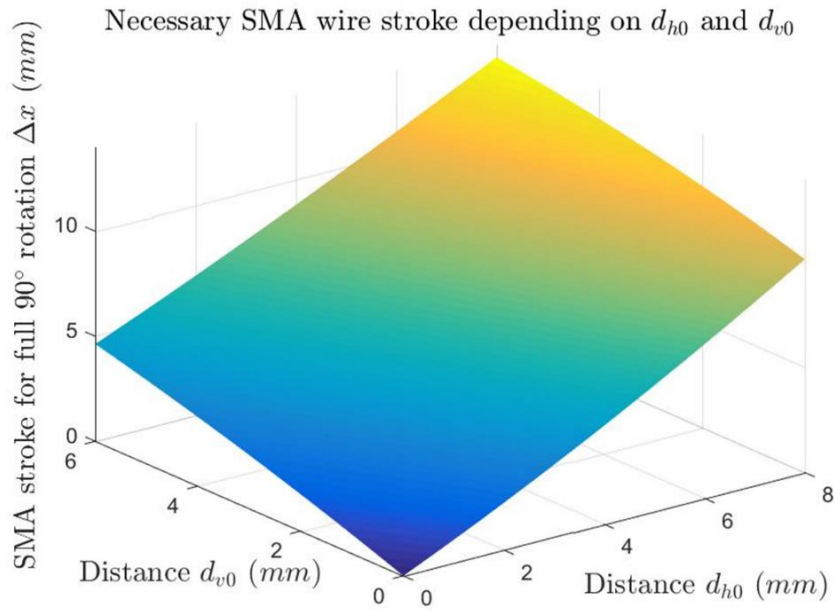
Figure 3.23: Graphical display of the design parameter relationships in the kinematic system (upper part). The given SMA stroke (center part) leads to a direct relation between d_{h0} and d_{v0} (lower part).
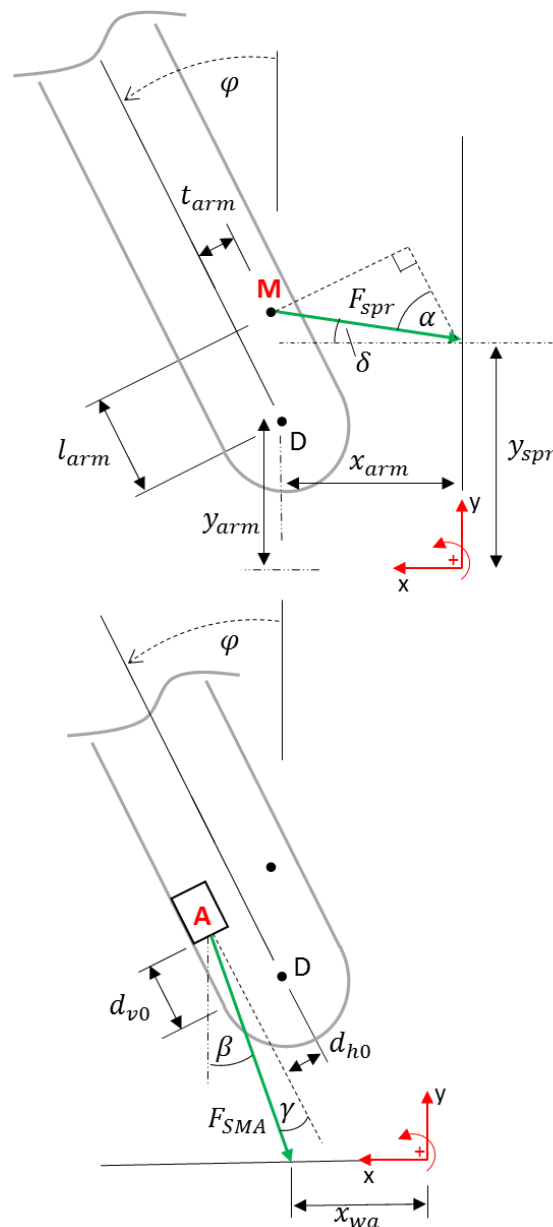
Figure 3.24: Sketch of the gripping arm to illustrate the geometrical relations for the spring force behavior (upper part) and the SMA force behavior (lower part) during rotation.

The path of this point along the rotational movement with the angle φ is responsible for the course of the moments M_{spr1} and M_{spr2} caused by the spring force F_{spr}. Two moments are the result of dividing the spring force into two components, one component parallel and one component perpendicular to the gripping arm during movement. The angle α is used to calculate these two force components. To determine the moments M_{spr1} and M_{spr2}, the geometrical parameters t_{arm} and l_{arm} are identified. They represent the horizontal and vertical distances between the spring attachment point M and the pivot point D of the gripping arm. With these parameters, the moments caused by the spring force can be described as:

$$M_{spr1} = l_{arm} \cdot F_{spr} \cdot \sin\alpha \tag{3.37}$$

$$M_{spr2} = t_{arm} \cdot F_{spr} \cdot \cos\alpha. \tag{3.38}$$

With the spring rate c_{spr}, the length of the spring during movement l_{spr}, and the initial length of the spring $l_{0,spr}$ the spring force is calculated with

$$F_{spr} = c_{spr} \cdot \left(l_{spr} - l_{0,spr} \right). \tag{3.39}$$

The length of the spring l_{spr} is described via the position of the attachment point M during the movement and is determined as

$$l_{spr} = \sqrt{x_M^2 + \left(y_M - y_{spr} \right)^2} \tag{3.40}$$

with

$$x_M = x_{arm} + \left(l_{arm} - \frac{t_{arm}}{\tan\varphi} \right) \cdot \sin\varphi \tag{3.41}$$

$$y_M = y_{arm} + \left(l_{arm} + t_{arm} \cdot \tan\varphi \right) \cdot \cos\varphi. \tag{3.42}$$

To calculate M_{spr1} and M_{spr2}, a relation between α and φ has to be found, therefore the angle δ is defined as

$$\delta = \tan^{-1}\left(\frac{y_M - y_{spr}}{x_M} \right). \tag{3.43}$$

The relation between α and φ is found to be

$$\alpha = \frac{\pi}{2} - \varphi - \delta. \tag{3.44}$$

As a result, the moments M_{spr1} and M_{spr2} are only dependent on the rotation angle φ and geometrical parameters.

The next step of the kinetic study looks at the moments resulting from the SMA force. The goal of the equilibrium of moments is to eventually find an equation for the behavior of the SMA force during the movement depending on the rotation angle φ and the design parameter d_{v0} (or d_{h0}). In analogy to the spring force, the relations for the SMA force are illustrated in Figure 3.24 (lower part). The position of the SMA wire guide in the end-

effector base is described with x_{wa} ($y_{wa} = 0$). The beginning of the SMA wire guiding in the gripping arm is marked with "A". The parameters d_{v0} and d_{h0} like in the kinematic study describe the distances from A to the pivot point. Like the spring force, the SMA force is divided in two components, one parallel and one perpendicular to the gripping arm during movement. The angle γ is used to calculate the SMA force components. The moments resulting from the SMA forces are

$$M_{SMA1} = F_{SMA} \cdot \cos\gamma \cdot d_{h0} \tag{3.45}$$

$$M_{SMA2} = F_{SMA} \cdot \sin\gamma \cdot d_{v0}. \tag{3.46}$$

To relate the angle γ to the rotation φ, the angle β is needed in

$$\gamma = \beta - \varphi \tag{3.47}$$

with

$$\beta = \tan^{-1}(\frac{x_A - x_{wa}}{y_A}). \tag{3.48}$$

The parameters x_A and y_A describe the position of point A during movement and are calculated with

$$x_A = x_{arm} + \cos\varphi \cdot \left(d_{h0} + d_{v0} \cdot \tan\varphi\right) \tag{3.49}$$

$$y_A = y_{arm} + \cos\varphi \cdot \left(d_{v0} - d_{h0} \cdot \tan\varphi\right). \tag{3.50}$$

With the equilibrium of moments $\Sigma M_i = 0$, and (3.37), (3.38), (3.45) and (3.46), the SMA force can now be described as

$$F_{SMA} = \frac{M_{spr1} + M_{spr2}}{\cos\gamma \cdot d_{h0} - \sin\gamma \cdot d_{v0}}. \tag{3.51}$$

Determination of the Design Parameters

This equation describes the SMA force as a function of the rotational angle φ and the design parameters d_{v0} and d_{h0}. With the help of (3.36) from the kinematic study, one of these parameters can further be eliminated. In our case, d_{h0} is eliminated and the rest of the parameters are set according to Table 7. The spring rate has to be selected strong enough,

so that the gripping arms are held in their initial positions, even when the end-effector is tilted. Possible dynamic forces caused by the robot movement are not addressed in this example.

Table 7: Construction Parameters of the End-Effector

Parameter	Value	Description
x_{arm}	40 mm	x-coordinate of the pivot point
y_{arm}	32 mm	y-coordinate of the pivot point
t_{arm}	5 mm	Initial horizontal distance: pivot point – spring attachment point M
l_{arm}	10 mm	Initial vertical distance: pivot point – spring attachment point M
y_{spr}	40 mm	y-coordinate of the spring attachment at the end-effector base
x_{wa}	38.32 mm	x-coordinate of the SMA wire guiding in the end-effector base
$l_{0,spr}$	22.35 mm	Initial length of the spring
c_{spr}	0.15 N/mm	Spring rate

The MATLAB tool is now used to visualize the SMA force behavior depending on φ and d_{v0}. Goal of these studies is to find values for d_{v0} and d_{h0} with regard to the necessary SMA force. Ideally, the force is nearly constant and has a low amplitude. Low forces allow the use of thin SMA wires, which results in higher actuation frequencies because of reduced cooling time. The results are displayed in Figure 3.25. The 3D-plot (Figure 3.25, upper part) shows the results of (3.51) with the SMA force as the z-axis, d_{v0} as the y-axis and φ as the x-axis. If d_{v0} is selected close to 0 mm, the SMA force is very low at the start of the motion but increases heavily towards the end of the 90 ° rotation. Conversely, a d_{v0} in the range of 5 mm leads to a high force at the beginning of the movement, which decreases rapidly to low values. To determine the desired value for d_{v0}, the 3D-plot is looked at from a position parallel to the y-z-plane (Figure 3.25, lower part). From this view, the point with the least variation of F_{SMA} can be identified with a y-value of 2.72 mm for d_{v0} and an SMA force of 13.63 N. As a result, it is now possible to design the rotary SMA actuator in this end-effector in a way that the SMA wire can work at a constant force, even though the moments are constantly changing during movement.

The remaining design parameter d_{h0} is obtained from (3.36) as d_{h0} = 1.88 mm. The force of 13.63 N dictates the choice of the SMA wire diameter. To reach a high number of lifetime

cycles, the mechanical stress in the SMA wire should not exceed 200 MPa [14], [15]. The calculated force is distributed among four SMA wires. The chosen SMA wire diameter of 150 µm results in a mechanical stress of 192 MPa. Note, that the presented design method is not limited to this specific example, but can very well be used to investigate the effect of parameter variations of any of the declared parameters in Table 7.
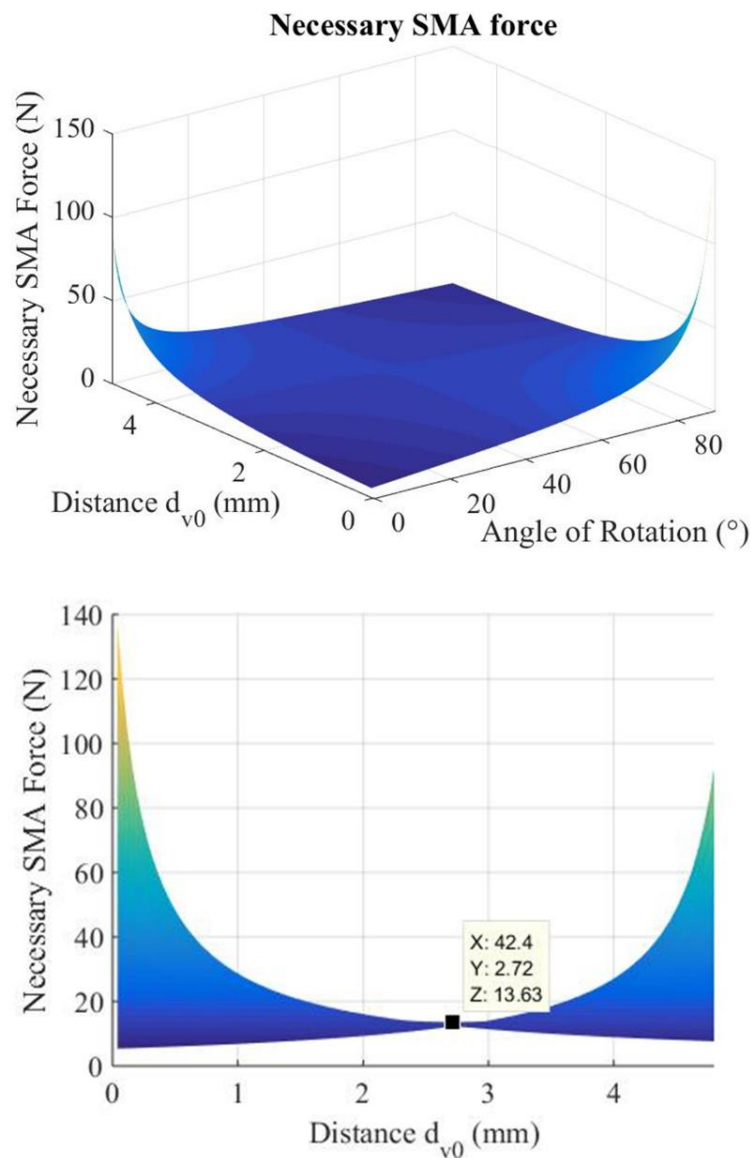
Figure 3.25: Behavior of the SMA force in relation to the design parameter d_{v0} and the angle of rotation (upper part) and identified design parameter for near constant SMA force during complete activation (lower part).

3.3.2 **End-effector Characterization and Validation**

The schematic of the setup used for the characterization of the actuators is shown in Figure 3.26. Current sources are used to activate the SMA wires in both DOFs. The rotational angles are measured with two Hall sensors (ams AS5048B). For this purpose,

permanent magnets are integrated into the joints of the aluminum structure. In addition, the electrical resistance of the SMA wires is measured during activation. The setup is controlled by a LabView and a NI cRIO system.
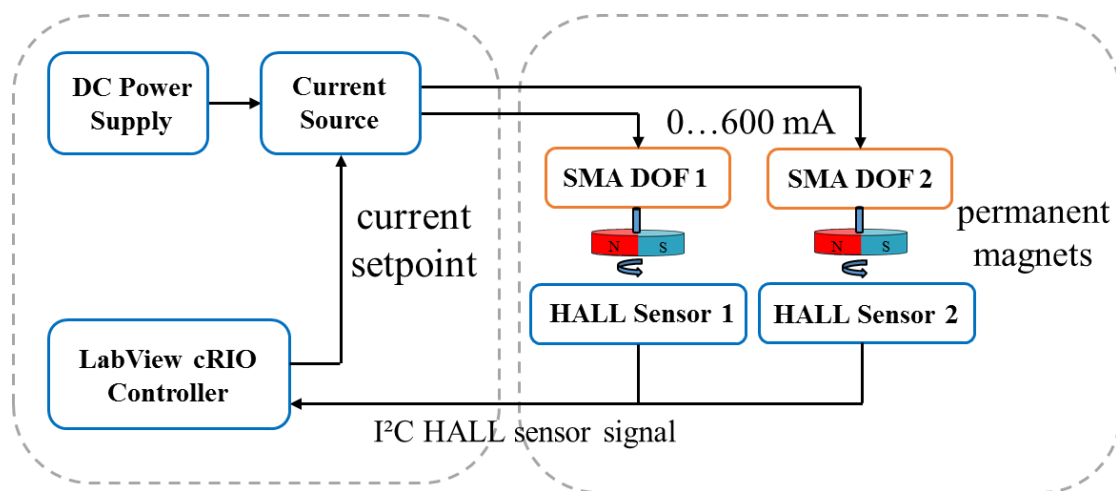
Figure 3.26: Characterization and validation setup for the SMA actuators in both degrees-of-freedom of one end-effector arm.

The characterization measurements of the first DOF are displayed in Figure 3.27. Column (a) shows the activation current signal (upper part), the rotational angle over time (center part) and the electrical resistance over time (lower part) for the first DOF. Column (b) shows zoomed-in graphs of the rotation (upper part) and the resistance (lower part) signals.

The SMA wire is activated for 10 s by a suggested electrical current of 400 mA [14], which is then stepwise increased to 500 mA and 600 mA. The gripping arm reaches its maximum rotational angle after about 4 s, but only with a current of 600 mA a full 90 ° rotation is achieved, which corresponds to the desired rotational angle. The transition temperature of the SMA wire increases with increasing stress. The joule heating below 600 mA is not sufficient for a full rotation. After the current is turned off, the gripping arm takes about 6-7 s to return to its initial position. The electrical resistance of the SMA wire first increases because of the rising temperature in the wire. As soon as the phase transformation takes place and the gripping arm begins to move, the resistance starts decreasing as expected [24]. The zoomed-in graphs in column (b) also indicate that little irregularities causing friction can be seen in the rotation signals as well as in the according resistance measurements.

Characterization DOF 1
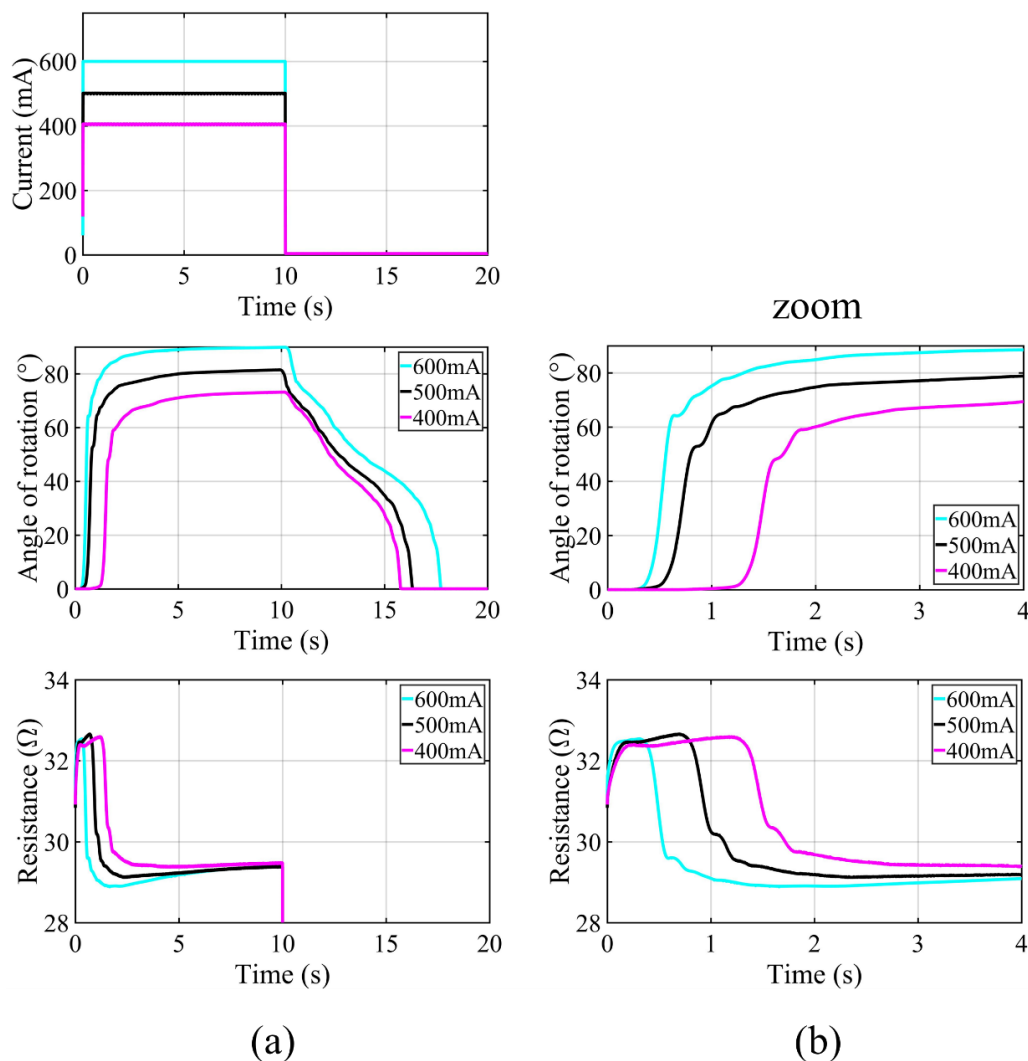
Figure 3.27: Current input (upper part), rotational angle (center part) and electrical resistance (lower part) for the first DOF (a) with zoomed-in graphs (b).

Figure 3.28 shows the characterization of the second DOF. This actuator uses the same SMA wire diameter, so the same electrical currents are applied for activation. The target rotational angle of 30 ° is reached in about 7 s with a current of 500 mA and in about 3 s with a current of 600 mA. The teeth of the locking mechanism design can be seen as steps in the rotation signals as well as in the resistance signals. The first step occurs at about 15 ° rotation with an SMA resistance of 7.5 Ω. At 400 mA the tilting arm is not able to move past the last step of the locking mechanism and after the current is turned off, it stays at the 20 ° rest position.

The measurements of the rotational movement validate the functionality of both SMA actuators. The purpose of the resistance measurements is the exploration of the SMA actuators' "self-sensing" abilities.

Characterization DOF 2
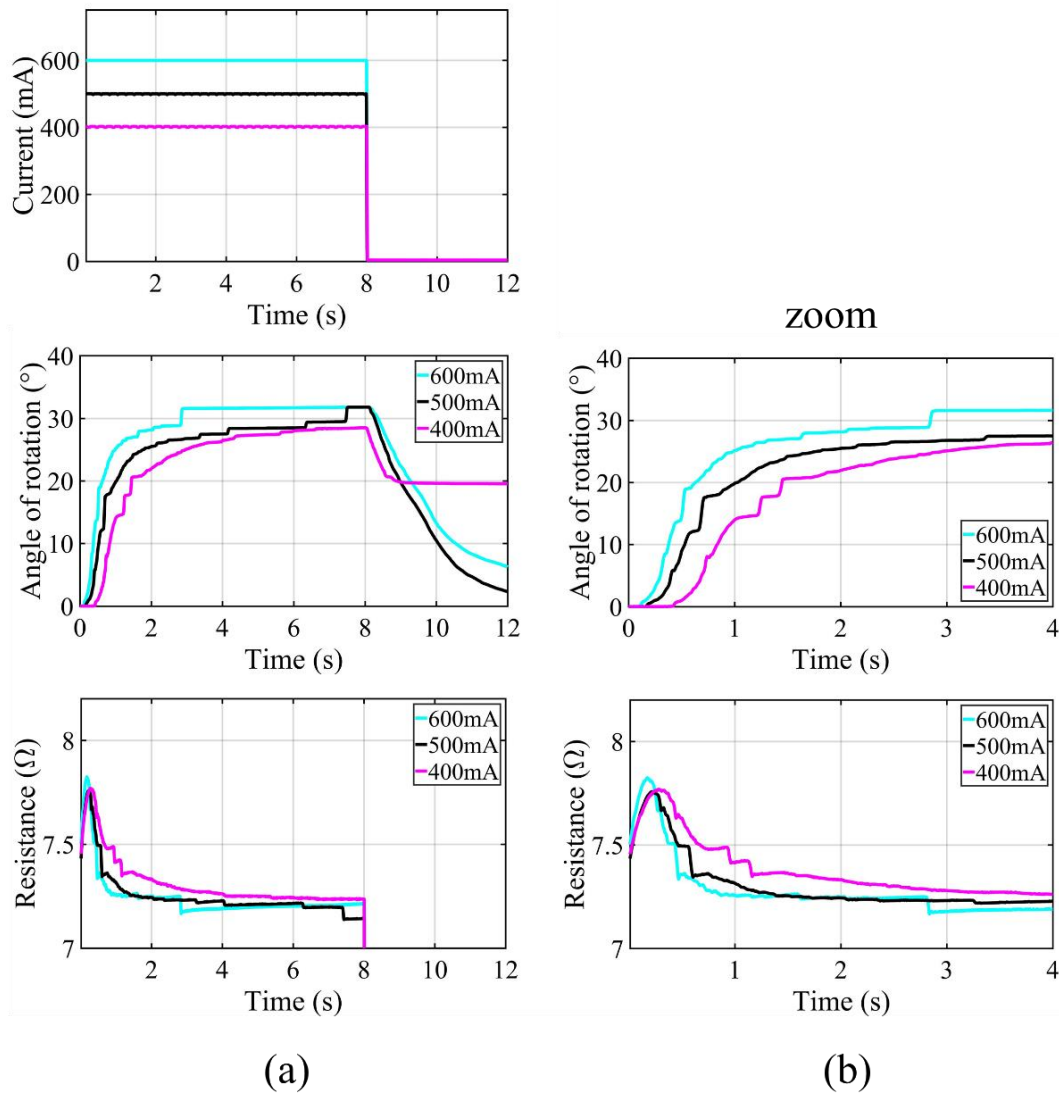
Figure 3.28: Current input (upper part), rotational angle (center part) and electrical resistance (lower part) for the second DOF (a) with zoomed-in graphs (b).

For condition monitoring purposes, a resistance measurement is a simple method to detect, if an SMA actuator is destroyed. In the case of the second DOF, the resistance signal could be used to detect, if the tilting arm has passed the steps of the locking mechanism and reached the desired rest position. The final aim is to use the change of resistance as the feedback signal for position control of the SMA actuators. The correlation between SMA resistance and rotational angle for the first DOF is shown in Figure 3.29 (upper part). For all three current levels, the SMA wire shows the same relation between 0 ° and the maximum angle reached. After the gripping arm reached its maximum displacement, the resistance of the SMA wires starts increasing again because of a rising temperature in the wire. To demonstrate the position control of SMA actuators, a PI controller using the Hall

sensor signal feedback is realized for the first DOF. The result is displayed in Figure 3.29 (lower part). Without going into further detail, the general feasibility of applying position control to the SMA actuator is shown.
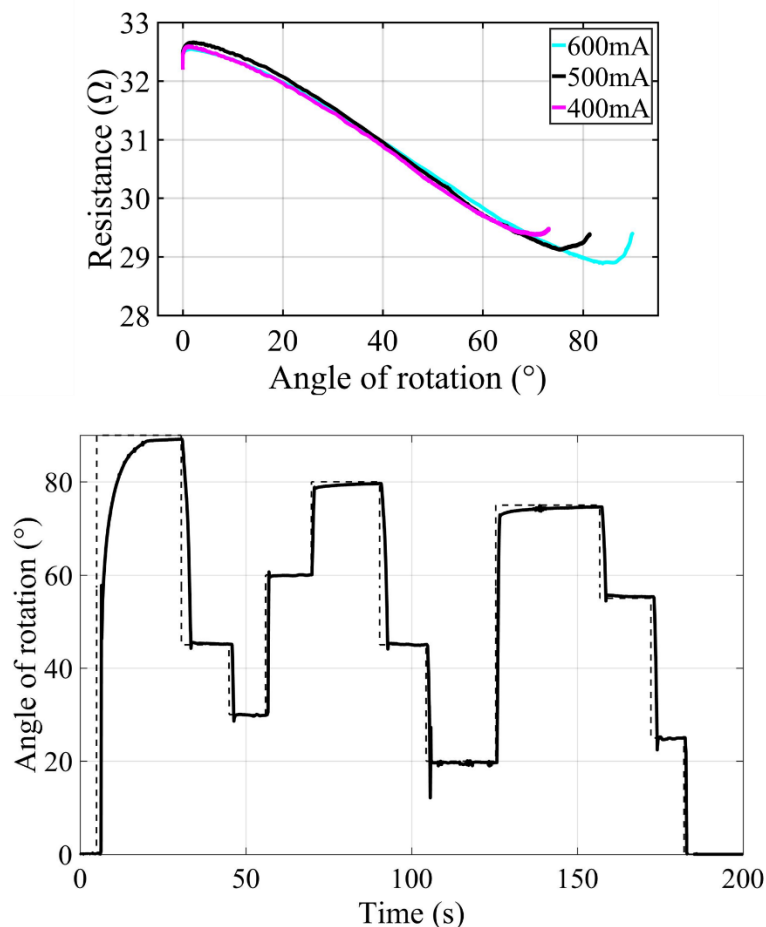
Figure 3.29: Position control of the first DOF using a PI controller with Hall sensor feedback.

3.4   Summary and Future Work: Applied SMA Actuator Design

This chapter presents systematic design frameworks including graphical design tools for SMA wire based linear and rotary actuators at the example of two possible applications. In the case of the suction cup, the energy-efficiency is improved by using a different kinematic concept and the actuator frequency could be enhanced by an SMA wire configuration with multiple windings. In future work, the membrane geometry of the suction cup has to be modified in order to produce higher quality vacuum. Additionally, the SMA wire's self-sensing ability could be exploited for monitoring of the vacuum quality. Finally, the advanced kinematic concept presented in chapter 4 implemented in the next prototype will result in a gripping system optimized in terms of energy-efficiency and dynamics.

The end-effector design includes a locking mechanism that allows energy-free holding of defined positions. The reconfiguration process of an end-effector always takes place without additional external loads. Once a workpiece is gripped, the end-effector structure has to carry the workpiece's weight, but the SMA actuator is not exposed to additional stress. In case of the presented SMA actuators, the SMA wires of the first DOF have to be constantly heated to hold the desired position until a workpiece is gripped. The next improvement of the design thus includes either an additional locking mechanism for the first DOF that allows energy-free holding of the desired gripping position or, instead of retaining the SMA wire-spring configuration, an antagonistic design using two SMA wires could also be an option [125]. The locking mechanism would also address possible dynamic forces on the gripping arms while the end-effector has not gripped a workpiece. Furthermore, future work will include the development of a position control using the SMA wires' self-sensing ability.

4   Advanced SMA Actuator Concepts - Bi-stable Spring Design

Chapter 3 has presented a systematic design scheme for linear spring SMA actuators at the example of two possible applications. This chapter introduces an advanced actuator concept, which uses a bi-stable spring element in combination with two antagonistic SMA wires instead of a linear spring configuration. This SMA actuator comes with advantages concerning energy-efficiency and actuation speed because it is able to hold two positions without consuming energy and the antagonistic SMA wire configuration can result in very high switching frequencies. In addition, output strokes can be increased by an order of magnitude and more. This chapter is based on [129]–[132].

4.1   Motivation for Bi-stable Spring Actuators

The development of a bi-stable SMA actuator is motivated by all three mentioned drawbacks of current SMA actuators, which are limited stroke, low actuation frequency and high energy consumption. The bi-stable concept presented in [129], [130] is based on integrating a hinged bi-stable element into an antagonistic SMA wire configuration. The rotary mounting of the bi-stable element is key in this invention because it allows the attachment of SMA wires in technically relevant positions. SMA wires produce extremely high force and only moderate stroke, which can be ideally used here by placing the wires close to the hinge pivot point. A simple configuration is displayed in Figure 4.1, in which a buckled beam is used as the bi-stable element and hinged on both ends. SMA wires are attached on both sides of one of the hinges. Contraction of one SMA wire results in a moment and eventually snapping of the bi-stable element. At the same time, the other SMA wire is stretched and ready for activation. The output stroke is measured at the center of the beam. The closer the SMA wires are attached to the pivot point, the less SMA stroke is necessary for a snapping of the bi-stable beam. This allows for high stroke transmission ratios and less design restrictions by the SMA's transformation strain. The antagonistic SMA wires allow, in contrast to a passive spring force, active deformation in both directions, which results in higher actuation frequencies. The switching between the two actuator positions requires only short activation pulses, so that energy consumption is drastically reduced. Finally, a large variety of actuator designs regarding the geometry and the SMA wire attachment is possible because of the pivotal mounting of the bi-stable

element (Figure 4.2), which allows for application specific or custom-fitted design of the SMA actuator.
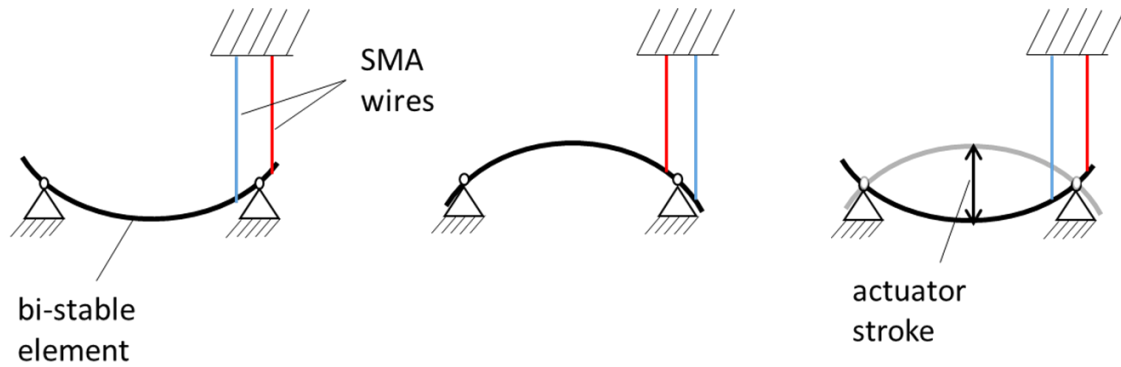
Figure 4.1: Exemplary simple configuration of a bi-stable SMA actuator. A beam is hinged on at both ends and an SMA wire is attached on both sides of one of the hinges [131].
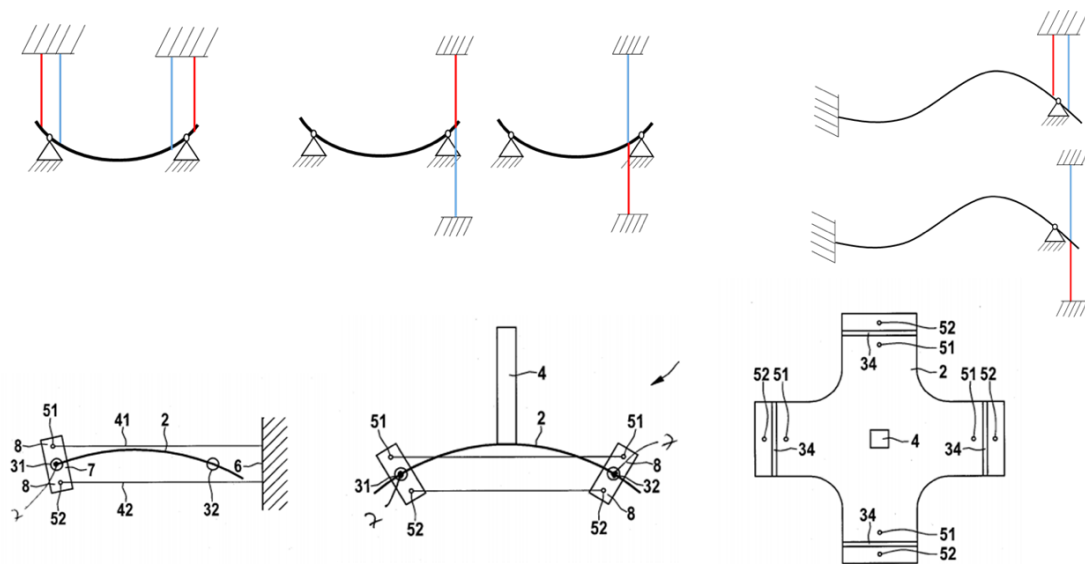
Figure 4.2: A variety of possible bi-stable SMA actuator configurations with SMA wires attached perpendicular (upper part) [131] or horizontally (lower part) [129] to the bi-stable element.

4.2 Bi-stable Spring Fundamentals

This section introduces the basics of mechanical stability problems and fundamental characteristics of hinged bi-stable springs. A short overview of the state-of-the-art of bi-stable SMA actuators is given and an early technology demonstrator of the bi-stable spring design is presented.

4.2.1 **Mechanical Stability Problems**

An equilibrium position of a system is called stable, if movement caused by a minimum excitation of the system stays in a defined range around this equilibrium position at all times. Excitation of a system in an unstable equilibrium in contrast results in the system leaving the equilibrium [133]. Critical load conditions can lead to stable equilibrium positions losing stability as well. For loss of stability, three categories are distinguished:

- Reaching of the maximum load
- Bifurcation problems
- Mechanical breakthrough problems

Reaching or exceeding of the maximum load usually causes plastic deformation and the creation of a plastic hinge region, which makes the system statically indeterminate. This leads to instability and generally destroys the system [134].

In bifurcation problems, more than one load-displacement characteristic is possible when exceeding a critical load. A typical example is displayed in Figure 4.3. A column is hinged at both ends and exposed to a load P. If P exceeds a critical value, the column starts to buckle to one side. Theoretically, the column can buckle in positive or negative ζ-direction, so the load-displacement characteristic shows a bifurcation with two possible paths. In a technical system, little imperfections in the system decide the direction of the buckling [134].
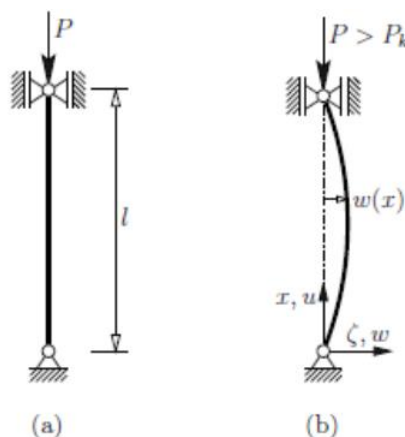
Figure 4.3: A narrow column hinged at both ends, in a straight and stable state (a) and in a buckled and stable state [134].

Mechanical breakthrough describes the abrupt change from one equilibrium position to another when surpassing the stability limit [134]. Figure 4.4 shows an example of a column system. The load-displacement diagram (d) indicates a jump in the characteristic under load

control. The complete characteristic can be recorded in a displacement-controlled experiment, which suppresses the mechanical breakthrough. The maxima in this diagram are called points of breakthrough [134]. The crucial parameters in strength calculations are Euler's critical load P_k and the column deflection $w(x)$ [135]. These deflections can be analytically determined with the Euler-Bernoulli theory, which is only valid for infinitesimal strains and small rotations, like in non-deformed systems [136].
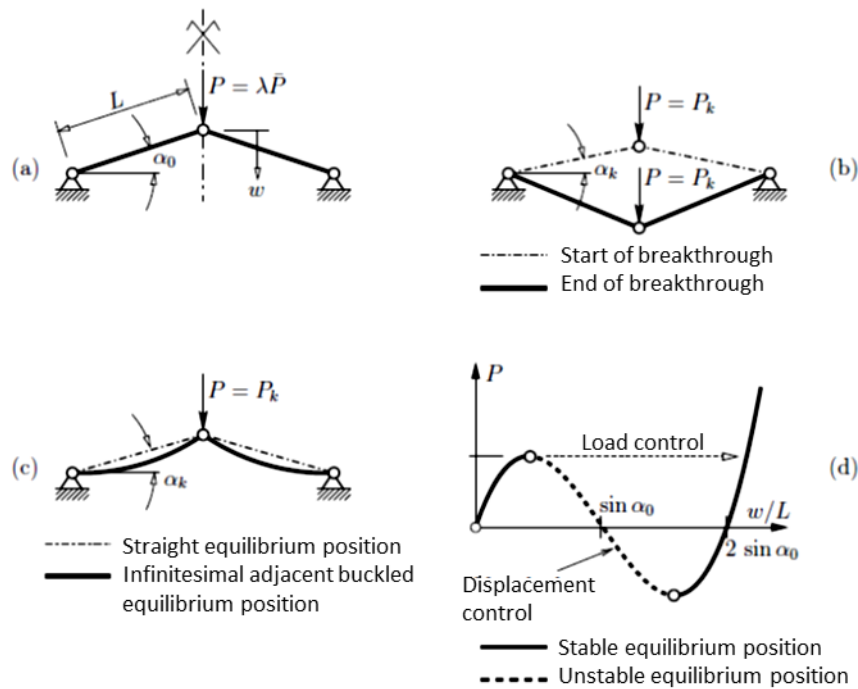
Figure 4.4: Static column system (a), column system breakthrough (b), equilibrium bifurcation (c) and qualitative load-displacement diagram (d) [134].

4.2.2 Hinged Bi-stable Beams

The bi-stable elements considered for SMA actuator systems do not meet the requirements for Euler-Bernoulli (4.2.1). For the description of large strains, the elastica theory suggests a nonlinear differential equation which cannot be solved analytically [134]. Approximated solutions can be found numerically [137], for example with the finite element method (FEM). The curvature of the beams results from the bending modes displayed in Figure 4.5. The first three modes are named according to their shape (U-, S- and W-shape).
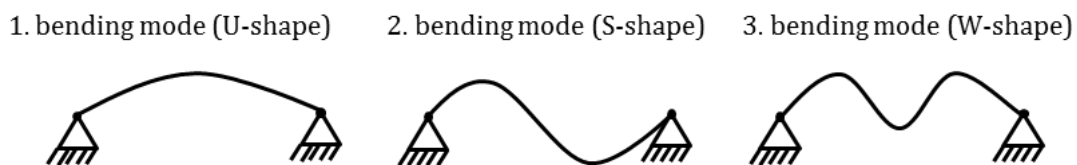
Figure 4.5: The first three bending modes of a hinged beam.

Figure 4.6 shows the numerical calculation of a qualitative force-displacement characteristic for a hinged bi-stable beam (displacement controlled). The force application is in the center of the beam. The stable bending modes in this case are mode 1 (U-shape) and mode 2 (S-shape) (red path). The dashed path presents the instable form of the W-shape [137]. Validation of the theoretical estimations shows discrepancies in the actual forces, because the real boundary conditions are hard to predict. Loads at defined application points are not feasible in a real system. In Figure 4.7, the maximum force in relation to the force application point along the beam is calculated and validated by experiments. Minimum forces occur at a distance of about 30 % of the beam length from the hinges. The characteristic shows a local force maximum at the beam's center [138].
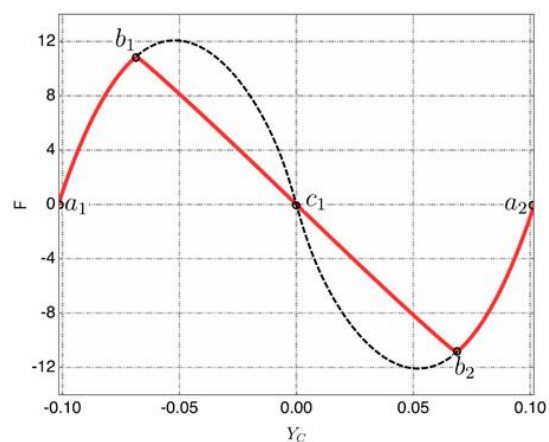
Figure 4.6: Force-displacement characteristic of a bi-stable beam with a force application at its center. The red path shows the stable bifurcation branch for displacement controlled deformation. The dashed path shows the instable branch with a higher energy level [137].
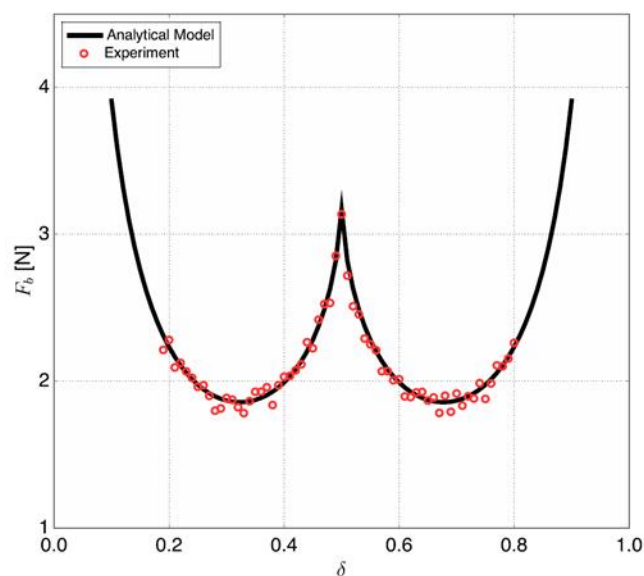
Figure 4.7: Maximum force at the point of breakthrough for a hinged bi-stable beam with displacement controlled deflection in relation to the lateral position of the force application point (beam center: $\delta = 0.5$) [138].

4.2.3 **Bi-stable SMA Actuators: State-of-the-Art**

Bi-stable systems and also systems using buckled beams are popular in MEMS applications [139]–[141]. The usage of bi-stable elements in combination with SMA actuators has been proposed in [142], [143]. The main difference of the bi-stable system proposed in this work in comparison to the state-of-the-art is the pivotal mounting of the bi-stable element. In case of the hinged beam, the center of the beam can be used for output force and displacement, but the SMA wires can be attached in antagonistic configuration on the same side of the beam, in close distance to the pivot points. A first functional technology demonstrator is displayed in Figure 4.8. The closer the attachment point of the SMA wires to the pivot point, the less wire contraction is necessary to force a snapping of the bi-stable beam. This allows for the construction of very compact, fast and energy-efficient SMA actuator systems. Other possible configurations of hinged bi-stable elements and SMA wire actuators are presented as well as preliminary characterization measurements are presented in [129]–[131].
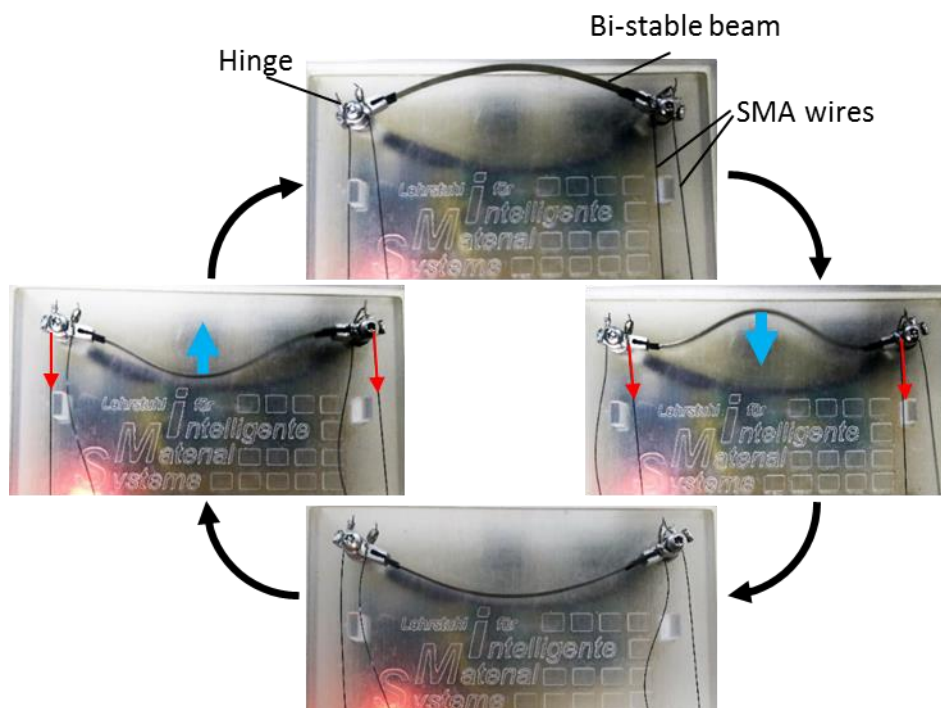
Figure 4.8: Functional technology demonstrator of a bi-stable SMA actuator.

4.3 **Experimental Setup**

For the design of actuators with hinged bi-stable spring elements, the design parameters are experimentally evaluated. Based on systematic experimental data, design rules can be established and parameters can be validated for FEM based simulation tools. The experimental setup aims at analyzing the torque necessary to force a snapping of the bi-

stable element, depending on the lever arm by varying the wire attachment point. Additionally, the necessary stroke for a snap-through as well as the output stroke at the center of the beam is measured.

4.3.1 Design of the Experimental Setup

A schematic of the experimental setup is shown in Figure 4.9. A linear actuator is able to pull on a bi-stable spring, like an SMA wire would if activated. The mechanical connection of the linear actuator with the bi-stable spring includes a load cell (Futek LSB200 5 lbs) to measure the pulling force. It also contains a linear air bearing to compensate for torque created by asymmetrical pull on the bi-stable spring. Steel cables are used to connect the boom to the spring element. The linear actuator has an integrated position encoder and is controlled by an Aerotech Ensemble CP 10-MXU controller. A laser displacement sensor (Keyence LK G-87) measures the displacement of the bi-stable spring. The experiments are run via an NI cRIO system and LabView, which is also used for the data acquisition. To guarantee minimal friction during the experiments an air bearing model NEWWAY S-302502 for shafts with a diameter of 13 mm is chosen. The CAD model of the experimental setup is displayed in Figure 4.10

The mount for the bi-stable spring is the key component of this setup. It has to comply with the following specifications:

- Spring has to be able to move freely starting at the axis of rotation
- Minimal friction in the hinges
- Variable points of force application and lever arms
- Continuous, reproducible adjustment of spring pretension
- Possibility of different spring lengths (45-55 mm)

The CAD model of the spring mount with its components is displayed in Figure 4.11 (upper part). The base has an inverted V-guide for the slider, which can be positioned precisely with an adjustment screw. With this mechanism and an integrated Nonius or Vernier scale, the mount can be accurately and reproducibly adjusted to different spring configurations. The clamping screw is used to lock the slider in its position. The hinges are realized by two ball bearings (SKF 618/4) per hinge to guarantee minimum friction and compensate for lateral torque. The spring is mechanically attached by two clamps, but is able to move freely between the two axes of rotation. A hole pattern in the clamps enables the variation of the lever arm between 0.5-2.5 mm in steps of 0.5 mm in both directions of the pivot point.
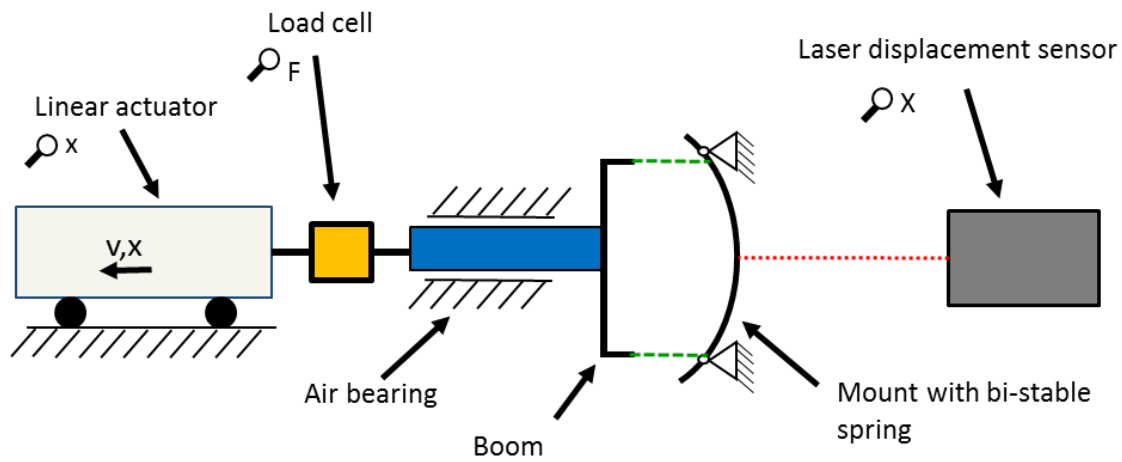
Figure 4.9: Experimental setup concept for one-sided or double-sided pull on a bi-stable spring element.
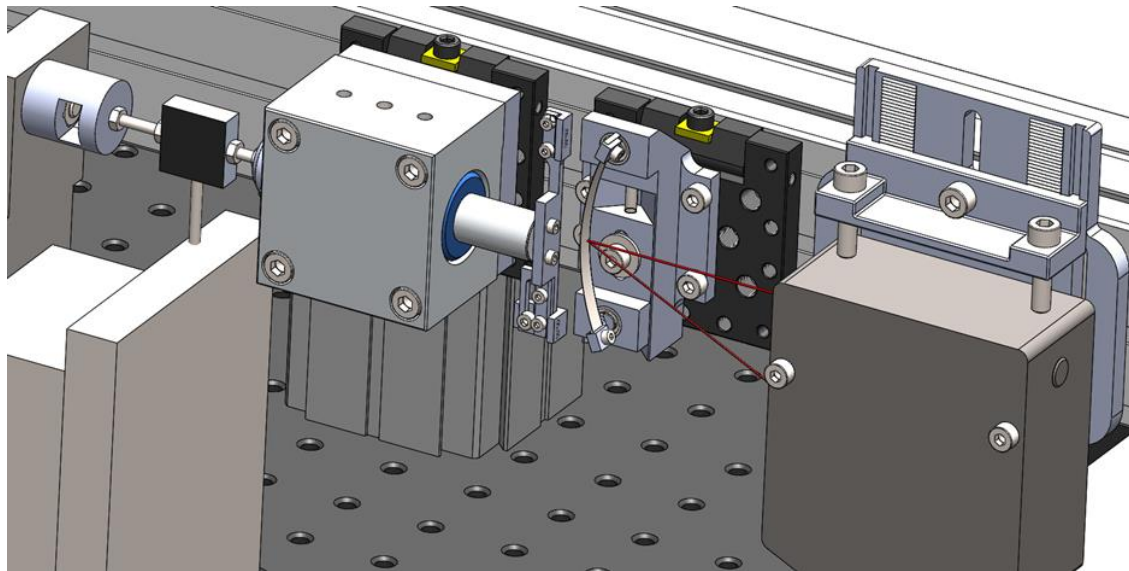
Figure 4.10: CAD model of the experimental setup for the evaluation of bi-stable springs.

The assembled mount with a clamped bi-stable spring is shown in Figure 4.11 (center part). The hole patterns of the spring clamps have to align with the same pattern on the boom (Figure 4.11, lower part). In analogy to the slider on the spring mount, the boom has to have one adjustable side. The steel cables are mechanically attached behind the hole patterns by clamping jaws.

The bi-stable spring specimens used in the experiments are 5 mm wide and have different lengths (Figure 4.12). The active or free length of these springs is the distance between the two pivot points, if the spring is clamped with zero pretension. The actual length of the specimen is always 10 mm longer than its free length.
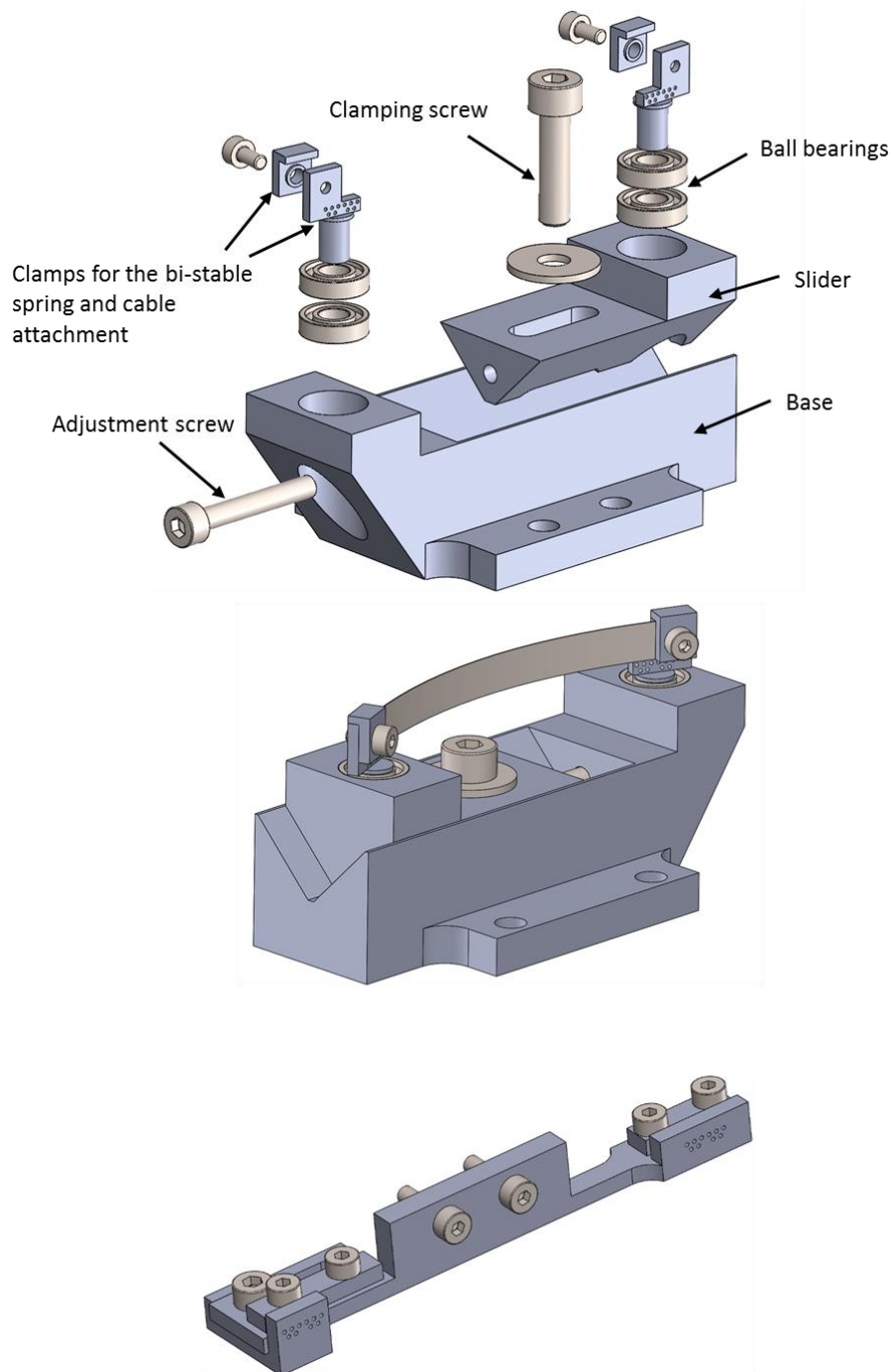
Figure 4.11: CAD model of the bi-stable spring mount (upper part), the assembled mount with clamped bi-stable spring (center part) and the boom for one-sided or double-sided pull (lower part).

In the experiments, free lengths of 47.5 mm, 50 mm, 52.5 mm and 55 mm are compared. The holes at both ends of the springs ensure a form fit and reproducible clamping of the specimens. Furthermore, three spring thicknesses (50 µm, 70 µm, 100 µm) and two steel types (1.1274 (C100S), 1.4310 (X12CrNi17-7) [144], [145]) are used as variations. Additionally, a superelastic NiTi alloy spring with a thickness of 110 µm is compared with the 1.4310 steel. In contrast to spring steel, which has a Young's modulus of approximately 200 GPa, the superelastic NiTI comes with a Young's modulus of around 50 GPa.
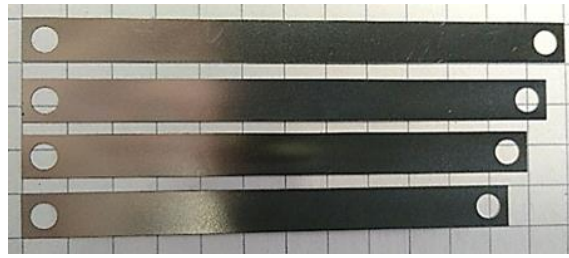
Figure 4.12: Four bi-stable spring specimens with free or active lengths of 55 mm, 52.5 mm, 50 mm and 47.5 mm.

The assembled setup and detailed views of the spring mount and the steel cable attachment are displayed in Figure 4.13. The steel cable has a diameter of 0.36 mm. On the side of the spring mount, the steel cable is attached by a knot bigger than the hole diameter (Figure 4.13, lower part). The knot is additionally fixated in one position with a drop of superglue. For double-sided pull experiments, test experiments have to be run to ensure symmetrical attachment of both steel cables.
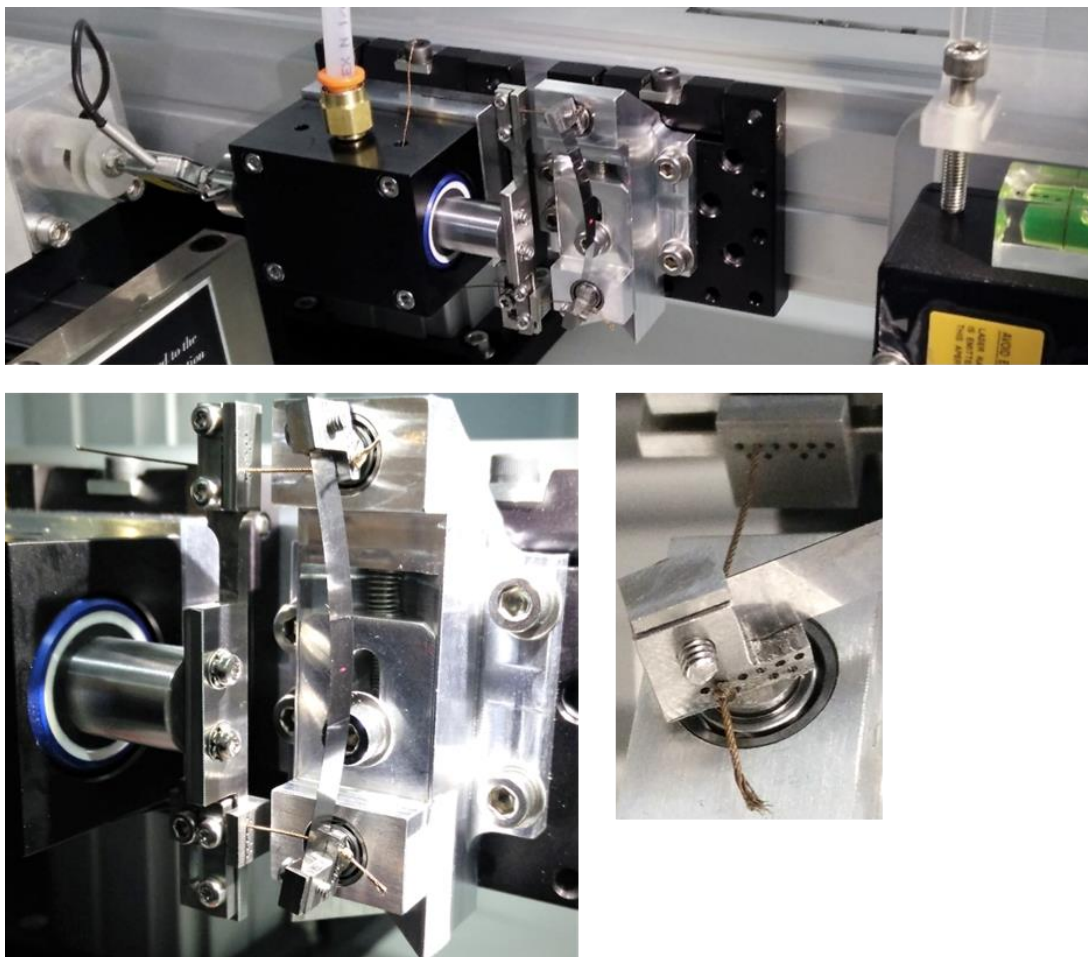
Figure 4.13: Experimental setup with a clamped bi-stable spring ready for a double-sided pull experiment (upper part) and detailed views of the spring mount and the boom as well as the steel cable attachment (lower part).

Before each experiment, the two end positions of the bi-stable spring are measured with the laser displacement sensor. These values serve as termination conditions for the LabView program. With the start of the experiment, the linear actuator starts moving at a speed of 0.1 mm/s. The measured variables are time, actuator position, displacement signal of the bi-stable spring and pulling force. The experiment ends when the bi-stable spring snaps through and reaches its second end position.

4.3.2 Validation of the Experimental Setup

A number of different experiments are conducted to determine the systematic errors and possible random errors during measurement. The system rigidity as well as the system friction is evaluated, so that the measurement results can be post-processed to show only actual behavior of the bi-stable spring. In addition, the reproducibility of the experiments is validated.

To measure the system rigidity, a steel plate with a thickness of 1.5 mm is clamped on the mount instead of a spring. The lever arm for this pull experiment is 0.5 mm. The laser displacement sensor monitors the displacement of the steel plate, which should not move in this experiment. The measurement results of the one-sided pull and the double-sided pull experiment are displayed in Figure 4.14.
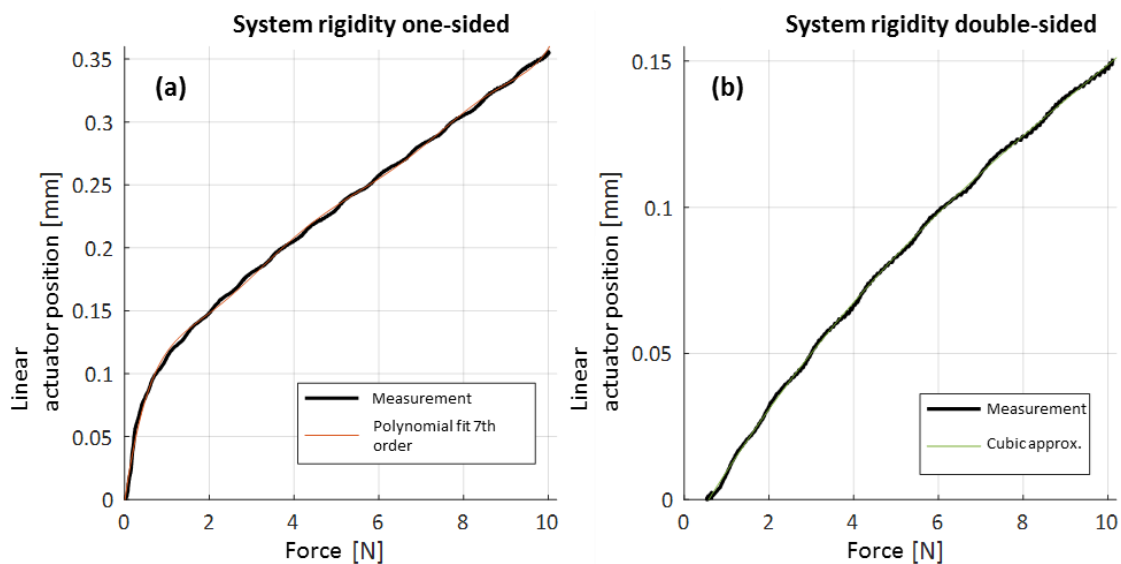
Figure 4.14: Determination of the system rigidity for the one-sided pull (a) and the double-sided pull (b).

While the steel plate shows zero displacement, the position of the linear actuator equals the deformation of the system. For the one-sided pull, the system rigidity characteristic can be fitted by a 7th order polynomial (a). The rigidity for the double-sided pull (b) is much higher

and can be fitted by a cubic function. Both approximations are used to subtract this systematic error in the measurements. The reason for much larger deformations in the one-sided pull experiment is that the system rigidity is predominantly dependent on the steel cable. The length of the steel cables used for these validation measurements remains the same throughout all experiments.

The determination of the system friction is done in an experiment without an installed spring element. The steel cables are attached to the hinges with a lever arm of 2.5 mm. During the experiment, the hinges are rotated for about 90 °. The combined friction forces of the air bearing and the four ball bearings are in the order of the signal noise with a maximum amplitude of 0.02 N (Figure 4.15) and thus can be ignored in the experiments.
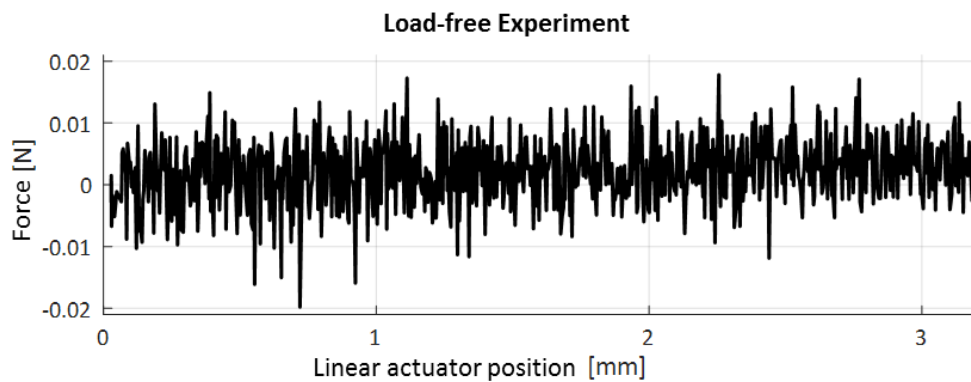
Figure 4.15: Result of an experiment without a mounted spring for the determination of the system friction.

The evaluation of reproducibility is conducted with a 1.1274 bi-stable spring with the free length $L_0 = 47.5$ mm and thickness $t = 0.07$ mm. The pretension of the spring is realized by the adjustment screw and the Vernier scale. For the validation of reproducible pretension, the bi-stable spring displacement resulting from the applied pretension is measured by the laser displacement sensor. The pretension of the bi-stable spring is increased to a defined value and reduced to the initial value five times and the maximum displacement of the spring is compared. First, the pretension is increased from zero to 1 mm, then from zero to 2 mm and lastly from 1 mm to 2 mm. The measurement results are displayed in Table 8. Pretensions of 1 mm (2 %) and 2 mm (4 %) lead to a standard deviation of 0.03-0.05 mm for the maximum spring displacement.

Table 8: Repeatability of the pretension mechanism measured by the maximum deflection at the center of the bi-stable spring in mm.

| | Variation of the Pretension | | | |
| | 0 mm - 1 mm | 0 mm - 2 mm | 1 mm - 2 mm | |
Repetition			1 mm	2 mm
1	8.43	12.01	8.49	12.00
2	8.47	12.00	8.35	12.04
3	8.36	12.09	8.38	12.04
4	8.45	12.02	8.43	12.07
5	8.49	12.07	8.35	12.00
Arithmetic mean:	8.44	12.04	8.40	12.03
Standard deviation:	0.05	0.04	0.05	0.03

The effect of removing a spring and installing a new spring between experiments is evaluated in Figure 4.16. In between each of the three measurement cycles of this double-sided pull experiment, the bi-stable spring is removed and reinstalled. For possible applications, mainly the maximum values of the force and the displacement are of interest and no relevant error is measured in these maximum values.

The springs used in the experiments are cut from metal sheets. It is possible, that through production and storage of these sheets, the bi-stable springs could develop preferred directions for bending or snapping. For this reason, the bi-stable spring is longitudinally turned between two measurements and the results are compared in Figure 4.17. Again, no relevant difference is observed.
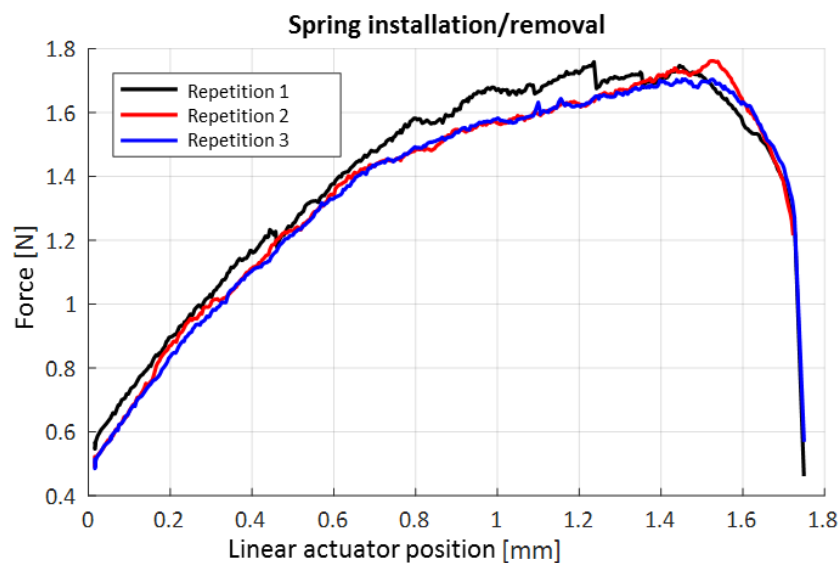
Figure 4.16: Influence of the removal and installation of a bi-stable spring on the measured characteristic ($t = 0.07$ mm, $L_0 = 47.5$ mm, $\Delta L = 2$ mm).
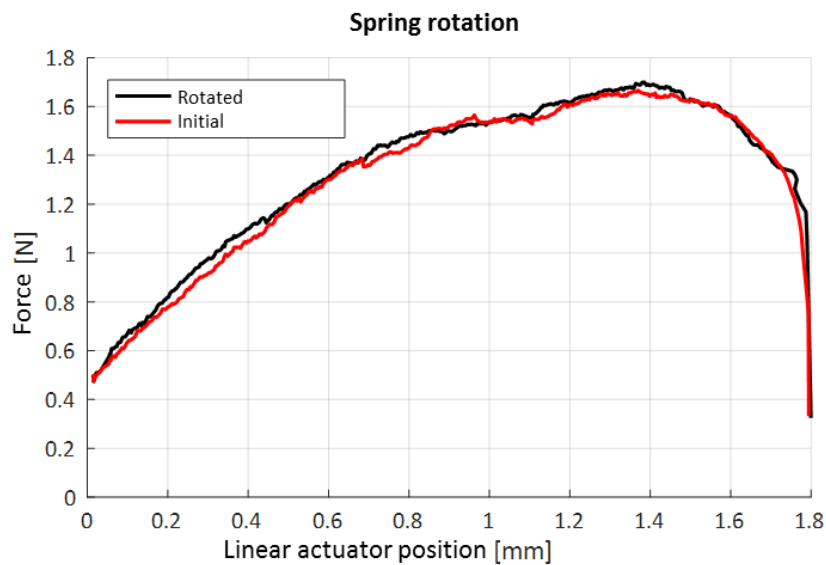
Figure 4.17: Influence of longitudinal turning of the bi-stable spring on the measured characteristic ($t = 0.07$ mm, $L_0 = 47.5$ mm, $\varDelta L = 2$ mm).

For the one-sided pull experiments, the steel cable can be attached at either the top hinge or the bottom hinge. Therefore, several experiments are conducted with both hinges and the results are compared. The difference in the force characteristic is exemplary displayed in Figure 4.18. Around the displacement of 0.4 mm, the force characteristic shows a different behavior. The maximum values of force and displacement, which are the most relevant for actuator design, are almost identical. Therefore, the top hinge is always used for the subsequent one-sided pull experiments.
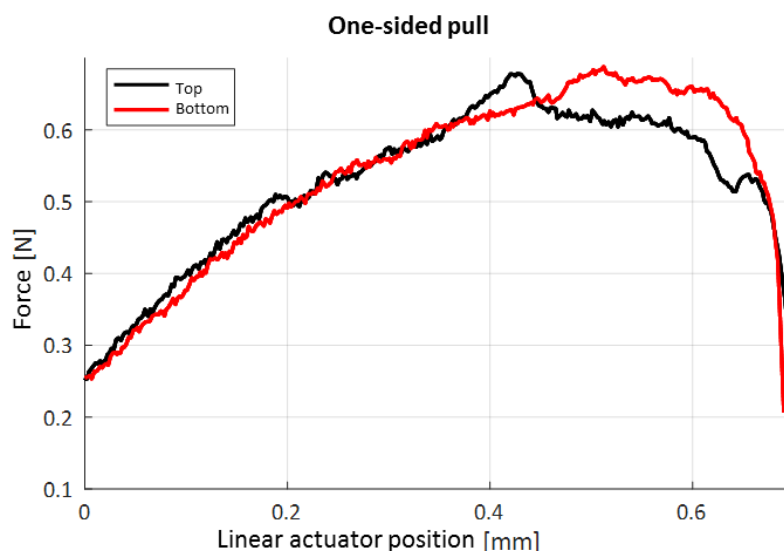
Figure 4.18: Comparison of the spring characteristic for the one-sided pull experiment on the top (black) and the bottom (red) hinge ($t = 0.07$ mm, $L_0 = 52.5$ mm, $\varDelta L = 1$ mm).

In the double-sided pull experiments, the two steel cables might be attached with a different pretension. A difference in pretension between the top and the bottom cable attachment results in an asymmetrical bending of the bi-stable spring. The influence of the spring bending symmetry is displayed in Figure 4.19. Symmetrical bending (red) results in higher forces and higher strokes. The subsequent double-sided pull experiments are exclusively conducted for symmetrical steel cable attachment.
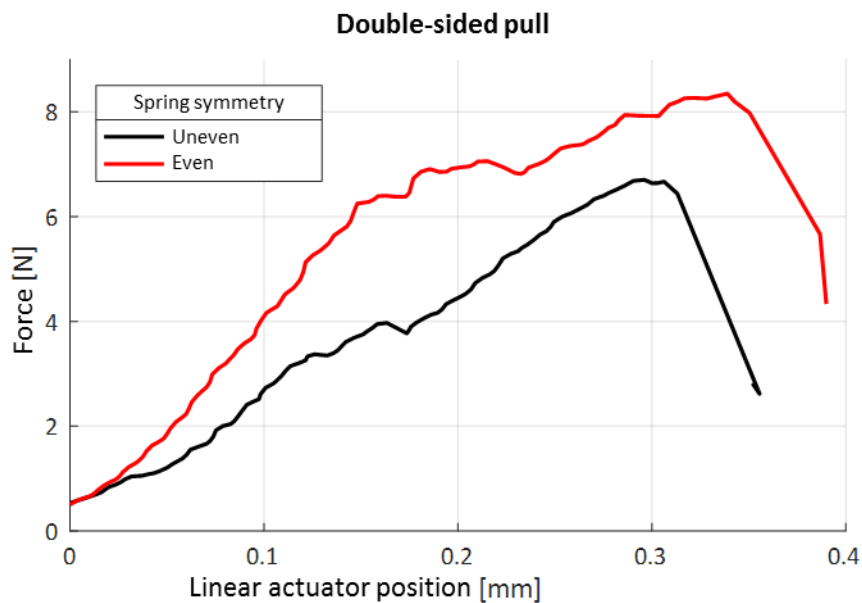
Figure 4.19: Influence of asymmetrical attachment of the steel cables in a double-sided pull experiment (C100S, $t = 0.07$ mm, $L_0 = 47.5$ mm, $\Delta L = 2$ mm).

4.4 Experimental Results

The experiments help the understanding of how the different parameters affect the maximum SMA force, the necessary SMA stroke as well as the output stroke of the bi-stable spring. The following parameters are varied in the experiments:

- Spring pretension
- Spring length
- Spring thickness
- Spring material
- SMA lever arm

The basic reference spring configuration for these experiments is a 70 µm thick spring out of 1.1274 steel with a lever arm of 1.5 mm outside of the hinge. All experiments are conducted for one-sided and double-sided pull.

4.4.1 **Variation of the Bi-stable Spring Pretension**

For the variation of the bi-stable spring pretension, a free spring length of 55 mm is selected. The pretension is gradually increased up to a value of 10 %. The increase in pretension is expected to result in increased SMA force and stroke as well as higher spring stroke. By reducing the distance between the hinges on the spring mount, seven different spring pretension values are evaluated. The resulting SMA force-displacement characteristics are displayed in Figure 4.20 for the one-sided pull (upper part) and the double-sided pull (lower part). Higher spring pretension leads to increased SMA stroke and force. The force values for the double-sided pull are more than twice as high as for the one-sided pull. At pretensions up to 4 %, the force characteristic shows a plateau around the maximum value for the one-sided pull, whereas for the double-sided pull the maximum value is measures shortly before the point of mechanical breakthrough.
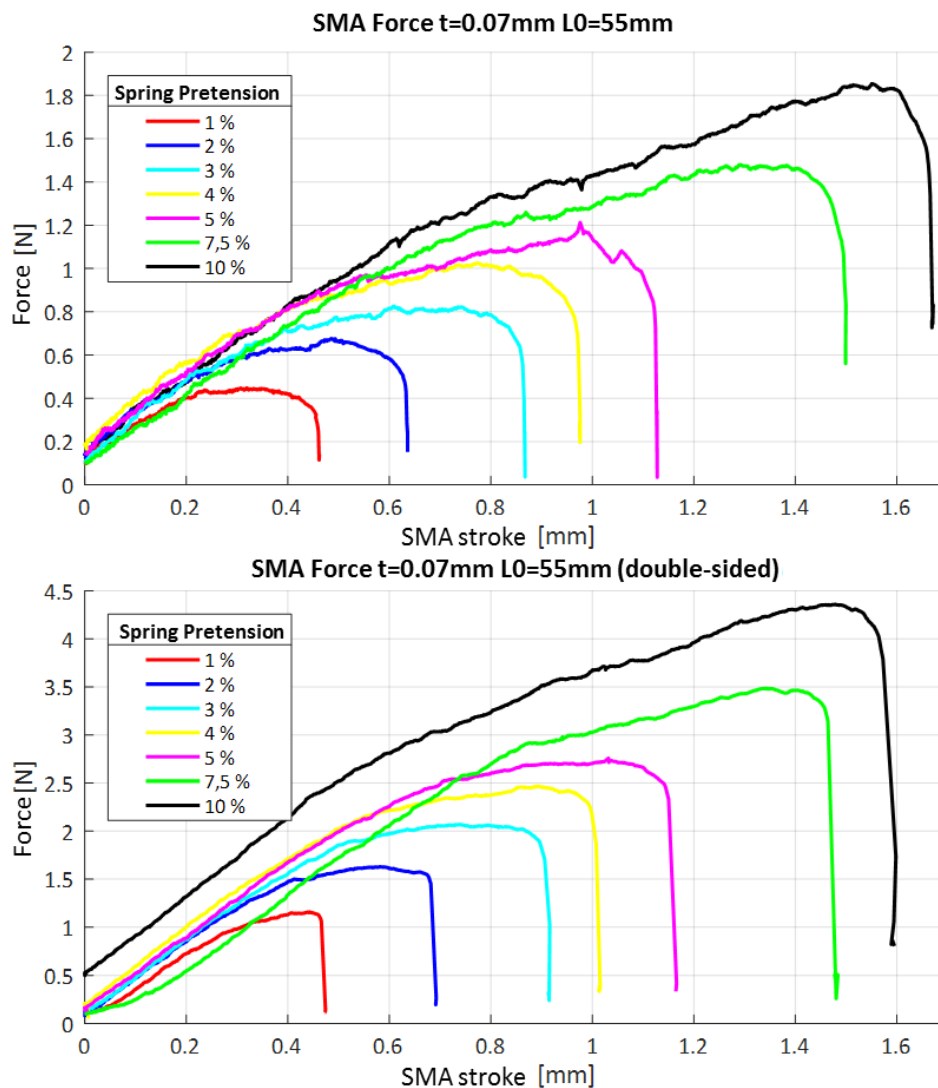
Figure 4.20: Force characteristics for varied spring pretension on a spring with 70 µm thickness and 55 mm free length. One-sided pull in the upper part and double-sided pull in the lower part.

The relation between maximum force and pretension is shown in Figure 4.21. Both characteristics show a linear trend. The gradient for the double-sided pull is higher by a factor of 2.4, which means that the in an application, bigger diameter SMA wires would be required.
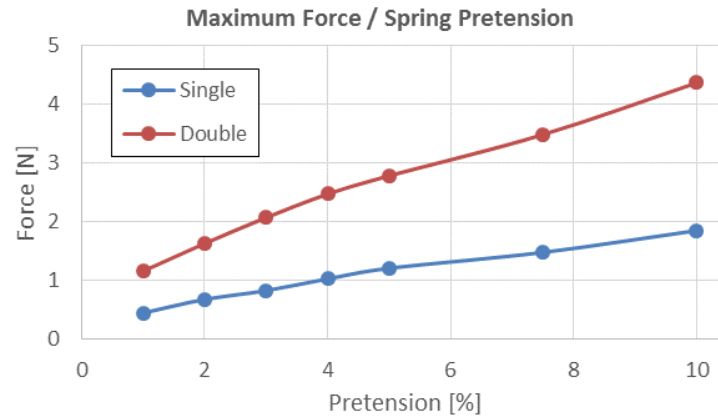
Figure 4.21: Relation between maximum SMA force and spring pretension for one-sided and double-sided pull experiments ($t = 0.07$ mm, $L_0 = 55$ mm).

As expected, the spring stroke increases as well with higher pretension (Figure 4.22). The spring stroke increases form 6.5 mm at 1 % pretension to 21 mm at 10 % pretension. The maximum stroke at 10 % pretension equals 38 % of the spring length (55 mm). The transmission ratio between SMA stroke and spring stroke is in the range of 1:12-1:14.

In contrast to the steady increase in spring stroke in the one-sided pull experiments, the double-sided pull results in a slight decrease in stroke at the start of the experiments. For these experiments, the stroke increase starts after about half of the total SMA stroke. This behavior can be explained with the different bending modes (Figure 4.23). The displacement is measures at the center of the spring. For the double-sided pull, the torque applied in both hinges leads to a bending of both spring ends which results in an upward (negative) movement of the spring's center. The situation displayed in Figure 4.23 shows the spring center reached the initial starting position again moving in positive direction.

The stroke characteristics in Figure 4.22 also suggest a faster and more abrupt mechanical breakthrough or snapping. The relation between stroke (SMA and spring) and pretension is shown in Figure 4.24. The maximum spring stroke has an identical behavior for both experiments, while the SMA stroke shows little discrepancies. Also the characteristics indicate a saturation for higher pretension values.
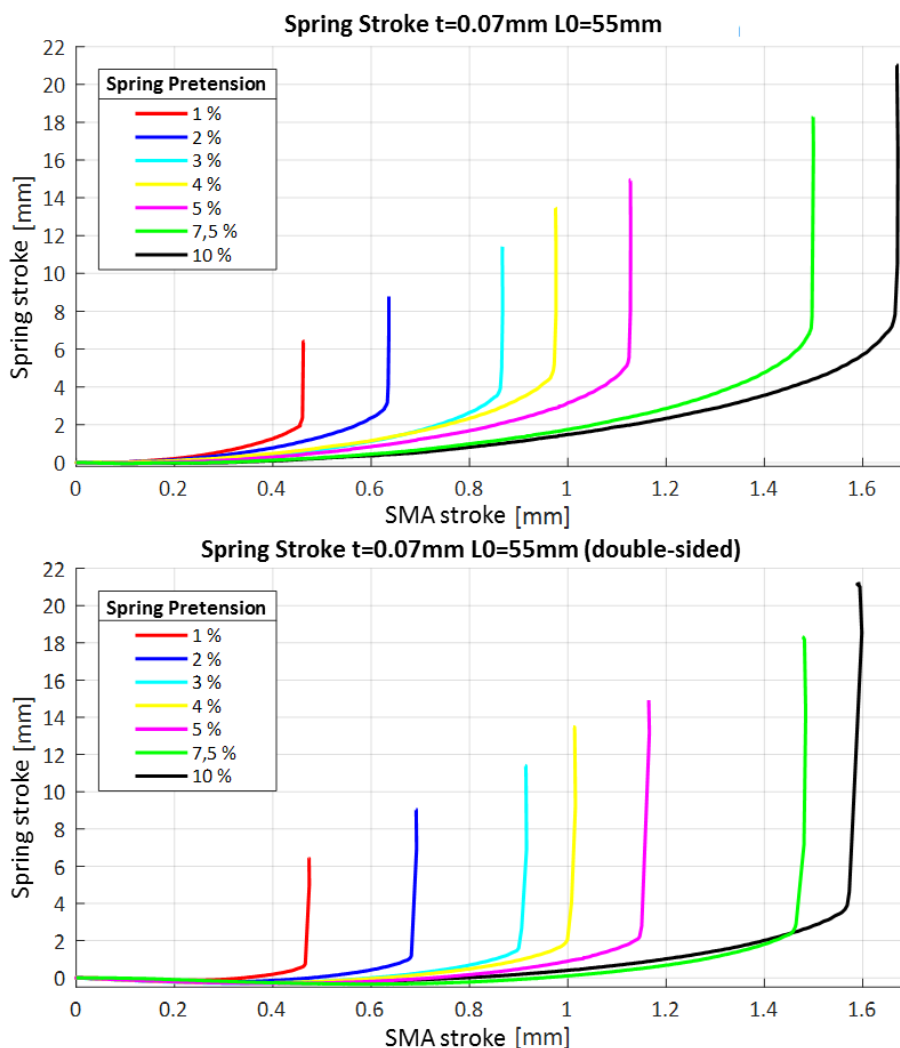
Figure 4.22: Spring stroke characteristics for varied spring pretension on a spring with 70 µm thickness and 55 mm free length. One-sided pull in the upper part and double-sided pull in the lower part.
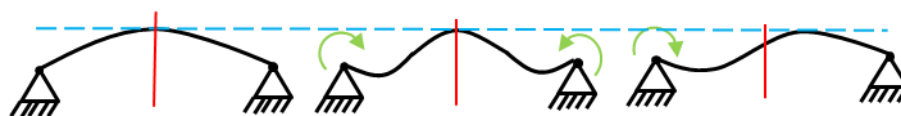
Figure 4.23: Different bending modes for one-sided (right-hand side) and double-sided (center) pull from the initial position (left-hand side).

For design of bi-stable spring actuators, a mini-tool in SolidWorks is used for modeling the bending curve of the bi-stable spring with the integrated spline function (Figure 4.25). For validation of this CAD based model, the experimental results are compared to the model predictions in Table 9. Overall, the model predictions correspond well with the experimental data. The spring strokes are very similar for all pretension values and the SMA stroke corresponds very well for higher pretension. For lower pretension values, the modeled SMA stroke is 0.2-0.3 mm higher than the measured values. That means the mini-tool is suited for first approximations in the design of bi-stable SMA actuators.
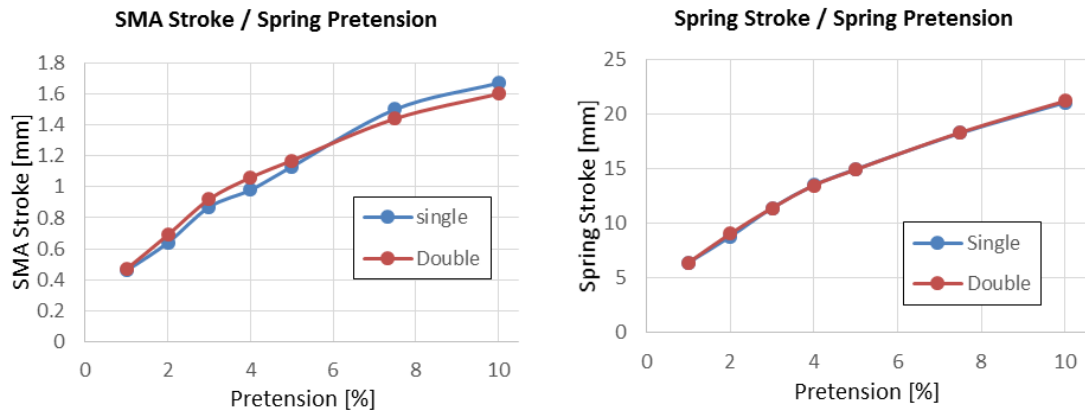
Figure 4.24: Necessary SMA stroke in relation to the bi-stable spring pretension (left-hand side) and maximum spring stroke output in relation to the bi-stable spring pretension (right-hand side) for one-sided and double-sided pull experiments.
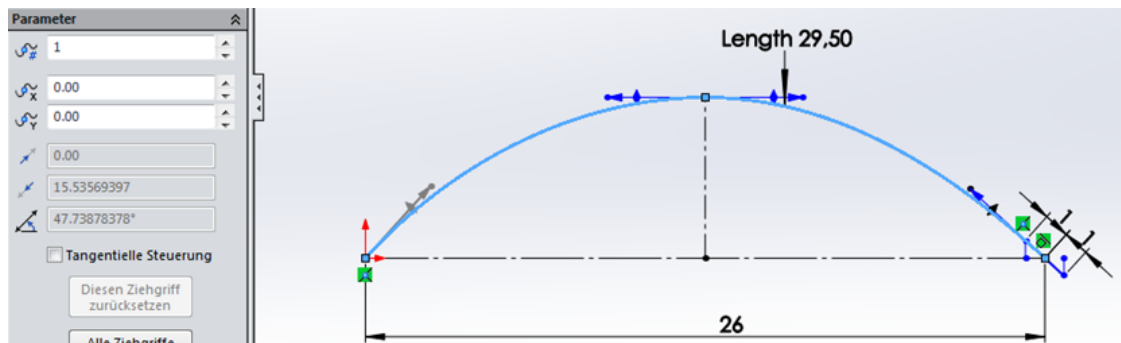
Figure 4.25: Screenshot of the SolidWorks tool for the modeling of bending curves of 2D bi-stable spring elements.

Table 9: Comparison of the modeled values and the measured values for necessary SMA stroke and spring stroke output.

Spring Pretension [%]	**Spring Stroke Model [mm]**	Spring Stroke One-Sided [mm]	Spring Stroke Double-Sided [mm]	**SMA Stroke Model [mm]**	SMA Stroke One-Sided [mm]	SMA Stroke Double-Sided [mm]
1	**6.6**	6.4	6.4	**0.78**	0.46	0.47
2	**8.6**	8.8	9.1	**0.81**	0.63	0.69
3	**11.5**	11.4	11.4	**1.18**	0.86	0.91
4	**13.5**	13.5	13.5	**1.28**	0.97	1.01
5	**15.1**	15.0	14.9	**1.36**	1.13	1.17
7.5	**18.6**	18.3	18.3	**1.52**	1.50	1.47
10	**21.3**	21.1	21.2	**1.64**	1.70	1.60

4.4.2 **Variation of the Bi-stable Spring Length**

For the variation of the spring length, the base reference spring configuration is used for all four spring length values. A constant pretension is realized through a reduction of the hinge distance of 4 % of the respective spring length. The results in Figure 4.26 show little difference in the force behavior, although the shorter springs tend towards higher maximum forces. Again, the double-sided pull results in forces more than twice as high as in the one-sided pull experiment.

The necessary SMA stroke for a mechanical breakthrough stays constant over all experiments (Figure 4.27). Only the maximum displacement of the spring center increases for longer spring lengths. This increase shows a linear behavior for the investigated range of spring lengths. An increase in spring length of 5 mm results in a stroke output increase of 1.5 mm. The fact that the SMA stroke remains constant leads to an increase in transmission ratio from 1:11.9 for the short spring to 1:13.8 for the longest spring.
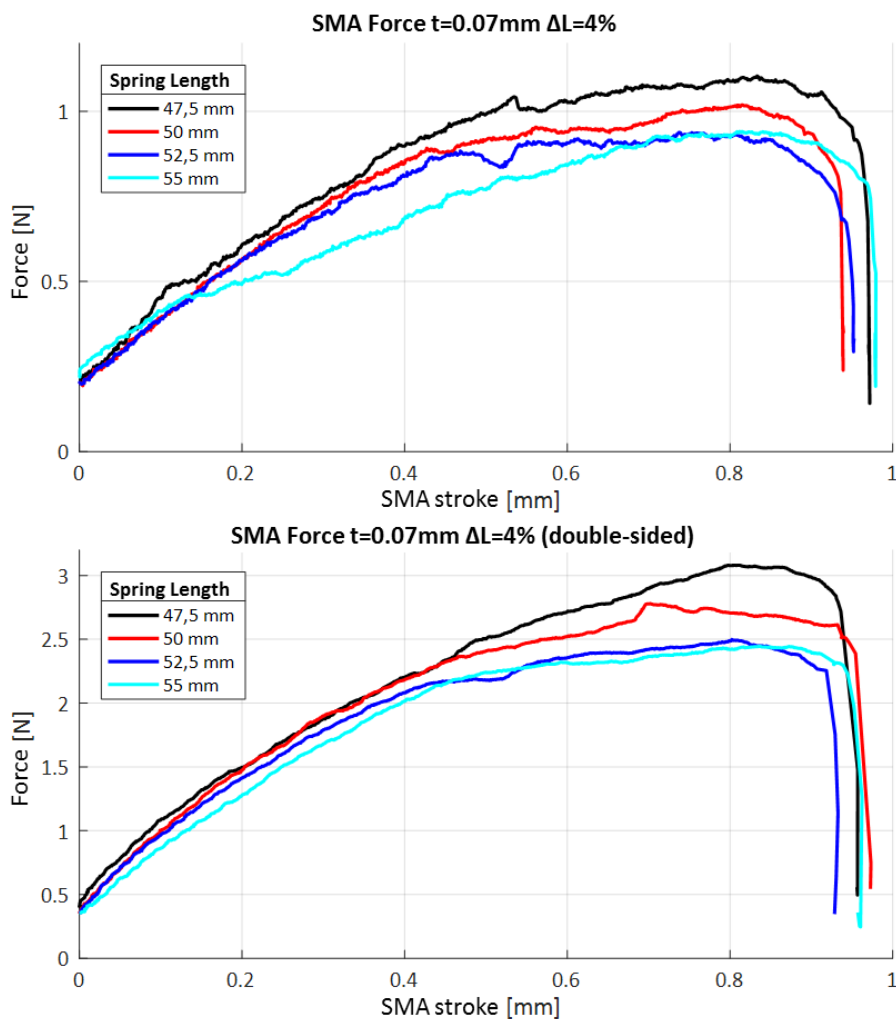
Figure 4.26: Force characteristics for varied spring lengths on a spring with 70 µm thickness and constant spring pretension. One-sided pull in the upper part and double-sided pull in the lower part.
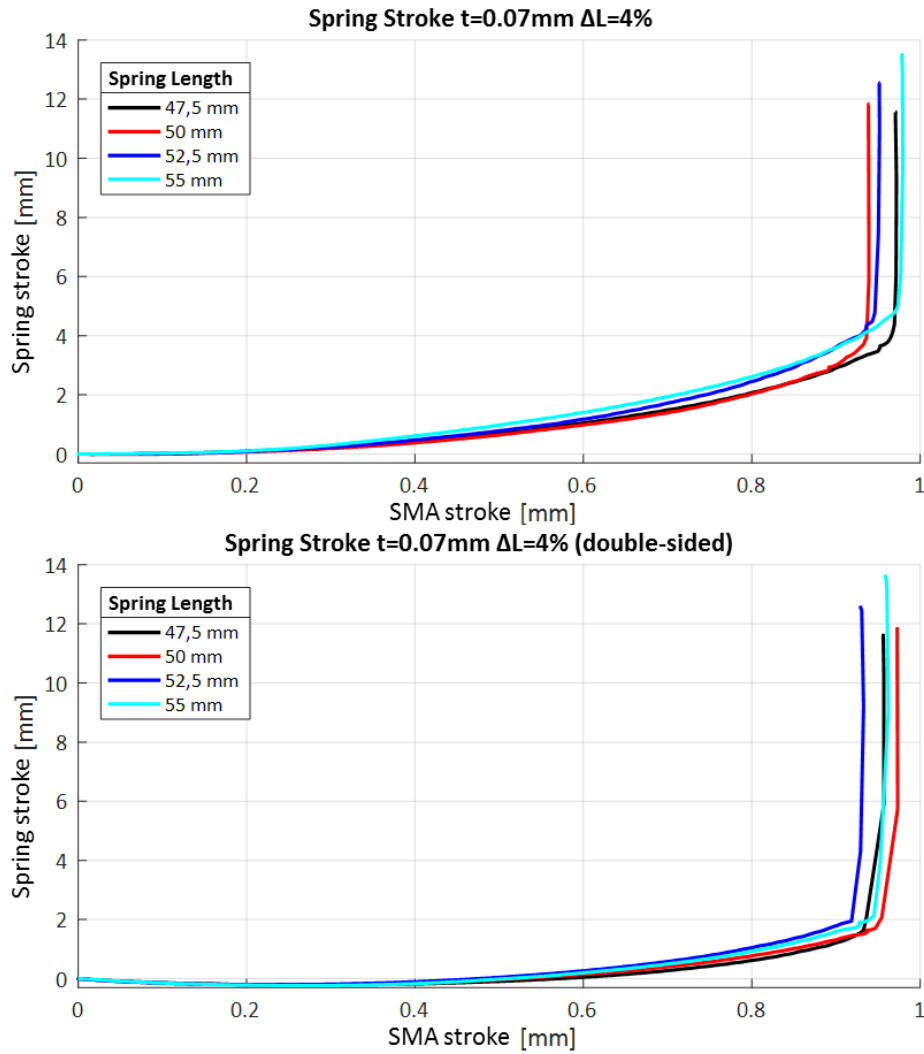
Figure 4.27: Spring stroke characteristics for varied spring lengths on a spring with 70 µm thickness and constant spring pretension. One-sided pull in the upper part and double-sided pull in the lower part.

4.4.3 **Variation of the Bi-stable Spring Thickness**

The variation of the spring thickness is expected to have a major effect on the resulting forces. The geometrical moment of inertia for the spring cross section [146] is calculated with:

$$I_z = \frac{b^3 \cdot h}{12}. \tag{4.1}$$

The thickness of the spring is described by b in (4.1), which means that it has a cubic relation to the resulting bending moment ($b = t$). The stroke output should not be affected by the spring thickness. The measurement results in Figure 4.28 show, that doubling the thickness from 50 µm to 100 µm results in forces more than five times higher for the one-sided pull and more than 7 times higher for the double-sided pull experiment.
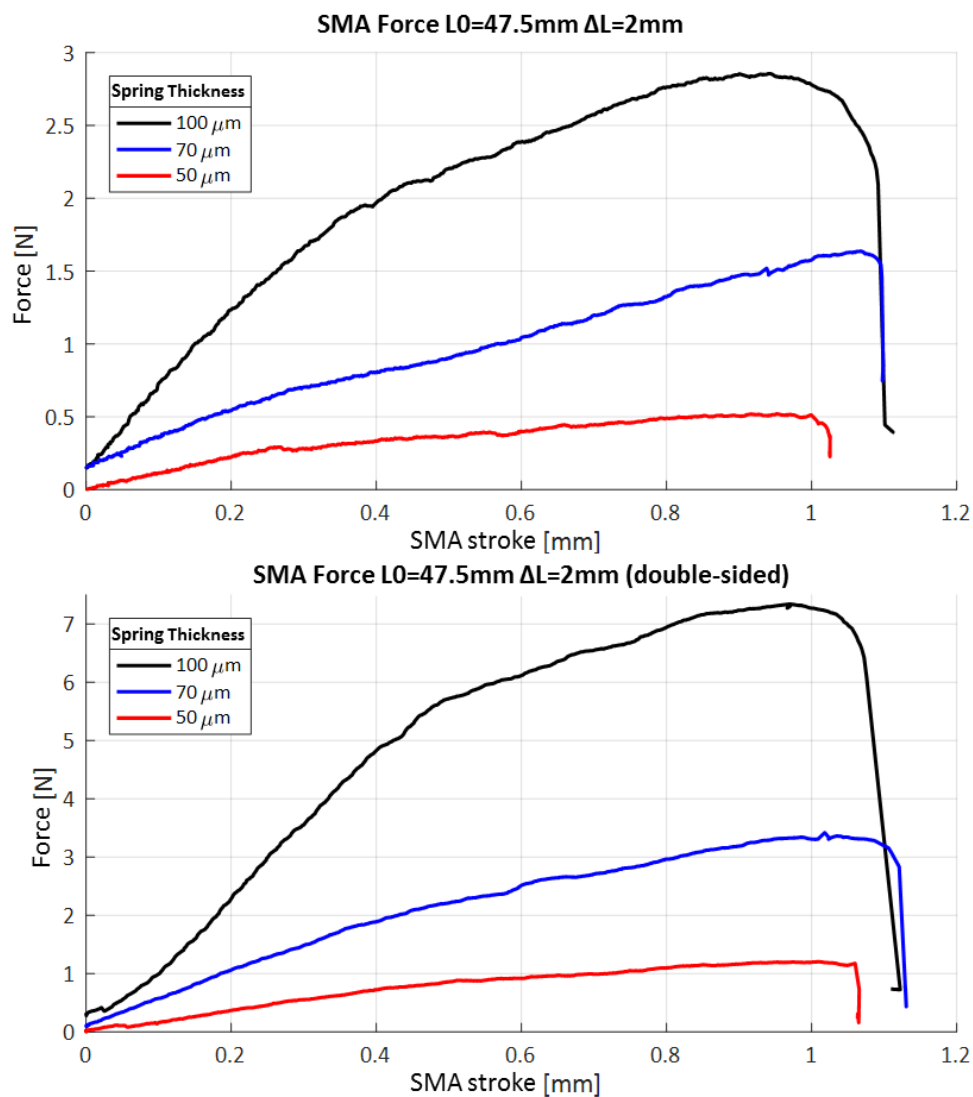
Figure 4.28: Force characteristics for varied spring thicknesses on a spring with 47.5 mm length and constant spring pretension. One-sided pull in the upper part and double-sided pull in the lower part.

As expected, the thickness of the bi-stable spring has a major influence on the necessary force to generate the snapping of the spring. The stroke output remains constant as displayed in Figure 4.29.

The mechanical stress is higher in thicker springs, especially on its edges. Stacking of several thin springs to generate higher forces could reduce the local stress in the individual springs. The rotational movement at the hinges however causes problems as displayed in Figure 4.30. The two springs have a different distance to the pivot point because of their thickness. That means, while one of the springs is in its initial U-shape, the other one is forced to bend because of the fixed distance between the hinges. Because of this effect, no experiments have been conducted with stacks in this experimental setup.
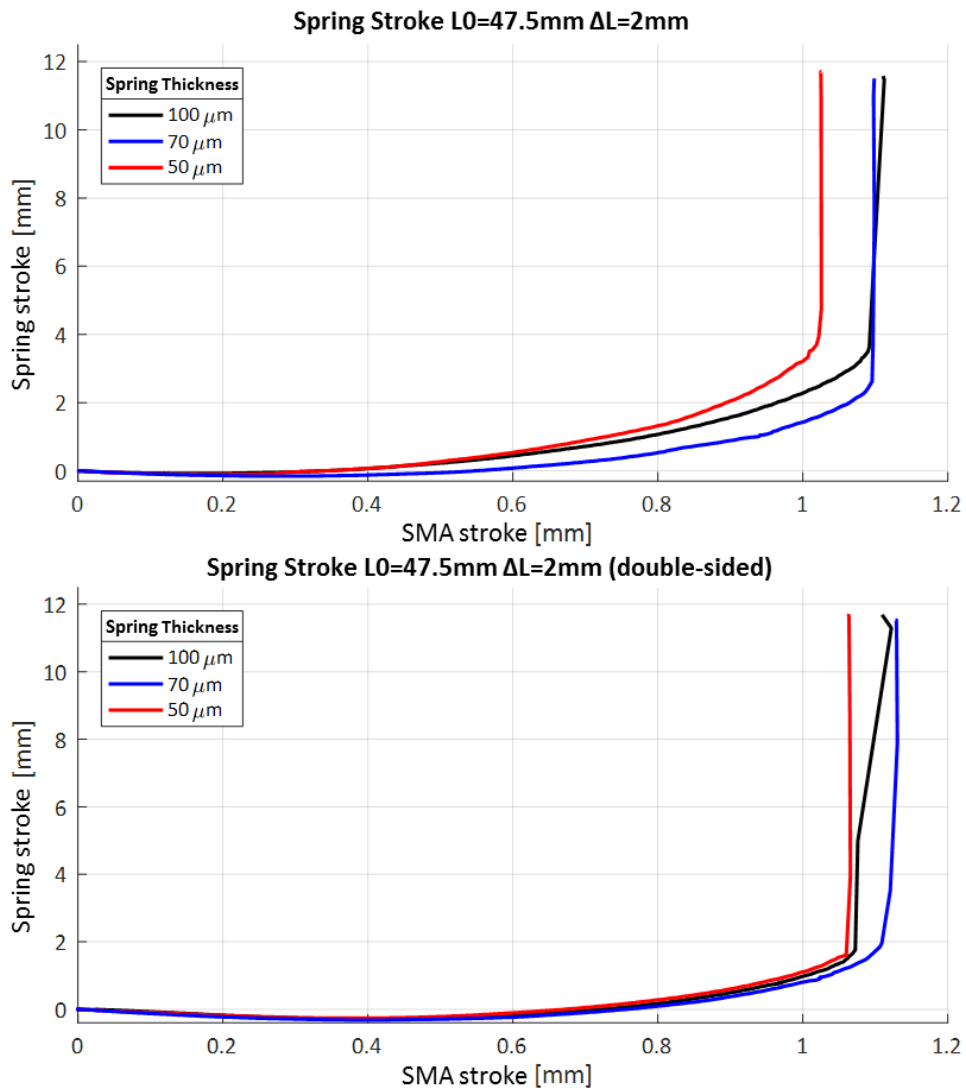
Figure 4.29: Spring stroke characteristics for varied spring thicknesses on a spring with 47.5 mm length and constant spring pretension. One-sided pull in the upper part and double-sided pull in the lower part.

Figure 4.30: Stack of two 50 µm thick bi-stable springs. An apparent gap between the two springs resulting from the different distance to the pivot point can be observed.

4.4.4 **Variation of the Bi-stable Spring Material**

The variation of the spring material is expected to have an influence on the maximum forces because of different Young's moduli and yield strengths. Again, no difference is expected in the stroke output behavior. In the first experiments, regular spring steel (1.1274) is compared with stainless steel (1.4310). The springs in these experiments have a length of 55 mm and a thickness of 70 µm.

The second set of experiments compares superelastic NiTi springs with the same stainless steel (1.4310). For material availability reasons, the spring specimens in these experiments are 50 mm long and have a thickness of 110 µm. For all experiments, pretensions of 4 % and 10 % are evaluated to investigate possible plastic deformation. The comparison between the two steel types is shown in Figure 4.31.
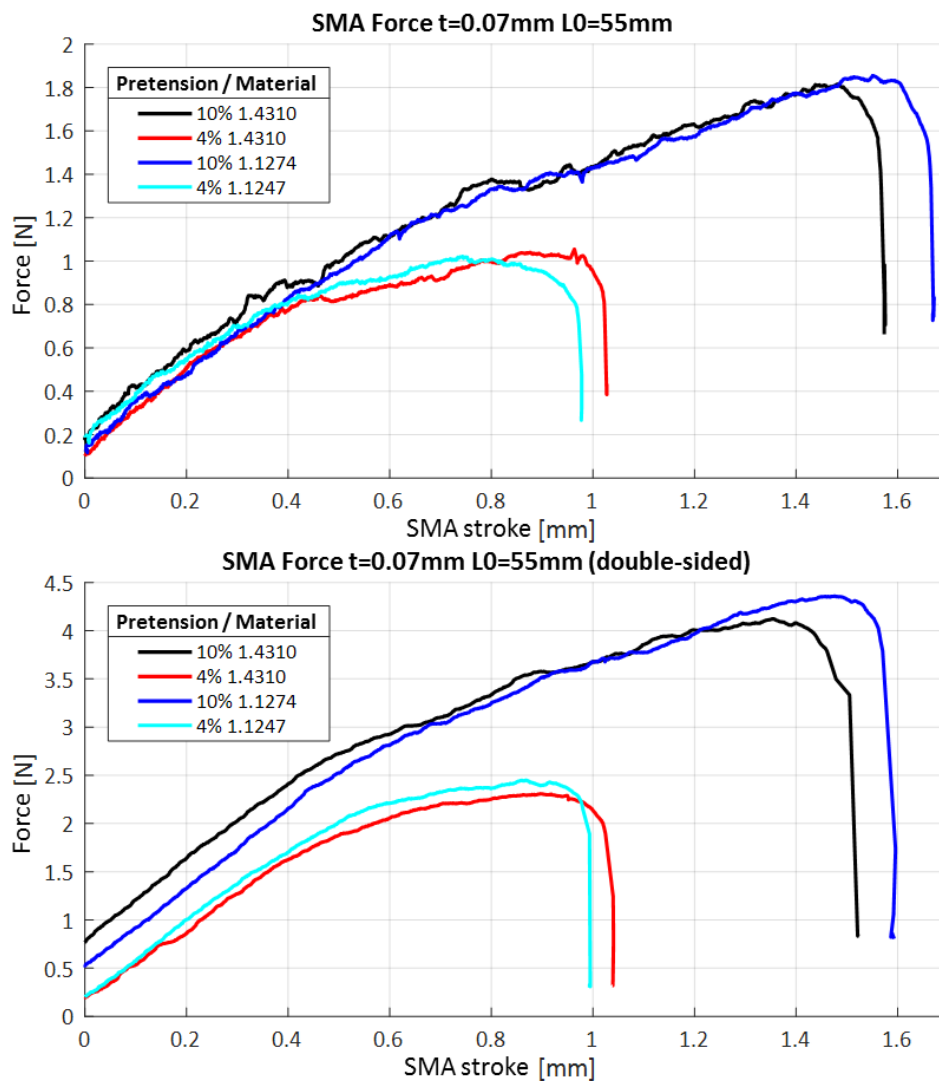
Figure 4.31: Force characteristics for two different steel types and two levels of pretension. One-sided pull in the upper part and double-sided pull in the lower part.

The small difference between the maximum forces can be explained by the slightly higher Young's modulus of 1.1247 (C100S). Both springs have not shown any plastic deformation which means that a pretension of 10 % does not lead to critical stresses. The maximum stroke of the spring is not affected by the material (Figure 4.32). The SMA stroke does not show a clear tendency, as its values are lower for C100S at 4 % pretension but higher for C100S at 10 % pretension. The discrepancy between the absolute values is in the range of 0.1 mm. This scattering of the measurement can be observed in all experiments and can be reasoned by the tolerances of the setup, in particular in the hole pattern for the steel cable attachment.
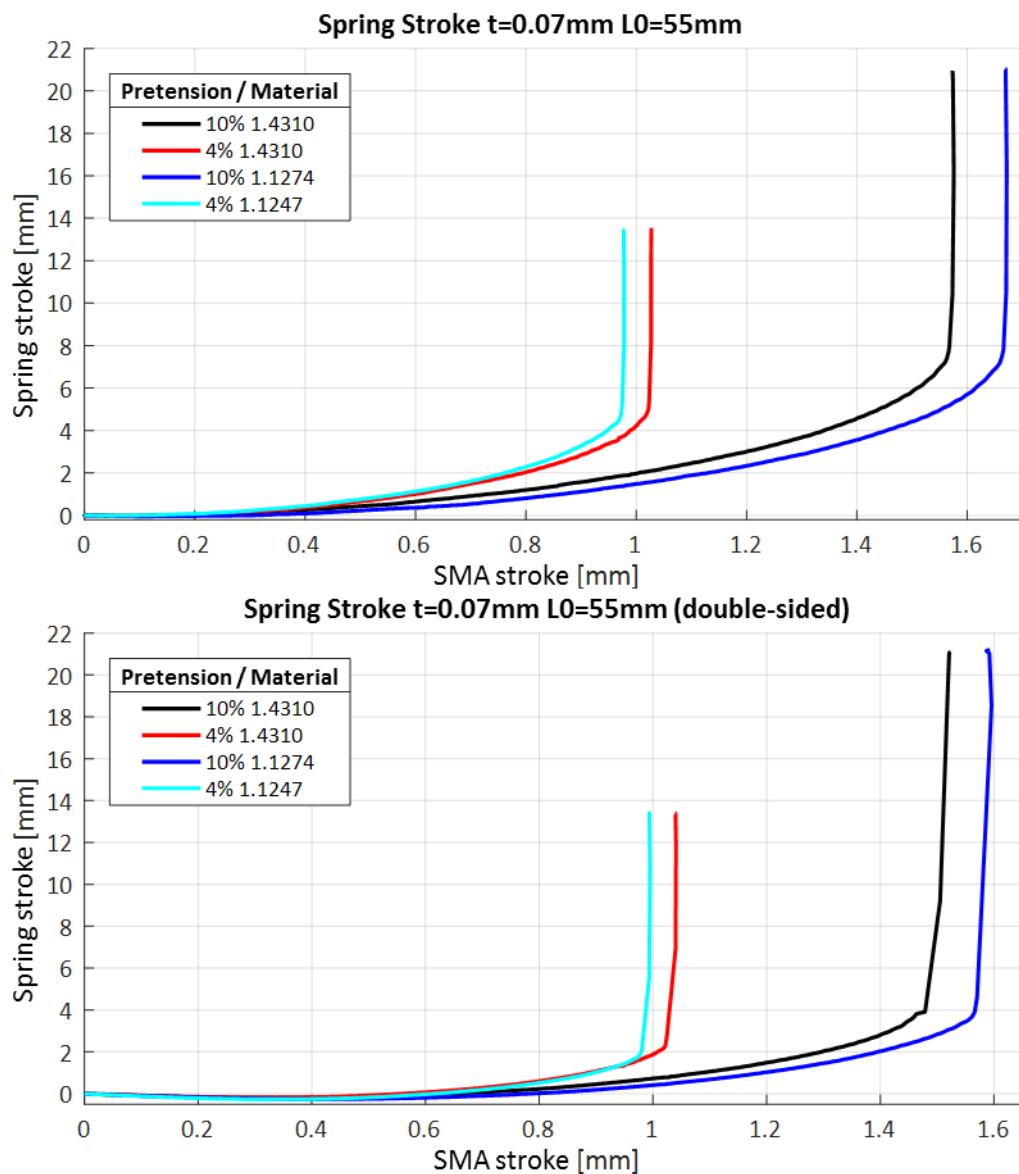
Figure 4.32: Spring stroke characteristics for two different steel types and two levels of pretension. One-sided pull in the upper part and double-sided pull in the lower part.

The low Young's modulus of the NiTi in comparison to steel leads to much lower forces (Figure 4.33). The double-sided pull experiment at 10 % pretension could not be completed for the steel spring, because the maximum linear actuator force was reached during the experiment. The measurements do not give new insights to the material behavior, because the superelastic material property becomes relevant at much higher material strains (or for much thicker springs), where the steel is plastically deformed. The stroke behavior is also unaffected by the material variation (Figure 4.34).
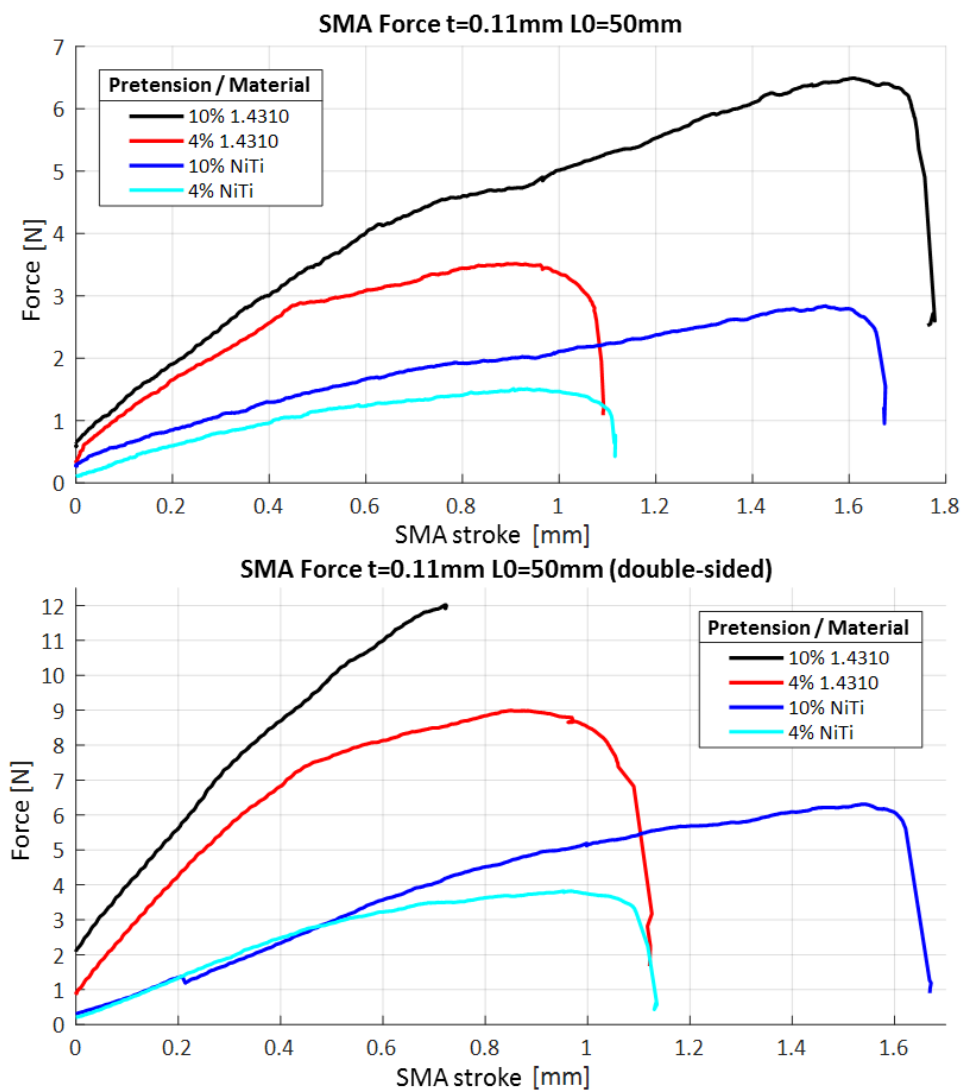
Figure 4.33: Force characteristics for steel (1.4310) and superelastic NiTi at two levels of pretension. One-sided pull in the upper part and double-sided pull in the lower part.
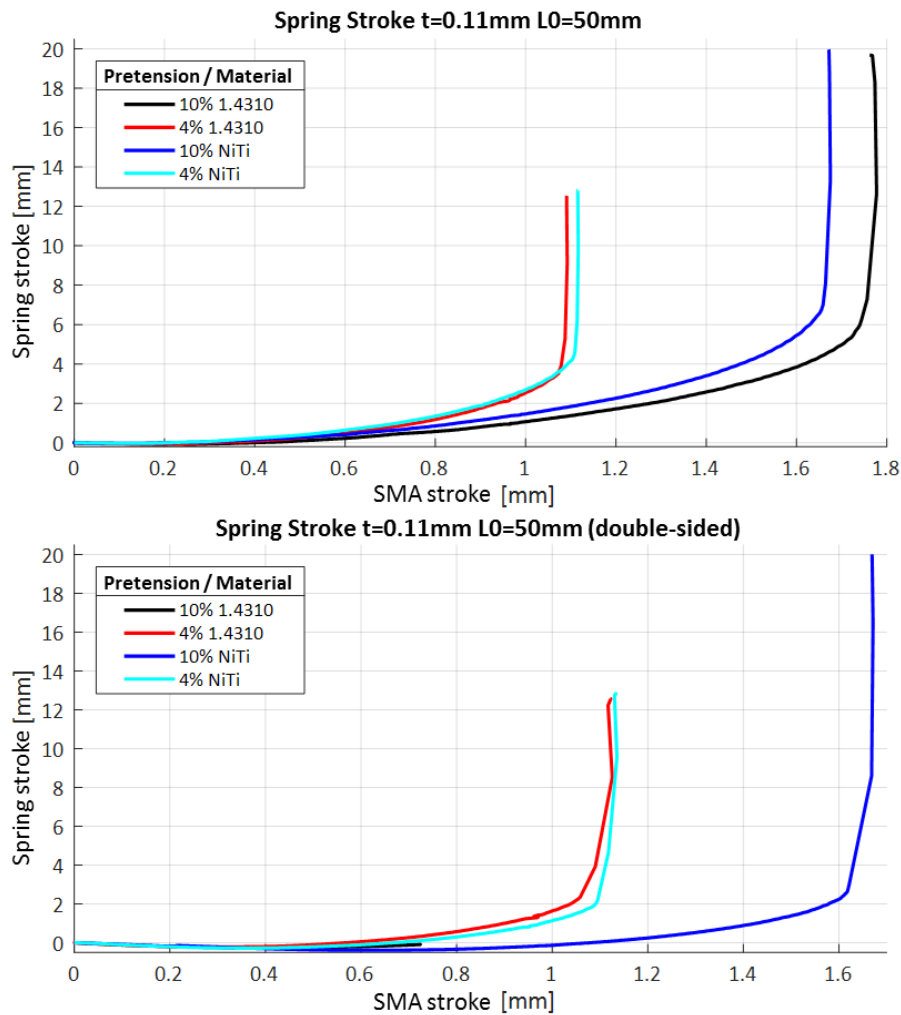
Figure 4.34: Spring stroke characteristics for steel (1.4310) and superelastic NiTi at two levels of pretension. One-sided pull in the upper part and double-sided pull in the lower part.

4.4.5 Variation of the SMA Wire Lever Arm

Three different lever arm values (0.5 mm, 1.5 mm, 2.5 mm) are evaluated for a steel spring with 50 mm free length. For each lever arm value, the steel cable is attached at the inside and at the outside of the pivot point. Theoretically, no difference in force behavior is expected by switching the attachment point. The measured force characteristics are displayed in Figure 4.35. The observed differences between inside and outside attachment of the steel cable is the result of the general tolerance of +/- 0.05 mm for the machining of the parts. The discontinuous force characteristic for the short lever arm of 0.5 mm results from slipping of the steel cable in the slightly bigger hole for attachment. This effect can be neglected for bigger lever arms. The variation of the lever arm has a major influence on the transmission ratio between necessary SMA stroke for a mechanical breakthrough and the output stroke of the bi-stable spring.
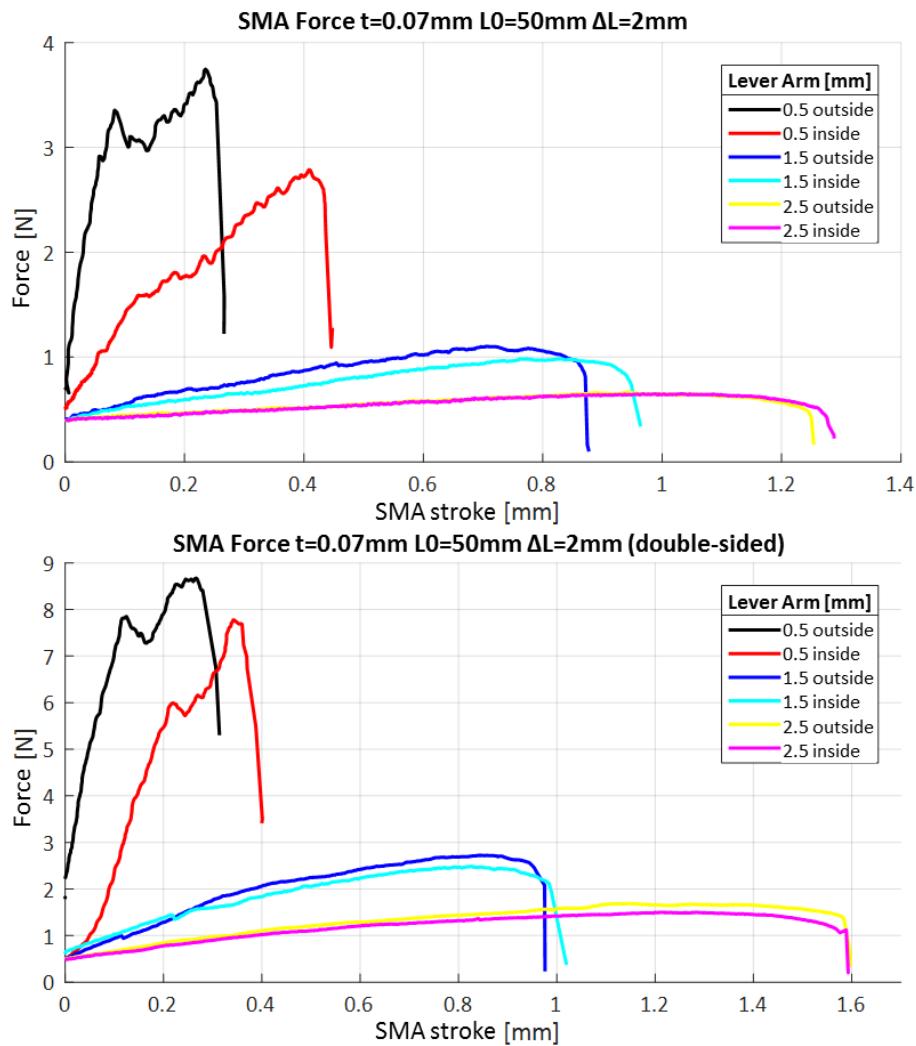
Figure 4.35: Force characteristics for a hinged bi-stable spring (1.1274) actuated with different lever arms. One-sided pull in the upper part and double-sided pull in the lower part.

The comparison of the different transmission ratios in Table 10 shows that by reducing the lever arm to 0.5 mm, a transmission ratio of 1:45.7 can be realized. This is of particular interest for SMA actuator design, because the advantage of being able to generate high forces is used to minimize the restrictions of limited actuator stroke.

Table 10: Transmission ration between SMA stroke and spring output stroke for different lever arms and SMA attachment points.

| $L_0 = 50$ mm; $\Delta L = 4$ % | Transmission Ratio | | | |
| | One-Sided | | Double-Sided | |
Lever Arm [mm]	inside	outside	inside	outside
0.5	27.2	45.7	30.1	39.0
1.5	12.6	13.6	12.2	12.4
2.5	9.2	9.6	7.6	7.6

4.4.6 Transient Response of the Bi-stable Spring

In a possible application (e.g. a valve), the transient behavior of the bi-stable spring right after the snap-through is relevant for the application's functionality. Therefore, the laser displacement sensor signal is evaluated in relation to time. Figure 4.36 shows the measurement results for the one-sided pull experiment. The transient oscillation has an amplitude under 0.01 mm, which is very close to the measurement accuracy of the experimental setup. The oscillation frequency is at approx. 10 Hz.

For the double-sided pull, no transient oscillations can be observed after the snap-through. The detected noise on the displacement signal has an amplitude of approx. 0.005 mm, which equals the range of the test setup's measurement accuracy. The bi-stable spring reaches its second stable state by snapping without noteworthy transient oscillation for both activation types (one-sided and double-sided).
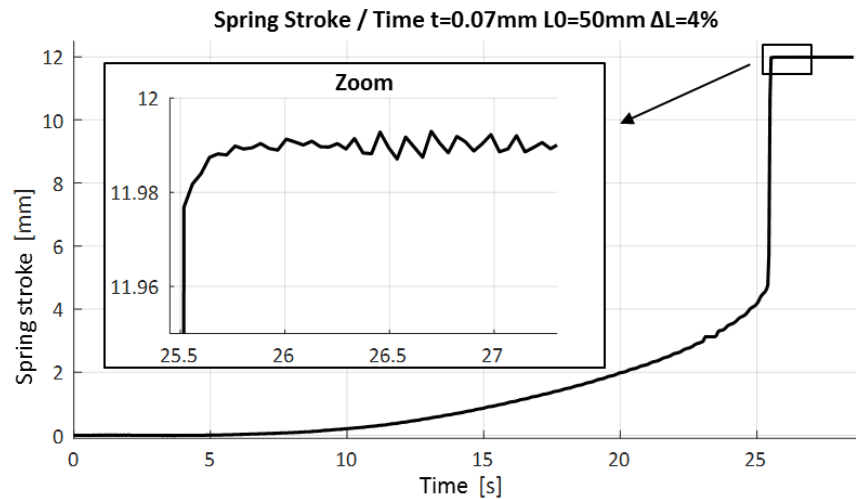
Figure 4.36: Transient response of a bi-stable spring for one-sided activation.
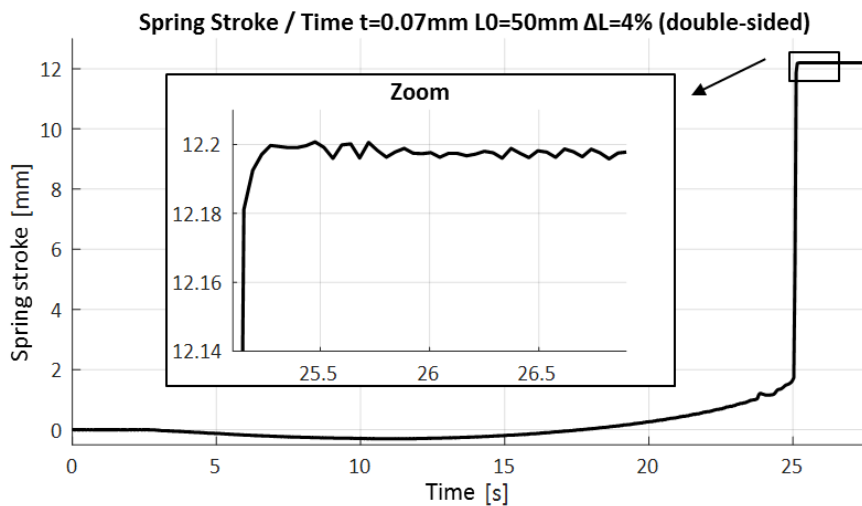
Figure 4.37: Transient response of a bi-stable spring for double-sided activation.

4.5   Summary and Future Work: Bi-stable Spring Actuators

Bi-stable SMA actuators attack the two biggest drawbacks of linear spring systems. First, the SMA wires are activated with short pulses to switch between two energy-free positions, which results in very energy-efficient overall systems. Secondly, higher actuation frequencies are reached through the active restoring forces of the antagonistic wires.

The results of the experimental study have shown relationships between the geometrical parameters of bi-stable elements and necessary SMA forces and strokes. These can be used in design of actuator systems. In addition, different applications might favor either one-sided or double-sided activation strategies, which both have been extensively compared. Double-sided activation is found to require up to 35 % higher SMA forces and the snapping motion is more abrupt than in one-sided activation. By reducing the lever arm of the SMA attachment, a transmission ratio between SMA and output stroke of 1:45 is realized. The increase in output stroke comes with an increase in SMA force, but because of the high energy density of SMA wires, forces are oftentimes easier to scale in limited construction space than stroke. The mini-tool for the prediction of the output stroke is validated by measurement results. This tool is also used for the prediction of the necessary SMA wire length, depending on the attachment point.

Future work includes further experiments with external loads and thus characterization of complete actuator systems. All measurement results should be used for the validation of a FEM design tool for bi-stable SMA actuators. With a validated tool, SMA actuators can be designed specifically for different application fields. For example, the suction cup presented in chapter 3 is upgraded with a bi-stable actuator module for energy-efficient operation. Both, the activated and deactivated state are held energy-free and only a short activation pulse is needed to grip and release a workpiece. Additionally, high-frequency pick & place tasks are now possible because of the antagonistic SMA wire configuration. Instead of a passive spring force like in linear spring systems, an active SMA force acts as the restoring mechanism.

5 Advanced SMA Actuator Concepts – High-Speed and Efficient Activation

The previous chapters demonstrated how typical SMA inherent drawbacks can be attacked by construction or design. Besides the mechanical aspects, the control of SMA wires plays a significant role regarding the actuator's performance. This chapter is mainly based on [147]–[150] and presents an SMA activation method based on higher voltage levels, which results in millisecond actuation, stroke amplification and energy savings up to 80 %.

5.1 Motivation for High-Speed SMA Activation

In most applications, an SMA wire is controlled by supplying an electrical current, which results in a Joule heating that increases the wire temperature. SMA wire manufacturers list specific activation currents for each wire diameter in their data sheets [14], [15]. These current values lead to voltages in the order of 1-10 V and may be continuously applied without overheating the wire. The use of those control values, however, commonly results into a slow activation of the SMA wire (order of seconds), which potentially limits the applicability of the technology [151]–[154]. It is remarked how the electrical resistance, and consequently the desired supplied voltage and power, depend on the geometry of the SMA actuator, i.e., wire diameter and length, as well as phase composition and temperature [28], [155]. All of those quantities change during actuation, therefore the supplied current is non-constant for a constant applied voltage. This implies a need for application-specific power electronics to ensure correct current values for SMA activation, which may severely complicate the overall system design. In addition, many researchers investigated different driving strategies such as pulse-width modulated controllers, or PI and PID controllers for position control via resistance feedback [156]–[164]

The study in this chapter presents a different activation approach for SMA wire actuators. The total electrical energy that is needed to heat up the wire to transformation temperature can be controlled not only by voltage level but also by the length of the activation pulse. Therefore, instead of using power electronics to transform the given supply voltage to a desired level, the duration of the activation pulse is adjusted. That way, the activation of the SMA wire takes place at a high electrical power for a short time interval. First studies on SMA pulse activation were conducted by Vollach, Shilo and coworkers [165]–[168]. In their investigation, kilovolt pulses of the duration of microseconds were used to activate

SMA material, while acquiring at the same time frequency response, displacement and SMA force. However, the presented studies were conducted mainly with a material science perspective, since the focus of the work was the kinetic of the Nickel-Titanium phase transformation. In addition, the adopted voltage on the order of kilovolts is difficult to be reproduced in real-life applications, e.g., industrial ones. It is pointed out how the use of such a control strategy is still relatively unexplored for application-oriented SMA devices which operate in industrial environments, and thus subject to constraints in terms of maximum voltage levels.

The goal of this study is the exploration of potential application scenarios for pulse-controlled SMA, compatibly with voltage levels commonly used in industrial environments. Typical supply voltages used in real-life applications range from 12 V to 48 V in the automotive sector, 24 V for industrial bus systems, and up to 110-125 V in aerospace industry. These values are significantly higher than the ones commonly used to drive SMA wires (on the order of 1-10 V), and therefore they lead to higher currents than recommended by datasheets. At the same time, these values are significantly lower than the ones investigated in previous studies on pulse driving (on the order of kV). It is shown that it is possible to use these given supply voltages to generate pulse activation in the millisecond range, achieving fast and energy-efficient SMA actuation with a compact and lightweight power electronics solutions.

In conventional quasi-static operation, one typically focuses on stroke as a direct consequence of the low-voltage activation. On the other hand, the high-voltage activation of SMA wires, and the related phase transformation in the material, result in an instantaneous generation of force, which leads to a highly dynamic stroke as a consequence of accelerations and velocities. In addition to simplified power electronics and faster actuation time, a further advantage of pulse actuation is energy-efficiency. In current state-of-the-art actuators, the SMA wire activation takes place under non-adiabatic conditions, i.e., a large amount of the heating energy is lost due to heat exchange with the environment during the activation process. With high electrical power and a fast heating pulse, it is possible to reach the transformation temperature and start actuation before heat is lost to the environment, thus leading to an adiabatic activation. All the mentioned effects are examined with systematic measurements in an experimental setup and presented in the following sections.

5.2 Experimental Setup

The block diagram of the experimental setup is shown in Figure 5.1 (upper part). A power supply is used to heat the SMA wire with an electric pulse. A laser displacement sensor, model Keyence LK-G87, measures the SMA wire stroke. The time derivatives of the displacement signal, i.e., velocity and acceleration, are calculated and plotted in post-processing. SMA force is recorded by a load cell of the type Futek LSB200. The voltage on the SMA wire is measured via 4-wires sensing, while electrical current measurement is realized via a current clamp. Additionally, the whole experiment is recorded with an optical high-speed camera system Olympus i-SPEED TR for a better interpretation of the measurement results. Signal processing and data acquisition during the experiment are realized via a NI cRIO system. The mechanical structure of the setup, including the positioning of the key components, is shown in Figure 5.1 (lower part, [148]). The SMA wire is guided vertically and clamped at top and bottom. The specifically designed clamps combine mechanical and electrical connection, by connecting the SMA wire directly to a small PCB part. The upper clamp is attached to the load cell, which is connected to the aluminum frame structure. The bottom clamp is directly connected to the air-bearing shaft. The total weight of the clamp including shaft is 22.5 g. A compression spring can be placed between the bottom clamp and a micro-adjustment stage, allowing to vary the SMA wire pretension. In applications, the use of springs as a bias mechanism for the SMA wire is a common design solution [95]. Additionally, the spring is used to adjust bias forces to bigger SMA wire diameters. The air bearing guides the vertical motion with minimal friction. The laser displacement sensor detects the motion of the air-bearing shaft. The SMA wire length in its austenitic state in this setup is 225 mm.

5.2.1 Test Procedure

The SMA wire used in these experiments is a SAES Getters SmartFlex actuator wire with a transition temperature $A_s = 90\ °C$ [15]. The SMA wire length is measured in its austenitic state, in order to guarantee reproducibility. At low temperature (martensitic) state, the SMA wire shows a two-way effect. This means that, after cooling down, the SMA wire shows a non-defined elongation, even without external loads [4], [18]. This elongation is not uniquely defined, and may vary from sample to sample. To ensure that the SMA wire length is always measured in the same crystallographic state, a separate measuring setup is used. In this setup, the SMA wire is heated in a nearly load-free configuration to reach complete phase transformation to austenite. The desired length is measured and marked in this high temperature state.
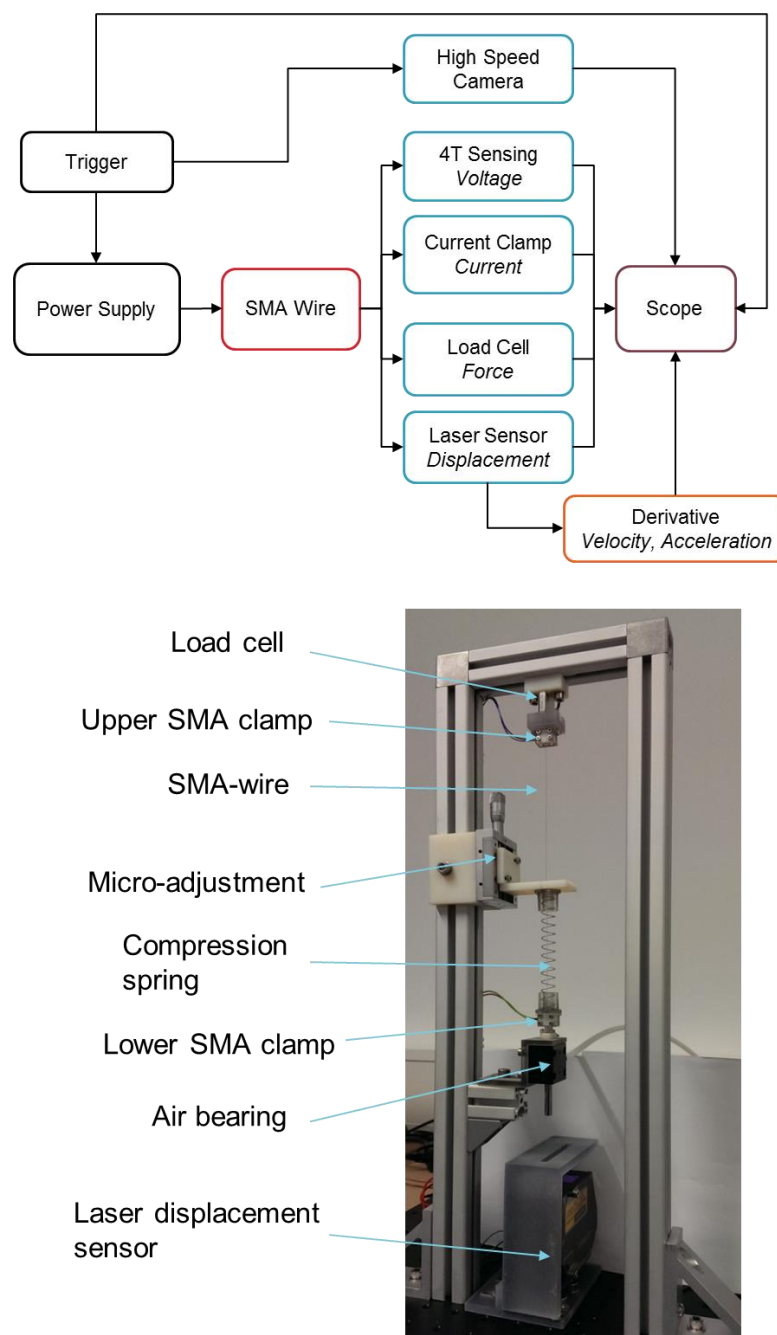
Figure 5.1: Block diagram (upper part) and mechanical structure (lower part, [148]) of the experimental setup.

The wire is then cut at the markers and clamped in the experimental setup. The micro-adjustment stage, in combination with the compression spring and the load cell, allows the generation of a desired pre-stress and pre-strain in the SMA wire. The experiment is then started via LabView.

SMA wires show a training effect after early activation cycles. This effect is visible in a change of its remnant strain after cooling down and returning to its initial state. A new SMA wire in the test setup needs a few training cycles (usually 10-20 cycles) until the remnant strain stays constant. Therefore, the force signals and the displacement signals are

compared to the initial values after each experiment. The measurements are started, once the force and displacement stays at constant values after few activations. During the measurements, mechanical stress in the SMA wire can reach critical levels, which may lead to plastic deformations and eventually damage the wire. This aspect can be monitored by the force and displacement values after each experiment. In case critical stress is overcame, the SMA wire has to be exchanged.

5.3 Experimental Results

Typical activation of a conventional SMA wire is displayed in Figure 5.2. An SMA wire with a diameter of 76 µm is activated according to the manufacturer's data sheet suggestion, i.e., a supply voltage of 8 V. The resulting electrical current is of approximately 150 mA for 1 s. The initial force is set to 0.28 N, which results to a mechanical stress of 60 MPa in the SMA wire. The bias spring has an elastic constant of 0.056 N/mm. The graph shows the trigger signal (brown), electrical current (black, [A]), force (purple, [N]), displacement (green, [mm]), velocity (yellow, $[10^{-1}$ m/s]) and acceleration (cyan, $[m/s^2]$) signals. After 1 s, a maximum displacement of 8.33 mm is reached, which corresponds to a stroke of 3.7 %. The maximum mechanical stress in the SMA wire reaches 165 MPa. This measurement will serve as a reference for the energy analysis in the following experiments at higher voltages, which will use identical parameters for initial force and spring rate.
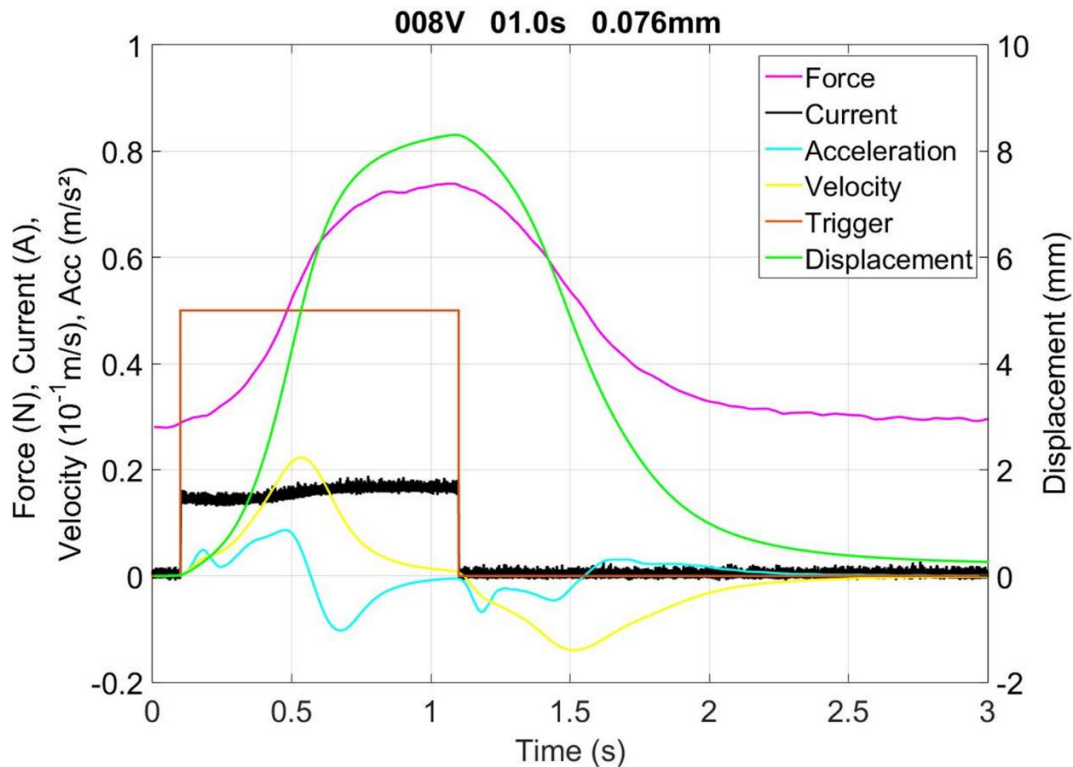
Figure 5.2: Conventional SMA activation as reference measurement showing a synchronized evolution of force and displacement in a quasi-static condition.

5.3.1 **Conventional SMA Activation vs. High-Speed SMA Activation**

In all of the experiments performed with quasi-static actuation mode, the displacement is measured as a direct output. The force and displacement signals are always in phase, implying that inertial effects are negligible. From a mechanical point of view, the system is described by the equilibrium of forces, including the SMA force F_{SMA}, the spring force F_{spr} and the weight force F_{weight}:

$$F_{SMA} = F_{spr} + F_{weight}. \tag{5.1}$$

Note that the inertia force is neglected in (5.1), due to the quasi-static condition. After the supply voltage is turned off, the SMA force and the displacement return to their initial starting values. The displacement signal shows the effects of the thermal cooling of the SMA wire.

The energy balance for this conventional activation is described by:

$$\int_{t_0}^{t_1} U \cdot i \cdot dt = m_{SMA} \cdot c \cdot (T_{trans} - T_{env}) + h \cdot m_{SMA} - \int_{t_0}^{t_1} \alpha \cdot A_{SMA} \cdot (T_{SMA}(t) - T_{env}) \cdot dt. \tag{5.2}$$

The electrical energy input is calculated by integrating the electrical power ($P=U \cdot i$, voltage U, current i) in the time interval $[t_0, t_1]$, where t_0 is the initial time and t_1 is the time at which the transformation temperature T_{trans} is reached and the phase transformation is completed. The total electric energy equals the sum of three contributions, reported on the right-hand side of (5.2). The first term corresponds to the energy required to heat the SMA wire from room temperature T_{env} to transformation temperature, given by the product of $(T_{trans} - T_{env})$, specific heat capacity c and SMA wire mass m_{SMA}. The second term $h \cdot m_{SMA}$ describes the latent heat of the phase transformation. Finally, the third term accounts for the heat loss due to thermal exchange between the SMA wire and the environment, where α is the convective cooling coefficient, and A_{SMA} is the surface area of the SMA wire. Note that both i and T_{SMA} are assumed to be non-constant during the time interval $[t_0, t_1]$.

In contrast to the conventional activation, Figure 5.3 shows experimental results of SMA activation at higher voltages. In these experiments, the same SMA wire with a diameter of 76 µm is activated at 24 V (Figure 5.3, upper part), 48 V (Figure 5.3, center part) and 125 V (Figure 5.3, lower part). The first qualitative difference observed is the oscillation of the spring-mass-system before it returns to its initial starting values. The force and displacement signals are not synchronous anymore. In this dynamic system, the

displacement is the result of the acceleration caused by the SMA force. Mechanically, the system dynamics have to be included by adding the inertia force F_i to (5.1):

$$F_{SMA} = F_{spr} + F_{weight} + F_i. \tag{5.3}$$

For a discussion of the quantitative changes, expanded views of the three measurements in Figure 5.3 are shown in Figure 5.4. The current signal in the measurement at 24 V (Figure 5.4, upper part) is similar to the conventional current signal (shown in Figure 5.2). First, the current decreases due to the rising temperature and thus rising electrical resistance in the SMA wire. Once the SMA wire starts contracting, the global geometric changes lead to a decrease of the electrical resistance and the electrical current starts to increase. The measurements at 48 V (Figure 5.4, center part) and 125 V (Figure 5.4, lower part) do not show this effect in the current signals, because there is only minimal contraction when the electrical current is turned off. The displacement signals reach higher maximum values in comparison to the conventional activation, but the force signals are always at 0 N when maximum displacement is reached. At these points during activation, the SMA wire is slack so that the load cell is unable to detect any force. This means that maximum displacement is not reached through conventional phase transformation, but due to the extreme acceleration of the bottom mass. This effect will be referred to as "ballistic" activation. For these three measurements, velocities and accelerations are up to two orders of magnitudes higher with respect to the conventional actuation. The force signals at 48 V and 125 V show an instantaneous response to the current signal, and reach their maximum values with the first peak. The behavior of the force at 24 V is slightly different, as the maximum force is reached with the second peak. The displacement at the second force peak is almost 5 mm, which is much higher in comparison to the two measurements at higher voltages. This displacement is an indicator for the actual SMA wire contraction, i.e., the measurement at 24 V shows the transition from quasi-static to highly dynamic actuation. In this particular case, dynamic effects are barely visible, but do not dominate the response.

The input energy for all three measurements in Figure 5.3 is about 0.4 J, which is much lower than the input energy of 1.2 J for the conventional activation. In conventional activation, energy is lost to the environment during actuation, which is described by the last term on the right-hand side in (5.2). Very fast actuation times lead to very small time intervals [t_0, t_1] and the heat exchange term becomes negligible.
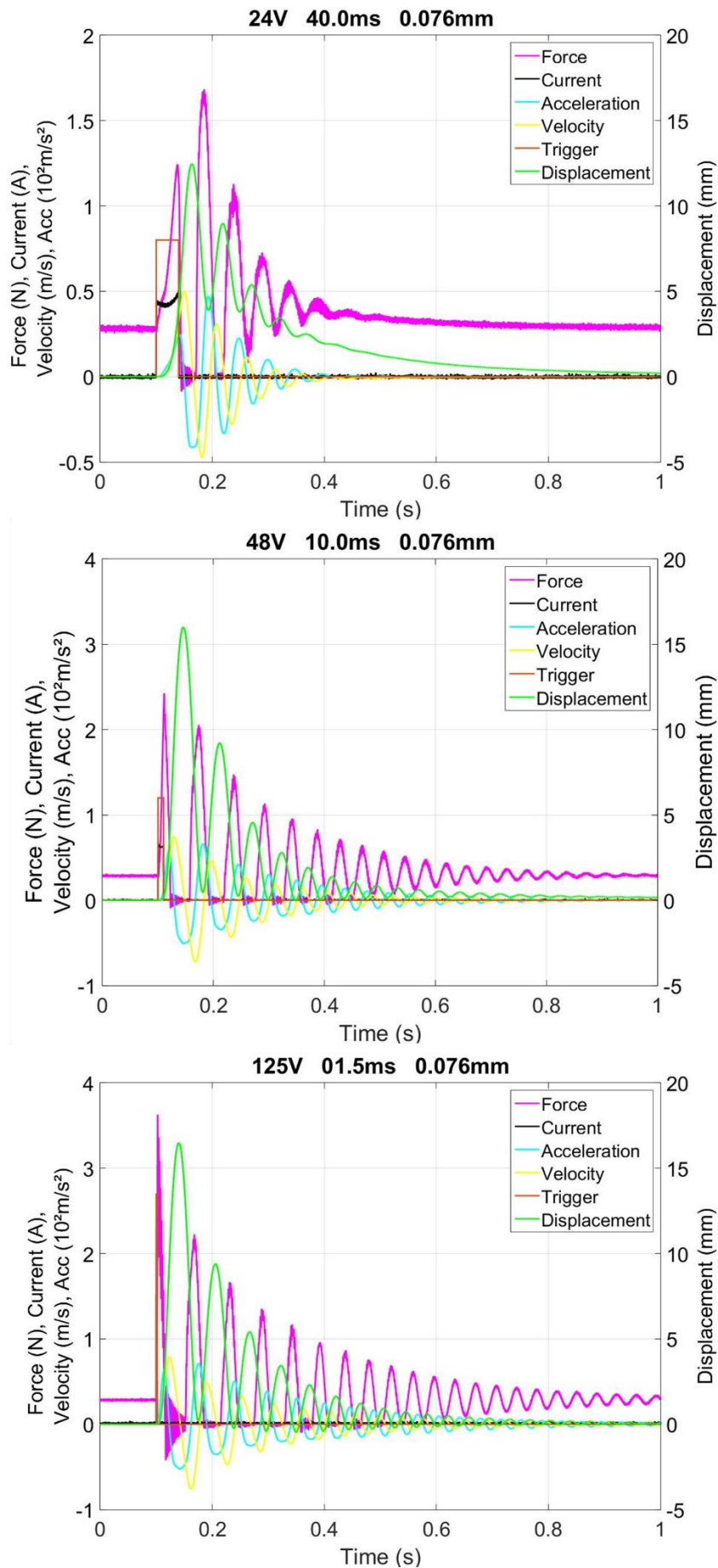
Figure 5.3: High-speed SMA activation at 24 V (upper part), 48 V (center part) and 125 V (lower part).
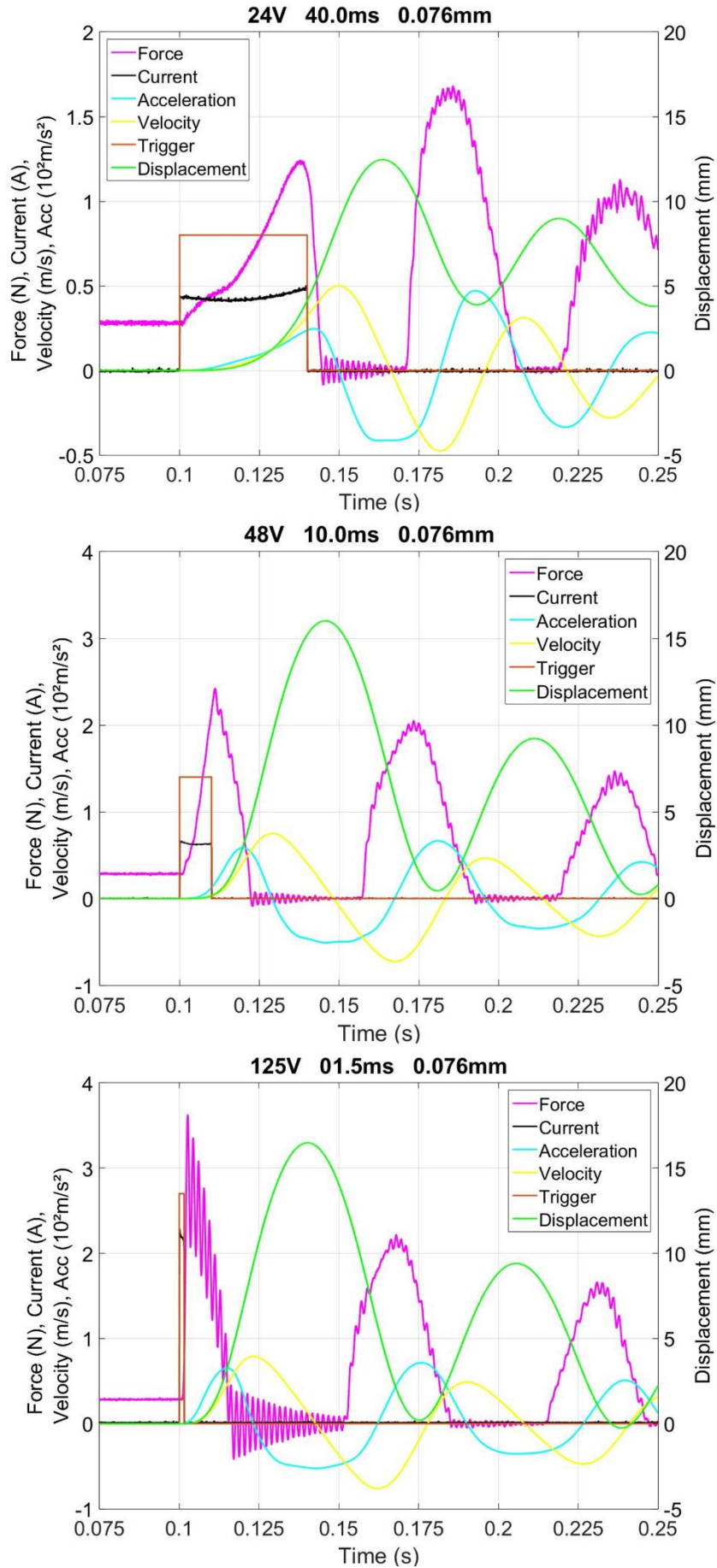
Figure 5.4: Zoomed-in measurements of SMA high-speed activations at 24 V (upper part), 48 V (center part) and 125 V (lower part).

The energy balance (5.2) for this adiabatic activation of SMA wires is reduced to:

$$U \cdot i \cdot (t_1 - t_0) = m_{SMA} \cdot c \cdot (T_{trans} - T_{env}) + h \cdot m_{SMA}. \qquad (5.4)$$

A detailed discussion of the energy-efficiency follows in section 5.3.3, which will show that all the following experiments with supply voltages of 48 V or higher can be considered to be occurring under adiabatic conditions.

Figure 5.5 shows a measurement with synchronized high-speed camera recordings to visualize the ballistic effect. The rapid heating pulse and the resulting phase transformation in the SMA wire accelerate the attached mass to a velocity that causes the SMA wire to become slack. The moving mass can result in displacement values that cannot be reached by conventional phase transformation. In this experiment, a 76 µm SMA wire is activated by a 2 ms pulse at 125 V. The maximum displacement of 21 mm implies a stroke of 9.3 %. The force in the SMA wire is present immediately and reaches its maximum of 4 N when the current is turned off at 2 ms. This force is equivalent to a mechanical stress of 880 MPa. After that, the force decreases as the SMA wire starts contracting and the mass is accelerated. The acceleration results in high velocities of the moving mass and the SMA wire becomes slack, as shown in the optical camera screenshots. At these points, the force signal is at 0 N. The excited spring-mass system continues then to oscillate until it reaches its initial state. The high frequency oscillation in the force signal is due to the natural frequency of the load cell. Maximum displacement is reached 38 ms after the electrical current is turned off. Interestingly, the acceleration signal also reaches its maximum with a delay of about 15 ms after activation, and after the maximum force peak. That means that the SMA wire is accelerated for a certain time interval even though there is no external energy input. This effect can be explained by an increase of the austenite transformation temperature under increasing mechanical stress. In fact, transformation temperature typically increases with mechanical stress by a factor of 0.11-0.14 K/MPa [3]. In the presented measurement (Figure 5.5) the mechanical stress reaches 880 MPa immediately after activation. The austenite start temperature of 90 °C is defined at a mechanical stress of 200 MPa [15]. Thus, at 4 N the austenite start temperature increases up to 185 °C. The SMA wire heats up to high temperatures before the force starts to decrease. As the force decreases, the transformation temperature also drops again, which leads to more energy in the hot wire being used for the phase transformation, even though there is no external energy input. After the force signal reaches 0 N, the acceleration starts decreasing.

During the experiment, the measured force is not in a linear relationship with the acceleration of the moving mass according to $F = m \cdot a$. The load cell measures the resulting forces at the top clamp of the SMA wire, while the bottom clamp represents the accelerated mass. In addition to the initial force resulting from the mass of the bottom clamp, the pre-loaded spring and the phase transformation, the load cell also records so-called force vibrations as soon as the system is in motion [166]. The last screenshot in the sequence of high-speed recordings (Figure 5.5) is taken at 0.1545 s and indicates a slack wire. However, the load cell records a force of about 1.5 N at this time, which implies the presence of an additional force. Vollach and Shilo describe these force vibrations as a genuine mechanical response of the SMA wire due to waves that propagate along the SMA wire.
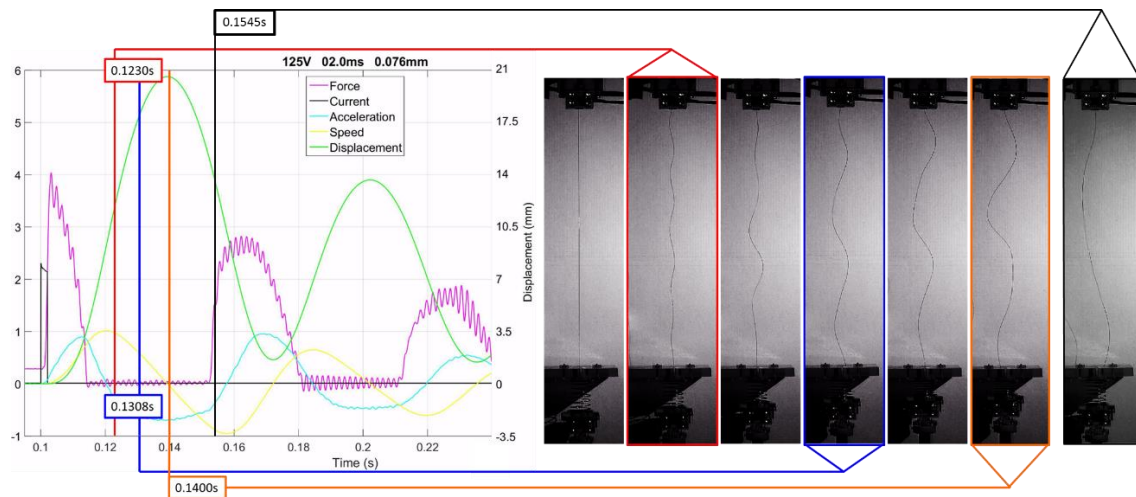
Figure 5.5: Synchronized high-speed recording of a "ballistic" activation of an SMA wire.

5.3.2 **Mechanical Analysis**

In the experimental analysis, SMA wire diameters of 50 µm, 76 µm and 100 µm are evaluated at three different supply voltages and working against two different loads. The goal is to study the effects of these parameters on some performance indices, which are relevant for actuator applications. The maximum force, the maximum displacement and the time delay to reach the maximum displacement are extracted from the measurements at 24 V, 48 V and 125 V supply voltage and graphically presented to demonstrate experimental trends. At each supply voltage, five different activation pulse lengths (pulse widths) are applied, which results in a stepwise increasing energy input. The stiffness of the compression spring working against the SMA wire equals 0.056 N/mm. Each measurement is performed with initial loads of 0.28 N (weight plus preloaded spring) and

0.67 N (same weight, increased spring preload). For a clear presentation of the measured data, the experimental results of the 76 µm wire at 48 V working against the lower load of 0.28 N is used as a reference. The variations of the initial load, the SMA wire diameter and the supply voltage are then displayed in separate graphs, always in comparison to this reference measurement.

In Figure 5.6, the experimental results of the reference measurement with the 76 µm wire are displayed. At the supply voltage of 48 V, activation pulses of 2 ms, 4 ms, 6 ms, 8 ms and 10 ms are used. With increasing activation pulse time, the generated SMA force increases (Figure 5.6, upper part), because the total energy input is higher and more SMA material is transformed from martensite to austenite. Because of the higher forces, the weight is accelerated more. This leads to higher total displacements of the moving mass (Figure 5.6, center part). Note that the maximum displacement obtained in most of these measurements does not correspond to the actual SMA wire contraction, but results from the high acceleration of the mass. The ballistic effect displayed in Figure 5.5 occurs every time, when the force signal drops to 0 N. The time to reach the maximum stroke also increases, because the total displacement is much higher (Figure 5.6, lower part) but the average speed of the moving mass is much higher for longer activation pulses.

The effect of different initial loads is displayed in Figure 5.7. At 48 V supply voltage, the 76 µm wire's preload is increased from 0.28 N to 0.67 N by increasing the spring compression. The higher preload in the SMA wires leads to slightly higher maximum forces, but the difference becomes negligible (Figure 5.7, upper part). In case of activation with a 10 ms pulse, the difference in maximum force is only 0.15 N. The high force peak right after activation results from the phase transformation. The SMA wire wants to contract immediately, but is unable to because of the load's inertia. A higher initial load results in a higher transformation temperature, that means more energy is used to heat up the wire and less energy is used for the phase transformation. Less phase transformation means that less force is added to the initial load in the first peak of the force signal. The higher initial load leads to lower maximum strokes (Figure 5.7, center part). Because of the higher initial spring load but constant mass, the negative acceleration is higher, which leads to less total displacement and shorter times to reach the maximum stroke (Figure 5.7, lower part).

48 V   0.076 mm   0.28N
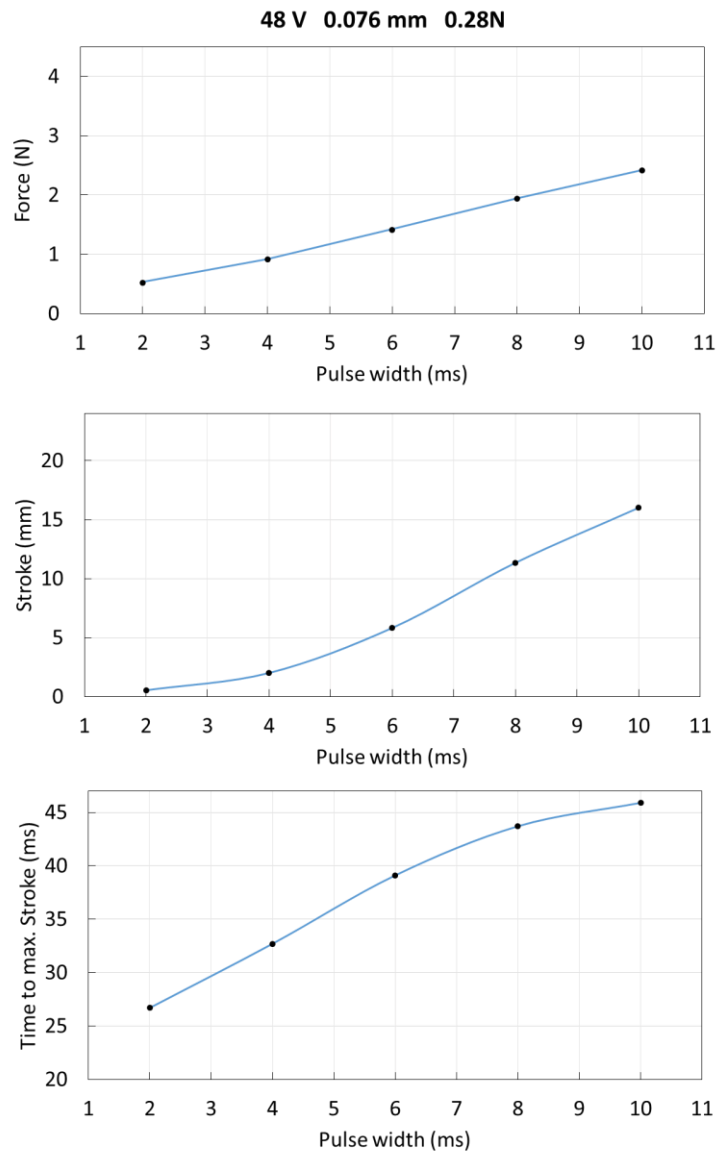
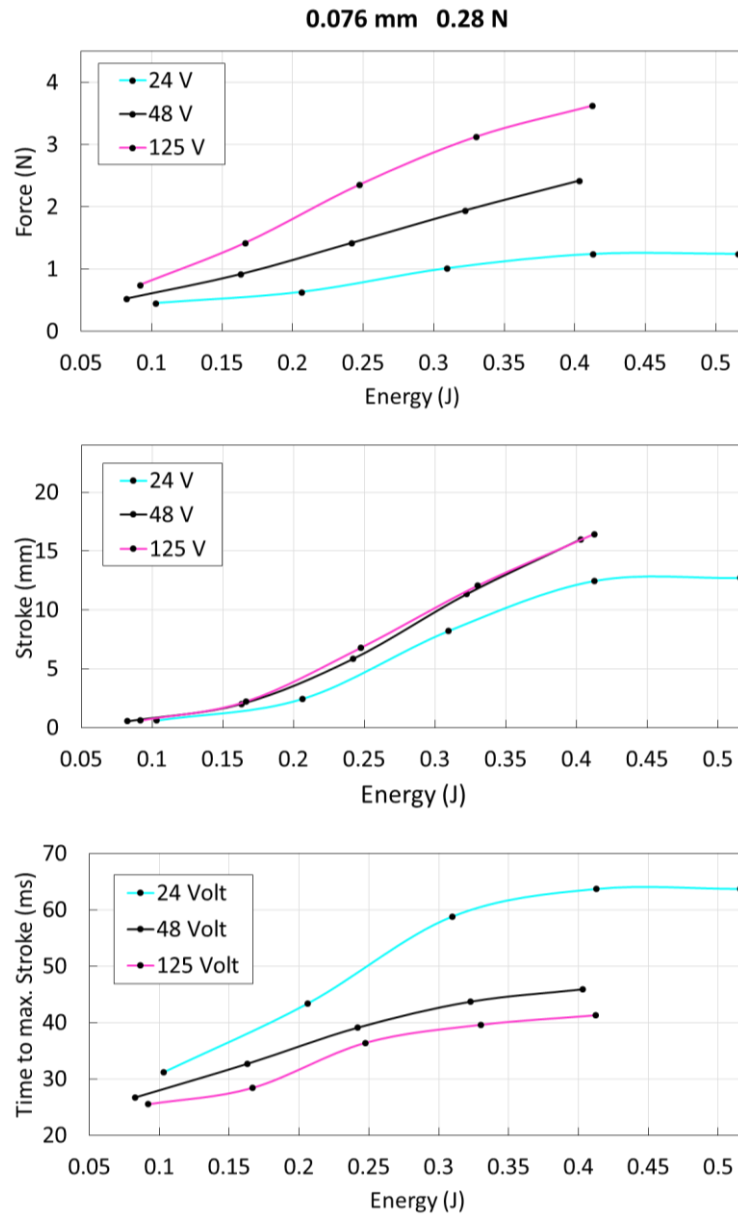**Figure 5.6:** Measurement of the 76 µm SMA wire at 48 V, recording maximum force (upper part), maximum stroke (center part) and time delay to reach maximum stroke (lower part) for five different activation pulse lengths. The initial load is 0.28 N.

The next experimental results show the effect of the SMA wire diameter (Figure 5.8). A bigger SMA wire diameter results in a lower electrical resistance, which leads to a higher power during activation at a constant voltage. In addition, the total energy input at defined activation pulse lengths is higher for bigger diameters. This fact results in more energy being used for phase transformation and thus higher SMA forces generated (Figure 5.8, upper part). For small energy inputs at short pulses (2 ms) the difference in force is not as large because the major portion of the energy is used to heat up the wire. The heating of the different wire diameters at constant voltage is very similar for these short pulses because the electrical current density is the same (and no energy is lost to the environment).
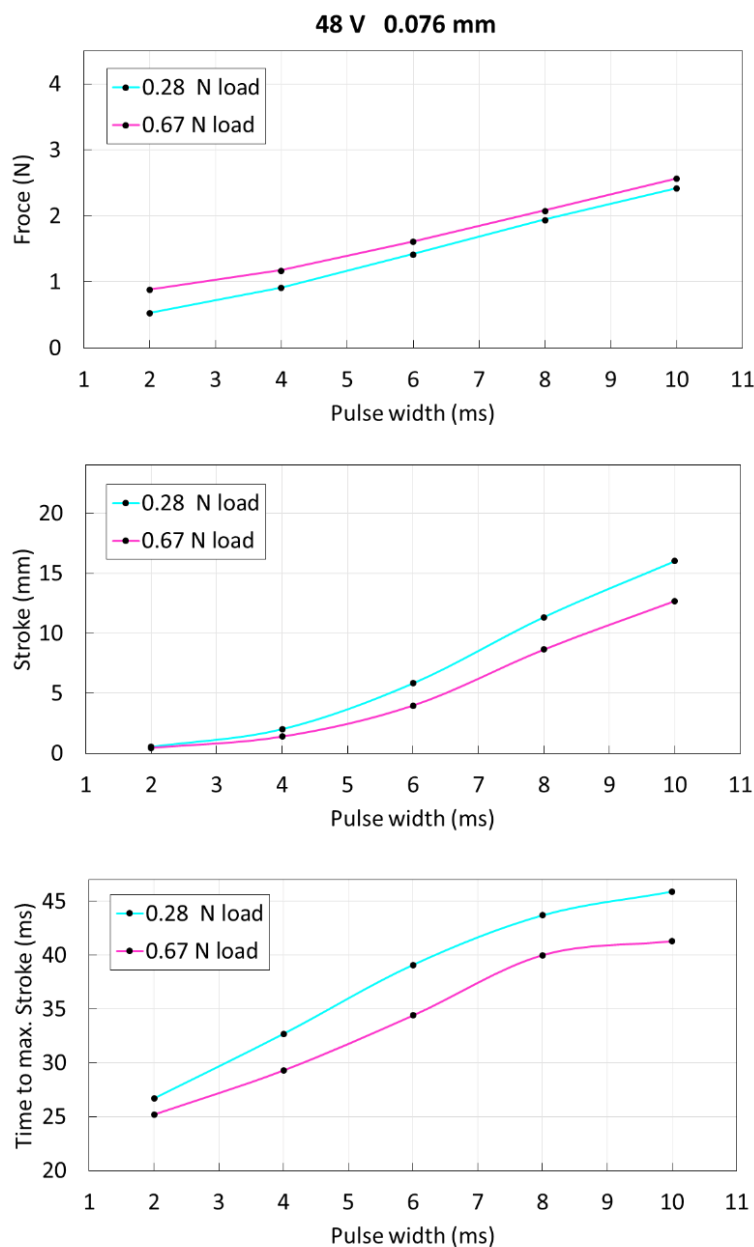
Figure 5.7: Comparison of maximum force (upper part), maximum stroke (center part) and time delay to reach maximum stroke (lower part) for two different loads (0.28 N, 0.67 N). The experiments are run at 48 V supply voltage using a 76 µm SMA wire.

The higher forces in the bigger wire diameters lead to higher strokes (Figure 5.8, center part), because of the higher energy input and stronger acceleration of the weight. The stronger acceleration also leads to higher speeds of the mass and thus shorter times to reach the maximum stroke (Figure 5.8, lower part). When activated with a 2 ms pulse, all three SMA wire reach the same maximum displacement, but the 100 µm wire is 10 ms faster than the 50 µm wire. When activated with a 10 ms pulse, all three wires reach their maximum displacement after about 45 ms, but the 100 µm wire shows a stroke of 23.9 mm whereas the 50 µm wire only reaches 9.2 mm.

Additionally, a comparison of the time delays to reach the reference displacement of 8.33 mm is presented in Figure 5.9. This is of particular interest for possible application scenarios. For this comparison, the relevant experiments at 48 V for all three SMA wire diameters are selected. The reference stroke of 8.33 mm is reached by all three wires with 10 ms pulses and by the two bigger diameters at 8 ms pulses. The 100 µm SMA wire reaches the reference stroke in less than 23 ms.

The last parameter study considers three different supply voltages (Figure 5.10). At different voltage levels, the activation pulse lengths have to be adjusted so the energy input stays similar. Therefore, this study investigates maximum force (Figure 5.10, upper part), maximum stroke (Figure 5.10, center part) and time to reach the maximum stroke (Figure 5.10, lower part) in relation to the input energy. Again, the 76 µm wire is used in these experiments with an initial load of 0.28 N. Higher voltages result in higher forces for the same input energy. Higher voltage equals higher electrical power. As previously explained, the force increases as long the load's inertia prevents the SMA wire from contracting. The faster the total energy is injected into the SMA wire, the more phase transformation takes place before the weight starts moving. The maximum stroke is almost identical at 48 V and 125 V. As shown in Figure 5.4 and Figure 5.5, the maximum displacement is reached by the "ballistic" acceleration of the mass. The highest point can be related to a potential energy. If no energy is lost during the experiment, the same input energy results in the same output. At 24 V, the SMA wire is not able to generate the same stroke, which means energy is lost during activation. The activation pulses at 24 V are much longer, which results in cooling of the wire during the activation. The generated stroke of about 12.5 mm for an energy input of 0.4-0.5 J is still the result of the ballistic activation, but the maximum stroke does not increase further. The activation pulse at 0.4 J is 40 ms long. This time interval is long enough for the system to reach a thermodynamic equilibrium, so that even longer activation pulses do not result in higher forces and higher output strokes. Again, the high acceleration of the bigger wire diameter leads to faster activation times. As before, also the time delays to reach the reference stroke are compared for the different supply voltage levels (Figure 5.11). For an energy input of 0.4 J, the stroke of 8.33 mm is reached at all three voltages. At 125 V the reference displacement is reached in under 22 ms. Even at the moderate voltage of 24 V, Figure 5.10 shows only a small decrease in energy-efficiency and performance for the activation compared to the higher voltages. The following section takes a closer look at the energy balance during high-speed SMA activation.
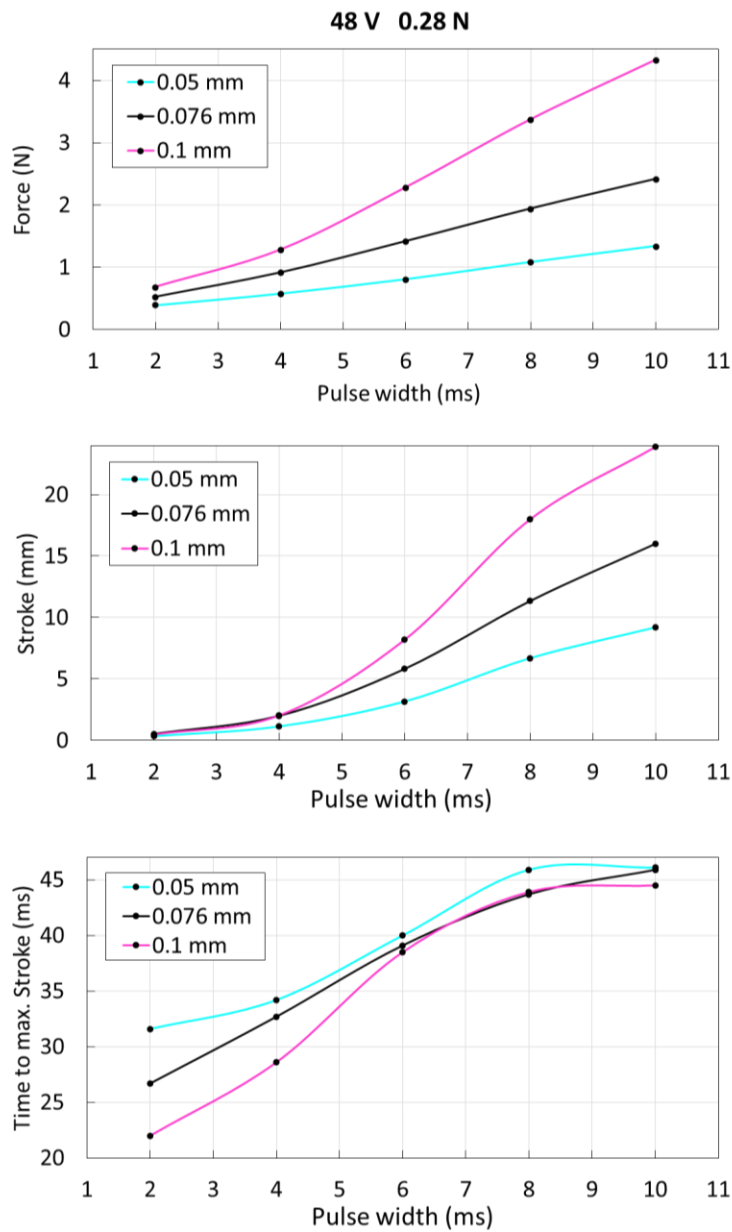
Figure 5.8: Comparison of maximum force (upper part), maximum stroke (center part) and time delay to reach maximum stroke (lower part) for three different SMA wire diameters (50 µm, 76 µm, 100 µm). The experiments are run at 48 V supply voltage and an initial load of 0.28 N.
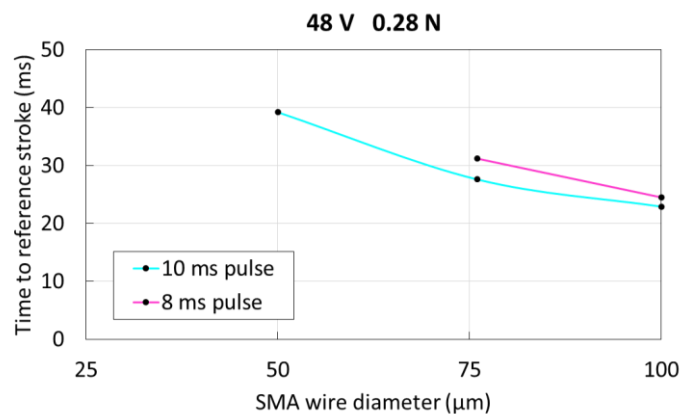
Figure 5.9: Time delays to reach the reference stroke of 8.33 mm for different SMA wire diameters activated with an 8 ms and a 10 ms pulse at 48 v supply voltage.

Figure 5.10: Comparison of maximum force (upper part), maximum stroke (center part) and time delay to reach maximum stroke (lower part) for three different voltage supply levels (24 V, 48 V, 125 V). The experiments are run with a 76 µm SMA wire and an initial load of 0.28 N.
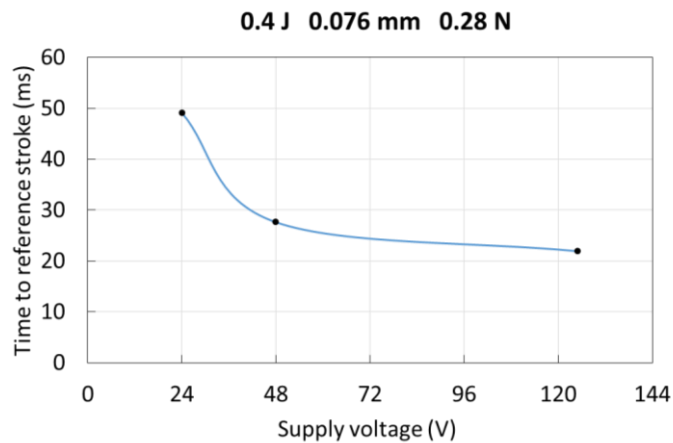
Figure 5.11: Time delays to reach the reference stroke of 8.33 mm for different supply voltages. The 76 µm SMA wire is always activated with a total energy of 0.4 J.

5.3.3 **Energy Analysis**

The minimum energy for a phase transformation is reached under adiabatic conditions. This means that no energy is lost through heat flow to the environment during the process. This minimum energy can be calculated with (5.4). The energy to heat a SMA wire (76 µm) from room temperature to transformation temperature ($\Delta T = 65\ K$) is calculated with the specific heat capacity $c = 500\ J/(kg \cdot K)$ and the mass $m_{SMA} = 6.58\ m$. The term $h \cdot m_{SMA}$ in (5.4) describes the latent heat of the phase transformation with $h \approx 20\ J/g$ [14]. The theoretical minimum energy for a full phase transformation is calculated as $W_{min} = 0.345\ J$.

In the first exemplary experiment, which serves as the reference, a 76 µm SMA wire is activated in the conventional way using the suggested current of 150 mA in the datasheet [15]. The SMA wire is activated with an activation pulse width of 1 s. The displacement reaches the value of 8.33 mm, which corresponds to a 3.7 % stroke. The same wire is then activated at increasing voltages. At each set voltage, the activation pulse time (pulse width) is slowly increased until a displacement of 8.33 mm is reached. In all experiments, the initial force in the SMA wire is 0.28 N and a spring rate of 0.056 N/mm is used. The results of these experiments are shown in Table 11. The activation delay describes the time interval from the start of activation until the bottom clamp of the SMA wire reaches maximum displacement of 8.33 mm.

The experimental results and observed tendencies are presented in Figure 5.12. The necessary pulse width to reach the reference displacement decreases dramatically between 8 V and 16 V, and stays almost constant after 24 V (a). The energy consumption shows a very similar behavior (c), as it is directly linked to the pulse width (d). Interestingly, also the activation delay mimics this behavior (b). The reason for this is the experimental procedure focusing on energy consumption analysis. If no energy is lost because the experiment runs under adiabatic conditions, the same total energy amount is necessary to generate a constant displacement output, which relates to a constant potential energy. At higher electrical powers, the initial force and thus the acceleration of the mass increases but at the same time the pulse width, which describes the acceleration interval, is decreased. This leads to a constant average velocity and activation delay. If shorter activation delays at the same displacement are desired, the pulse width can be increased at high electrical power. In this scenario, the displacement could be limited by a hard stop in the construction.

Table 11: Comparison of activation speed and energy consumption at different activation pulse widths for a 76 µm SMA wire. The last column indicates the percentage of energy needed in comparison to the reference at 8V.

Voltage [V]	Displacement [mm]	Pulse width [ms]	Activation delay [ms]	Energy [J]	Ratio [%]
8	8.33	1000	1008	1.2	100
12	8.33	226	237.1	0.637	53.1
16	8.33	77	95.2	0.370	30.8
24	8.33	29.2	57.2	0.305	25.4
30	8.33	17.7	49	0.288	24
35	8.33	12.8	45.8	0.282	23.5
40	8.33	9.74	43.9	0.280	23.3
48	8.33	6.71	42	0.277	23.1
70	8.33	3.08	39.7	0.272	22.7
110	8.33	1.21	38.5	0.267	22.3
125	8.33	0.94	38.3	0.266	22.2
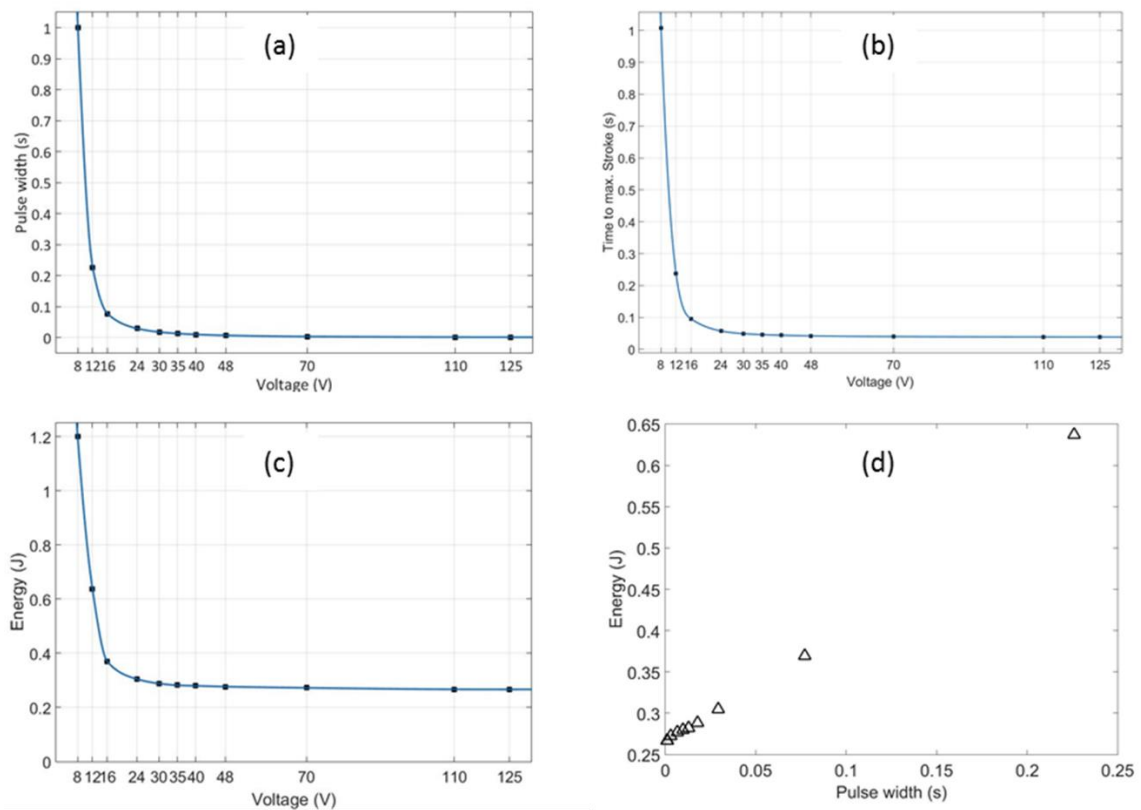
Figure 5.12: Graphical illustration of experimental results regarding activation pulse (a) activation speed (b) and energy consumption (c) in relation to the supply voltage and energy consumption in relation to the activation pulse (d) for a 76 µm diameter SMA wire.

The energy consumption for pulse widths between 1 ms and 30 ms is very similar. With a 77 ms activation pulse at 16 V, the energy consumption starts to increase more rapidly. The results of these experiments suggest that activation pulse widths up to almost 30 ms result in nearly adiabatic conditions. To verify these observations from a theoretical point of view, an estimate time interval for adiabatic conditions can be calculated. The temperature of a body according to Newton's law of cooling is determined by

$$T(t) = T_0 \cdot e^{-t/\tau}. \tag{5.5}$$

The time constant τ in this thermal process is described with the product of thermal resistance and heat capacity:

$$\tau = C_{th} \cdot R_{th}. \tag{5.6}$$

With a heat capacity of $C_{th} = c \cdot m = 3.292\,mJ/K$ and a thermal resistance of $R_{th} = 1/(\alpha \cdot A) = 1861\,K/W$, the time constant τ for the cooling process can be calculated. The heat transfer coefficient α for the convective cooling process of the SMA wire at room temperature can vary between 10-100 W/(K·m²). Usually values close to 10 W/(K·m²) are chosen to represent conditions with minimal air flow. The parameter A describes the heat transfer surface area of the SMA wire. With the time constant τ and (5.5) the time interval for a near adiabatic phase transformation can now be determined. Considering a 1 % cooling of the wire, this time interval is calculated as $t = -\ln(0.99) \cdot \tau$. Using the parameters in this experiment, time intervals between 6.2-61.6 ms are theoretically possible. The observed value of 30 ms relates to a heat transfer coefficient α of 20 W/(K·m²), which is highly reasonable for the considered setup. For this SMA wire diameter, the experimental results for the energy consumption during a high voltage SMA actuation are even slightly lower (22.2 %) than the calculated theoretical minimum (28.8 %). This minimum was calculated assuming a complete phase transformation, but the displacement in the experiments relates to a stroke of only 3.7 %. For complete phase transformation, strokes of 4-5 % can be expected. Additionally, the displacement in the experiments at voltage values equals or larger than 16 V was reached due to the ballistic effect, which means that even less phase transformation, has taken place. On the other hand, the calculation of this energy minimum does not take into account the increasing austenite start temperature for the phase transformation under mechanical stress. As stated above, the transformation temperatures generally changes with a factor of 0.11-0.14 K/MPa. Since

the mechanical stress is not constant during the actuation, the transformation temperature will change constantly during the activation process. In summary, the actual energy balance in these experiments cannot be trivially calculated, but a magnitude of possible exemplary energy savings can be determined. In addition to the absolute energy value, also the experimentally identified time interval for adiabatic conditions matches the theoretical considerations.

The same measurement sequence is performed for the SMA wire diameters of 50 µm and 100 µm. The total energy consumption at the different supply voltages is illustrated in Figure 5.13. At low voltages, the thin wires need more energy to reach the same stroke. Thin wires have a higher surface-to-volume ratio and thus lose more energy to the environment during non-adiabatic activation. Between 12 V and 16 V the SMA wire starts to reach the adiabatic region and the energy consumption settles at near constant values. At these voltages, the thin wires need the least amount of energy. The two components of energy have been introduced in (5.4). First, the SMA has to be heated to the transformation temperature $(m \cdot c \cdot \Delta T)$. After that, energy is consumed by the latent heat of the phase transformation $(h \cdot m)$. In small diameter SMA wires is less material to be heated up before the actual phase transformation can begin.
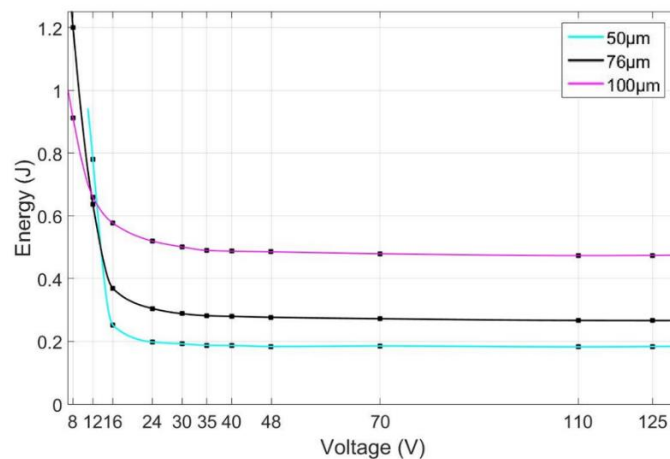
Figure 5.13: Total energy consumption for three different SMA wire diameters.

The different energy levels for the SMA wire diameters lead to almost identical pulse widths at set voltages (Figure 5.14). The expanded diagram (Figure 5.14, center part) shows that the pulse widths are always slightly higher for thinner SMA wires. In relation to the total energy consumption, the pulse width of the thin wires rapidly increases once the activation starts leaving adiabatic regions (Figure 5.14, lower part). In that case, the thicker SMA wires quickly become more energy-efficient because of their smaller surface-to-volume ratio.
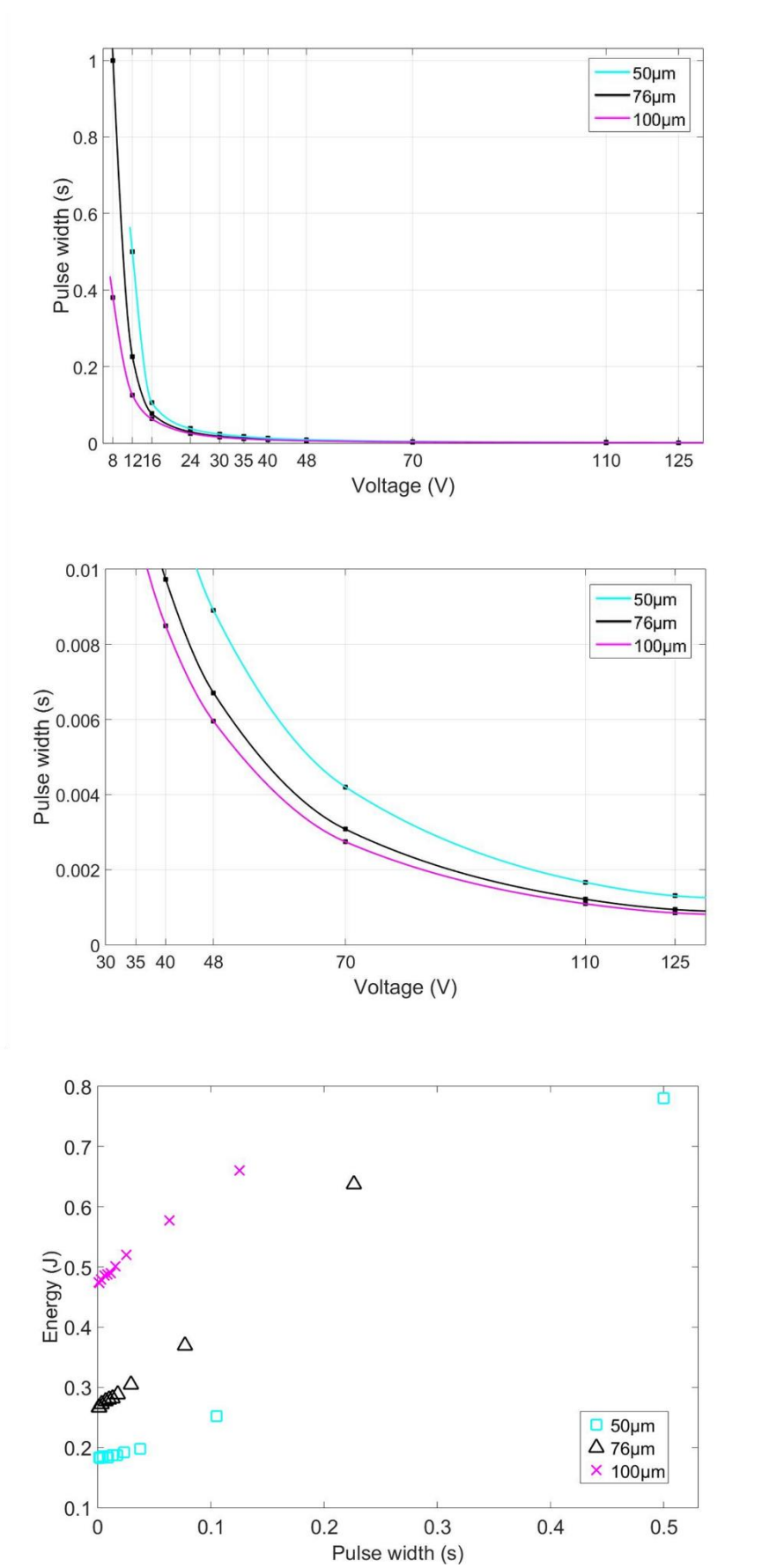
Figure 5.14: Comparison of the activation pulse widths in relation to the supply voltage (upper part) with zoomed-in graph (center part) and in relation to the energy consumption (lower part) for three different SMA wire diameters.

Similarly, to the pulse width, the activation speed is almost identical for the different SMA wires, provided that they are activated under adiabatic conditions (Figure 5.15). The zoomed-in graph (Figure 5.15, lower part) indicates that the thicker SMA wires are slightly faster than the smaller wire diameters, which is related to higher acceleration forces in thicker SMA wires due to the higher electrical power for activation.
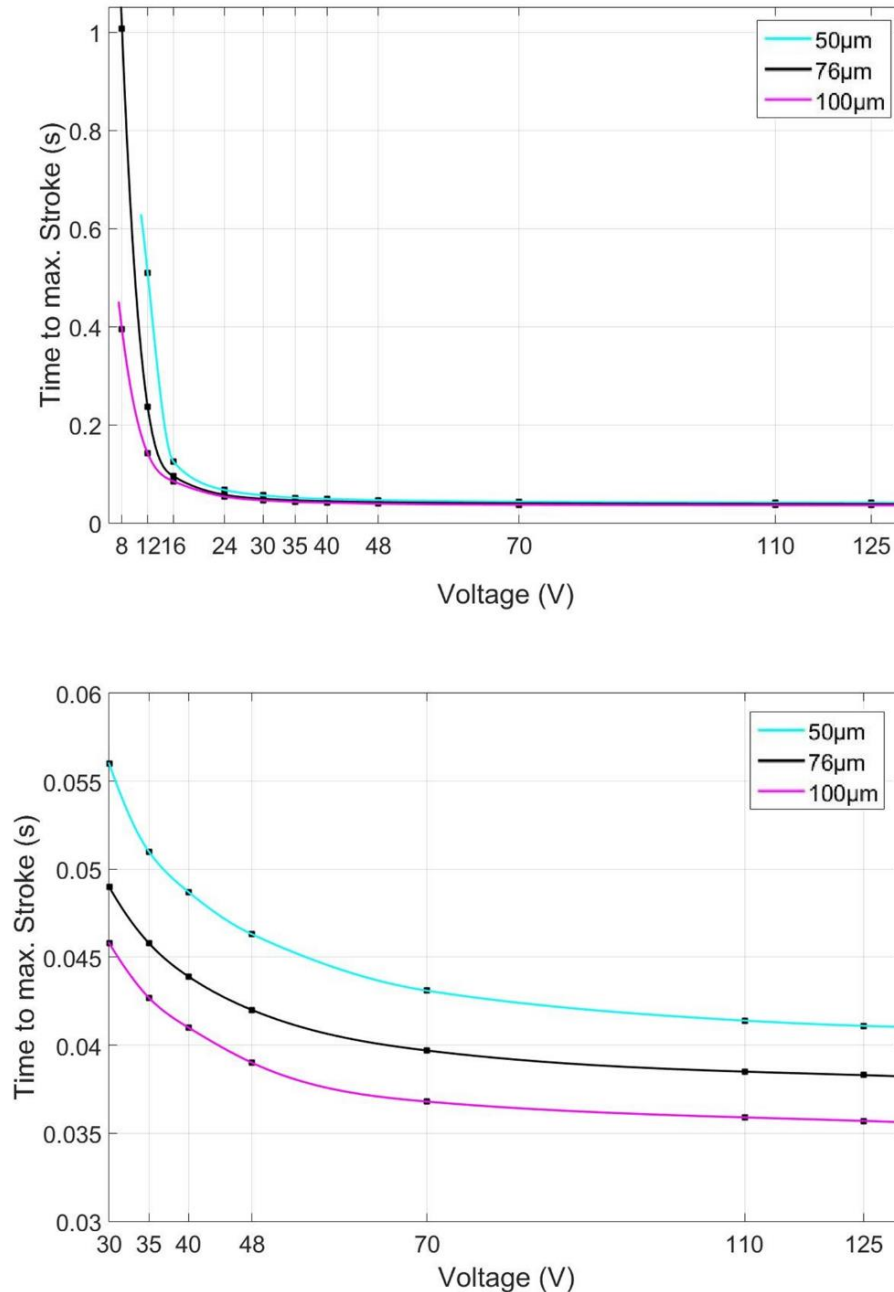
Figure 5.15: Comparison of the activation speed in relation to the supply voltage (upper part) with zoomed-in graph (lower part).

5.4   Summary and Future Work: High-Speed Activation

Instead of relying on complex and cost-intensive power electronics for current control, it has been shown that the novel control strategy can be performed with simplified hardware capable of applying a short voltage impulse for a short period of time. Advantages of the proposed strategy regarding SMA actuator performance are high actuation speeds and lower energy consumption. In addition, it is shown how high accelerations can lead to ballistic effects, which are responsible for a large actuation stroke. Once activated, the actuator system starts oscillating, according to a mass-spring-damper dynamics. The presented exemplary experiment showed activation times in the range of 40 ms for strokes of close to 10 % of the SMA wire length. With shorter activation pulses, energy consumption during activation is minimized, because no heat is lost to the environment. This adiabatic heating is already reached at moderate voltages around 24 V for the 76 µm wire. An analytical method of estimating the minimum energy for the SMA actuation and the maximum time interval for adiabatic conditions has also been demonstrated and discussed. Energy savings up to 80 % have been achieved.

Possible applications for this SMA activation could be in the field of release mechanisms, safety applications or switches, where only a single actuation or low frequency activations are needed. As an example, an SMA actuator could be used to release a spring-loaded system, in which dynamic effects like oscillations do not have any negative influence on the actuator performance.

In a next step, the experimental setup will be improved with an additional force measurement at the moving end of the SMA wire for a better force-acceleration correlation during the actuation. Further research will focus on the investigation of SMA actuation with high AC voltage, specifically looking at mains voltages like 130 V in the United States and 230 V in Europe.

6 Conclusion and Outlook

This thesis provides advanced design concepts and a novel activation method for SMA based actuator systems. Even though SMA technology has been known for decades and their functionality and reliability has been proven in applications, there are only few commercial products on the market, especially in the field of SMA actuators. Despite a large amount of advantages that come with SMA technology, several drawbacks have delayed a more widespread usage. On the one hand, engineers not familiar with the technology and its behavior rather use well-established and proven alternatives and, on the other hand, SMA wires oftentimes are accompanied by preconceptions of slow actuation times, high energy consumption and limited stroke output. The design and control concepts presented in this thesis aim at eliminating said drawbacks and provide engineers with guidelines for actuator design with SMA wires.

Applied SMA actuator design with linear springs is demonstrated at the examples of two case studies. A linear actuator concept is used in an SMA based vacuum suction cup for the handling of plane work pieces. The design steps include kinematic and kinetic studies of the system and the determination of the design parameters by solving linear systems of equations. The actuator system's dynamics are improved by using multiple thin wires with a high surface to volume ratio for efficient cooling and the energy-efficiency is improved by adjusting the kinematic concept to the suction cup's operating cycle. The application of a reconfigurable end-effector is used to demonstrate generation of rotary motion through SMA wire actuators. In the exemplary design framework, graphical methods are used to identify optimal design parameters. Energy consumption is minimized by a special locking mechanism that allows energy free holding of intermediate positions along the rotational radius.

An advanced actuator concept is presented using a bi-stable spring actuator. The bi-stability creates two energy-free actuator configurations so that only short activation pulses are necessary to switch between states. The antagonistic SMA wire configuration attached to the bi-stable element is able to realize higher actuation frequencies, because the bi-stable element may actively be forced in both directions even when the respective passive wire has not yet completely cooled down. The experimental study reveals crucial parameters in actuator design with bi-stable springs, such as the lever arm of the SMA wire attachment.

With short distances between pivot point and SMA wire attachment, stroke magnification of one order of magnitude and more becomes possible.

Instead of relying on special power controllers, it is demonstrated how SMA wires can be activated with power supplies at standard voltage levels. By limiting the activation pulse length and thus the energy input, SMA wires can be activated at very high voltages and electric power. With this control concept, very fast actuation times are achieved. Dynamic acceleration effects can lead to artificial stroke amplification up to a factor two and more. High-speed activation additionally leads to an optimized energy balance, because in near adiabatic activation, no energy is lost to the environment while heating the SMA wire.

All of the presented concepts and methods provide engineers with tools for the realization of SMA-based products or the improvement of prototypes eliminating typical drawbacks of SMA technology. In addition, a combination of a bi-stable actuator and high-speed activation is possible. Now, application fields, which fit the physical and material properties of SMA wires, have to be found and engineers have to be sensitized to the potential of the technology in comparison to state-of-the-art drives and motors.

References

[1]   J. G. Boyd and D. C. Lagoudas, "Thermomechanical Response of Shape Memory Composites," *J. Intell. Mater. Syst. Struct.*, vol. 5, no. 3, pp. 333–346, May 1994.

[2]   H. Funakubo, *Shape Memory Alloys*, vol. 1, no. D. Amsterdam: Gordon and Breach Science Publ., 1987.

[3]   S. Langbein and A. Czechowicz, *Konstruktionspraxis Formgedächtnistechnik*, vol. 1. Wiesbaden: Springer Fachmedien, 2013.

[4]   H. Janocha, *Unkonventionelle Aktoren - Eine Einführung*, 2. München: Oldenburg Verlag, 2013.

[5]   R. Britz, "Entwicklung eines skalierbaren Rotationsaktors auf Basis von Formgedächtnislegierungsdrähten," Saarland University, 2016.

[6]   Y. Goergen, "Entwicklung eines rekonfigurierbaren Endeffektors mit Formgedächtnisantrieb," Saarland University, 2016.

[7]   P. L. Reece, *Progress in smart materials and structures*. New York: Nova Science Publishers, Inc., 2007.

[8]   J. Klaput, "Studies of selected mechanical properties of nitinol − shape memory alloy," *Arch. FOUNDRY Eng.*, vol. 10, no. 3/2010, pp. 155–158, 2010.

[9]   L. C. Chang and T. A. Read, "Transducers," *Amer. Inst. Min. Engrs.*, vol. 191, p. 47, 1951.

[10]   L. C. Chang, "Atomic Displacements and Crystallographic Mechanism in Diffusionless Transformation of Gold-Cadmium Single Crystals containing 47"5 atomic percent Cadmium," *Acta Crystallogr.*, vol. 4, pp. 320–324, 1951.

[11]   W. Buehler, J. Gilfrich, and R. Wiley, "Effect of low temperature phase changes on the mechanical properties of alloys near composition TiNi.," *J Appl Phys*, 1963.

[12]   E. Just, "Entwicklung eines Formgedächtnis-Mikrogreifers," Universität Karlsruhe, 2001.

[13]   M. Kaack, "Elastische Eigenschaften von NiTi- Formgedächtnis-Legierungen," Ruhr-Universität Bochum, 2002.

[14]   Dynalloy Inc., "Technical Characteristics of Flexinol Actuator Wires," 2017. [Online]. Available: http://www.dynalloy.com/pdfs/TCF1140.pdf. [Accessed: 01-Mar-2018].

[15]   SAES Getters, "SmartFlex Brochure," 2017. [Online]. Available: https://www.saesgetters.com/sites/default/files/SmartFlex   Brochure_2.pdf. [Accessed: 01-Mar-2018].

[16]   H. Janocha, *Adaptronics and Smart Structures*, 2. Berlin Heidelberg: Springer Verlag, 2007.

[17]   F. Schiedeck, "Entwicklung eines Modells für Formgedächtnisaktoren im geregelten dynamischen Betrieb," Gottfried Wilhelm Leibniz Universität Hannover, 2009.

[18]   J. Mohd Jani, M. Leary, A. Subic, and M. A. Gibson, "A review of shape memory alloy research, applications and opportunities," *Materials and Design*, vol. 56. pp. 1078–1113, 2014.

[19]   B. Bauer, "Formgedächtnislegierungen in der Antriebstechnik: Aktoren in Getrieben und Kupplungen; Kerbwirkungszahlen," Ruhr-Universität Bochum, 2010.

[20]   D. C. Lagoudas, *Shape Memory Alloys: Modeling and Engineering Applications*. New York: Springer, 2008.

[21]   L. Lecce and A. Concilio, *Shape memory alloy engineering: for aerospace, structural and biomedical applications*. Oxford: Elsevier, 2015.

[22]   M. Bäker, *Funktionswerkstoffe - Physikalische Grundlagen und Prinzipien*.

Wiesbaden: Springer Vieweg, 2014.

[23] K. D. Skrobanek, O. F. Hagena, and M. Kohl, "Entwicklung von Mikromembran Aktoren mit NiTi-Formgedächtnislegierungen," Karlsruhe, 1998.

[24] N. Lewis, A. York, and S. Seelecke, "Experimental characterization of self-sensing SMA actuators under controlled convective cooling," *Smart Mater. Struct.*, vol. 22, no. 9, p. 094012--, 2013.

[25] V. Antonucci, G. Faiella, M. Giordano, F. Mennella, and L. Nicolais, "Electrical resistivity study and characterization during NiTi phase transformations," *Thermochim. Acta*, vol. 462, no. 1–2, pp. 64–69, Oct. 2007.

[26] V. Novák, P. Šittner, G. N. Dayananda, F. M. Braz-Fernandes, and K. K. Mahesh, "Electric resistance variation of NiTi shape memory alloy wires in thermomechanical tests: Experiments and simulation," *Mater. Sci. Eng. A*, vol. 481–482, pp. 127–133, May 2008.

[27] H. H. Bruun, *Hot-wire anemometry: principles and signal analysis*. 1995.

[28] S. J. Furst and S. Seelecke, "Modeling and experimental characterization of the stress, strain, and resistance of shape memory alloy actuator wires with controlled power input," *J. Intell. Mater. Syst. Struct.*, vol. 23, no. 11, pp. 1233–1247, May 2012.

[29] M. E. Pausley, S. J. Furst, V. Talla, and S. Seelecke, "Electro-mechanical behavior of a shape memory alloy actuator," *Proc. SPIE - Int. Soc. Opt. Eng.*, 2009.

[30] N. Ma, G. Song, and H.-J. Lee, "Position control of shape memory alloy actuators with internal electrical resistance feedback using neural networks," *Smart Mater. Struct.*, vol. 13, no. 4, pp. 777–783, Aug. 2004.

[31] P. Motzki, S. Hau, M. Schmidt, and S. Seelecke, "Künstliche Muskeln und Nerven in Industrie 4.0 Konzepten," *Ind. 4.0 Manag.*, vol. 2018, no. 4, pp. 38–41, Aug. 2018.

[32] Actuator Solutions GmbH, "Actuator Solutions SMA Products," 2018. [Online]. Available: http://www.actuatorsolutions.de/products/. [Accessed: 01-Mar-2018].

[33] M. Köpfer, "Industrialisierung der FGL-Technologie in hochvolumigen Serienprodukt," *VDI-Expertenforum: Smart Materials – aus der Forschung in die industrielle Anwendung*. Karlsruhe, 2017.

[34] J. Jayender, M. Azizian, and R. V. Patel, "Autonomous image-guided robot-assisted active catheter insertion," *IEEE Trans. Robot.*, 2008.

[35] S. J. Furst, G. Bunget, and S. Seelecke, "Design and fabrication of a bat-inspired flapping-flight platform using shape memory alloy muscles and joints," *Smart Mater. Struct.*, vol. 22, no. 1, p. 014011, 2013.

[36] F. Simone, G. Rizzello, and S. Seelecke, "Metal muscles and nerves - A self-sensing SMA-actuated hand concept," *Smart Mater. Struct.*, 2017.

[37] A. Menciassi, S. Gorini, G. Pernorio, and P. Dario, "A SMA actuated artificial earthworm," in *IEEE International Conference on Robotics and Automation, 2004. Proceedings. ICRA '04. 2004*, 2004, vol. 4, p. 3282–3287 Vol.4.

[38] K. R. Cha, G. H. Kim, J. H. Kim, and S. H. Jeong, "A Study on Anthropomorphic Robot Hand Simulation Driven by SMA Wire Using Segment Control," *Key Eng. Mater.*, vol. 345–346, pp. 1249–1252, Aug. 2007.

[39] C.-C. Lan and Y.-N. Yang, "A Computational Design Method for a Shape Memory Alloy Wire Actuated Compliant Finger," *J. Mech. Des.*, vol. 131, no. 2, p. 021009, Feb. 2009.

[40] M. Kohl, *Shape Memory Microactuators*. Berlin Heidelberg: Springer Verlag, 2004.

[41] M. Kohl and K. D. Skrobanek, "Linear microactuators based on the shape memory effect," in *Proceedings of International Solid State Sensors and Actuators Conference (Transducers '97)*, vol. 2, pp. 785–788.

[42] T. Duerig, D. Stoeckel, and D. Johnson, "SMA: smart materials for medical applications," *Proc. SPIE*, 2003.

[43] J. H. Crews, "Development of a Shape Memory Alloy Actuated Robotic Catheter for Endocardial Ablation: Modeling, Design Optimization, and Control," 2011.

[44] A. S. Veeramani, G. D. Buckner, S. B. Owen, R. C. Cook, and G. Bolotin, "Modeling the dynamic behavior of a shape memory alloy actuated catheter," *Smart Mater. Struct.*, vol. 17, no. 1, p. 015037, Feb. 2008.

[45] L. L. Stepan, D. S. Levi, and G. P. Carman, "A Thin Film Nitinol Heart Valve," *J. Biomech. Eng.*, vol. 127, no. 6, p. 915, Nov. 2005.

[46] G. Bunget, "BATMAV - A Bio-Inspired Micro-Aerial Vehicle For Flapping Flight," North Carolina State University, 2011.

[47] Y. Fu, W. Huang, H. Du, X. Huang, J. Tan, and X. Gao, "Characterization of TiNi shape-memory alloy thin films for MEMS applications," *Surf. Coatings Technol.*, vol. 145, no. 1–3, pp. 107–112, Aug. 2001.

[48] F. T. Calkins and J. H. Mabe, "Shape Memory Alloy Based Morphing Aerostructures," *J. Mech. Des.*, vol. 132, no. 11, p. 111012, Nov. 2010.

[49] M. Kohl, M. Popp, and B. Krevet, "Shape memory micromechanisms for microvalve applications," in *Proceedings Volume 5387, Smart Structures and Materials 2004: Active Materials: Behavior and Mechanics*, 2004.

[50] L. M. Gravatt, J. H. Mabe, F. T. Calkins, and D. J. Hartl, "Characterization of varied geometry shape memory alloy beams," in *SPIE Smart Structures and Materials + Nondestructive Evaluation and Health Monitoring*, 2010, p. 76450U–76450U–12.

[51] D. Clausi *et al.*, "Wafer-level mechanical and electrical integration of SMA wires to silicon MEMS using electroplating," in *2011 IEEE 24th International Conference on Micro Electro Mechanical Systems*, 2011, pp. 1281–1284.

[52] Y. Fu, H. Du, W. Huang, S. Zhang, and M. Hu, "TiNi-based thin films in MEMS applications: a review," *Sensors Actuators A Phys.*, vol. 112, no. 2–3, pp. 395–408, May 2004.

[53] J. J. Epps and I. Chopra, "In-flight tracking of helicopter rotor blades using shape memory alloy actuators," *Smart Mater. Struct.*, vol. 10, no. 1, pp. 104–111, Feb. 2001.

[54] S. J. Furst and S. Seelecke, "Experimental validation of different methods for controlling a flexible nozzle using embedded SMA wires as both positioning actuator and sensor," in *SPIE Smart Structures and Materials + Nondestructive Evaluation and Health Monitoring*, 2011, p. 79781K.

[55] S. J. Furst and S. Seelecke, "Fabrication and characterization of a dual-joint smart inhaler nozzle actuated by embedded SMA wires," *Smart Mater. Struct.*, vol. 23, no. 3, p. 35008, 2014.

[56] M. Cho and S. Kim, "Structural morphing using two-way shape memory effect of SMA," *Int. J. Solids Struct.*, vol. 42, no. 5–6, pp. 1759–1776, Mar. 2005.

[57] G. Bunget and S. Seelecke, "BATMAV: A Biologically-Inspired Micro-Air Vehicle for Flapping Flight – Kinematic Modelling," 2007.

[58] S. Saadat *et al.*, "An overview of vibration and seismic applications of NiTi shape memory alloy," *Smart Mater. Struct.*, vol. 11, no. 2, pp. 218–229, Apr. 2002.

[59] Q. Chen and C. Levy, "Vibration analysis and control of flexible beam by using smart damping structures," *Compos. Part B Eng.*, vol. 30, no. 4, pp. 395–406, Jun. 1999.

[60] P. Motzki, F. Simone, and S. Seelecke, "Shape Memory Alloy Actuators in Industrial Applications," *GMA-FA 4.16 "Unkonventionelle Aktorik" im VDI/VDE-Fachbereich Mechatronik, Robotik und Aktorik, Workshop der Nachwuchswissenschaftler*. VDI, Saarbrücken, Germany, 2014.

[61] S. Seelecke, "Thermische Formgedächtnislegierungen – vom Werkstoff auf dem Weg zum Produkt," *VDI-Expertenforum: Smart Materials – aus der Forschung in die industrielle Anwendung*. Karlsruhe, 2017.

[62]   O. Mailahn, P. Motzki, R. Müller, and S. Seelecke, "Innovative Greifplanungskonzepte und rekonfigurierbare Greiftechnologie," *VDI-Fachtagung Industrielle Robotik 2014*. Baden-Baden, Germany, 2014.

[63]   P. Motzki, J. Kunze, A. York, and S. Seelecke, "Energy-efficient SMA Vacuum Gripper System," in *Actuator 16 - 15th International Conference on New Actuators*, 2016, pp. 526–529.

[64]   J. Kunze, P. Motzki, B. Holz, A. York, and S. Seelecke, "Realization of a Vacuum Gripper System Using Shape Memory Alloy Wires," in *Actuator 14 - 14th International Conference on New Actuators*, 2014, pp. 210–213.

[65]   F. Khelfa, L. Zimmer, P. Motzki, and S. Seelecke, "Development of a Reconfigurable End-Effector Prototype," in *ASME 2017 Conference on Smart Materials, Adaptive Structures and Intelligent Systems - SMASIS17*, 2017, p. V002T04A011.

[66]   E. Williams and M. H. Elahinia, "An Automotive SMA Mirror Actuator: Modeling, Design, and Experimental Evaluation," *J. Intell. Mater. Syst. Struct.*, vol. 19, no. 12, pp. 1425–1434, May 2008.

[67]   E. Zimmerman, V. Muntean, T. Melz, B. Seipel, and T. Koch, "Novel pre-crash-actuator-system based on SMA for enhancing side impact safety," in *Advanced Microsystems for Automotive Applications 2009: Smart Systems for Safety, Sustainability, and Comfort*, 2009.

[68]   G. Bunget and S. Seelecke, "BATMAV: a 2-DOF bio-inspired flapping flight platform," *Act. Passiv. Smart Struct. Integr. Syst.*, 2010.

[69]   M. Pausley and S. Seelecke, "Design of a Smart Inhaler System for Improved Aerosol Drug Delivery," *Journal of Medical Devices*, vol. 2, no. 2. p. 027534, 2008.

[70]   C. Kleinstreuer, Z. Zhang, Z. Li, W. L. Roberts, and C. Rojas, "A new methodology for targeting drug-aerosols in the human respiratory system," *Int. J. Heat Mass Transf.*, vol. 51, no. 23–24, pp. 5578–5589, Nov. 2008.

[71]   Z. Zhang, C. Kleinstreuer, and C. S. Kim, "Comparison of analytical and CFD models with regard to micron particle deposition in a human 16-generation tracheobronchial airway model," *J. Aerosol Sci.*, 2009.

[72]   P. Motzki, B. Holz, F. Simone, and S. Seelecke, "Formgedächtnislegierungen in Applikationen der Greif- und Handhabungstechnologie - Shape Memory Alloys in Applications of Gripping- and Material-Handling-Technology," in *Fachtagung Mechatronik 2015*, 2015, pp. 55–60.

[73]   C. Rossi, A. Barrientos Cruz, and W. Coral Cuellar, "Sma control for bio-mimetic fish locomotion." E.T.S.I. Industriales (UPM), 12-Jul-2010.

[74]   J. M. Hollerbach, I. W. Hunter, and J. A. Ballantyne, "Comparative analysis of actuator technologies for robotics," *Robot. Rev. 2*, pp. 299–342, 1992.

[75]   R. Müller, S. Seelecke, M. Vette, O. Mailahn, and P. Motzki, "Rekonfigurierbares Handhabungssystem zur Handhabung von Großbauteilen mit adaptiven Sauggreifern bestehend aus Formgedächtnislegierungen," in *Bewegungstechnik 2014*, 2014, pp. 117–134.

[76]   P. Motzki, Y. Goergen, A. York, and S. Seelecke, "Reconfigurable SMA End-effector for Material Handling," in *Actuator 16 - 15th International Conference on New Actuators*, 2016, pp. 522–525.

[77]   P. Motzki, J. Kunze, B. Holz, A. York, and S. Seelecke, "Adaptive and Energy efficient SMA-based Handling Systems," in *SPIE - Active and Passive Smart Structures and Integrated Systems 2015*, 2015, vol. 9431, p. 943116.

[78]   S. K. Chaitanya. and K. Dhanalakshmi, "Demonstration of self-sensing in Shape Memory Alloy actuated gripper," in *IEEE International Symposium on Intelligent Control - Proceedings*, 2013.

[79]   G. Tu, C. Xie, G. Yao, Q. Zong, and X. Tang, "A new robot SMA bearing's gripper,"

Ind. Technol. 1994. Proc. IEEE Int. Conf., 1994.

[80] A. Khodayari, M. M. Kheirikhah, and B. Zarefar, "Fabrication a practical SMA actuated gripper," in *2011 IEEE International Conference on Robotics and Biomimetics, ROBIO 2011*, 2011.

[81] Z. W. Zhong and C. K. Yeong, "Development of a gripper using SMA wire," *Sensors Actuators, A Phys.*, 2006.

[82] S. Yan, T. Yang, X. Liu, and R. Wang, "Tactile feedback control for a gripper driven by SMA springs," *AIP Adv.*, 2012.

[83] S. K. Chaitanya and K. Dhanalakshmi, "Design and investigation of a shape memory alloy actuated gripper," *Smart Struct. Syst.*, 2014.

[84] A. Manuelle Bertetto and M. Ruggiu, "A Two Degree of Freedom Gripper Actuated by SMA with Flexure Hinges," *J. Robot. Syst.*, 2003.

[85] F. Simone, P. Motzki, B. Holz, and S. Seelecke, "Bio-inspirierter Drei-Finger-Greifer mit Formgedächtnisaktorik," in *Technische Unterstützungssysteme*, R. Weidner, T. Redlich, and J. P. Wulfsberg, Eds. Hamburg, Germany: Springer Berlin Heidelberg, 2015, pp. 194–195.

[86] F. Simone, P. Motzki, B. Holz, and S. Seelecke, "Ein bio-inspirierter 3-Finger-Greifer mit Formgedächtnisaktorik - A Bio-Inspired SMA-Based 3-Finger-Gripper," in *Erste transdisziplinäre Konferenz zum Thema "Technische Unterstützungssysteme, die die Menschen wirklich wollen,"* 2014, pp. 420–426.

[87] S. Dilibal, E. Guner, and N. Akturk, "Three-finger SMA robot hand and its practical analysis," *Robotica*, 2002.

[88] K. Yang and Y. Wang, "Design, drive and control of a novel SMA-actuated humanoid flexible gripper," *J. Mech. Sci. Technol.*, 2008.

[89] S. Jung, J. Bae, and I. Moon, "Lightweight prosthetic hand with five fingers using SMA actuator," *Control. Autom. Syst. (ICCAS), 2011 11th Int. Conf.*, 2011.

[90] S. Bressers, S. Chung, A. Villanueva, C. Smith, and S. Priya, "JetSum: SMA actuator based undersea unmanned vehicle inspired by jellyfish bio-mechanics," 2010, vol. 7644, p. 76440G–7644–9.

[91] C. Smith, A. Villanueva, K. Joshi, Y. Tadesse, and S. Priya, "Working principle of bio-inspired shape memory alloy composite actuators," *Smart Mater. Struct.*, 2011.

[92] G. Bunget and S. Seelecke, "Batmav - Development and testing of a SMA-based bio-inspired flapping platform," in *ASME 2010 Conference on Smart Materials, Adaptive Structures and Intelligent Systems, SMASIS 2010*, 2010.

[93] M. Kohl, B. Krevet, and E. Just, "SMA microgripper system," *Sensors Actuators A Phys.*, vol. 97–98, pp. 646–652, Apr. 2002.

[94] C. C. Lan, C. M. Lin, and C. H. Fan, "A Self-Sensing Microgripper Module With Wide Handling Ranges," *IEEE/ASME Trans. Mechatronics*, vol. 16, no. 1, pp. 141–150, 2011.

[95] S. J. J. Furst, "Design, Fabrication, and Control Methods for Exploiting the Multifunctional Sensing and Actuation Capabilities of Shape Memory Alloy Wires," Saarland University, 2012.

[96] C. C. Kessens and J. P. Desai, "Versatile Passive Grasping for Manipulation," *IEEE/ASME Trans. Mechatronics*, vol. 21, no. 3, pp. 1293–1302, 2016.

[97] A. Firouzeh and J. Paik, "Grasp Mode and Compliance Control of an Underactuated Origami Gripper Using Adjustable Stiffness Joints," *IEEE/ASME Trans. Mechatronics*, vol. 22, no. 5, pp. 2165–2173, 2017.

[98] J. Luntz, B. Barnes, D. Brei, P. W. Alexander, A. Browne, and N. L. Johnson, "SMA wire actuator modular design framework," in *Proceedings of SPIE - The International Society for Optical Engineering 7290*, 2009.

[99] O. Benafan *et al.*, "Shape memory alloy actuator design: CASMART collaborative best practices and case studies," *Int. J. Mech. Mater. Des.*, vol. 10, no. 1, pp. 1–42,

2014.

[100] R. W. Wheeler *et al.*, "Engineering Design Tools for Shape Memory Alloy Actuators: CASMART Collaborative Best Practices and Case Studies," in *ASME 2016 Conference on Smart Materials, Adaptive Structures and Intelligent Systems*, 2016, p. V001T04A010.

[101] D. Reynaerts and H. Van Brussel, "Design aspect of shape memory actuators," *Mechatronics*, vol. 8, pp. 635–656, 1998.

[102] T. W. Duerig and K. N. Melton, "Designing with the shape memory effect," *Mater. Res. Soc. Symp. Proc.*, vol. 9, p. 581, 1989.

[103] T. W. Duerig, K. N. Melton, D. Stöckel, and C. M. Wayman, *Engineering Aspects of Shape Memory Alloys*. London: Butterworth-Heinemann, 1990.

[104] M. Sreekumar, T. Nagarajan, and M. Singaperumal, "Design of a Shape Memory Alloy Actuated Compliant Smart Structure: Elastica Approach," *J. Mech. Des.*, vol. 131, no. 6, pp. 61008–61011, May 2009.

[105] C. Liang and C. A. A. Rogers, "Design of Shape Memory Alloy Actuators," *J. Mech. Des.*, vol. 114, no. 2, pp. 223–230, Jun. 1992.

[106] S. Hau and S. Seelecke, "Einführung in die Aktorik mit Aktiven Materialien," *Vorlesung - Lehrstuhl für intelligente Materialsysteme, Universität des Saarlandes*. Saarbruecken, 2013.

[107] H. Schunk *et al.*, *Robot Grippers*. Weinheim: WILEY-VCH, 2007.

[108] Festo AG & Co. KG, "Basic principles of vacuum technology - brief overview." [Online]. Available: http://www.festo.com/net/SupportPortal/Files/286804/Basic_Vacuum_Technology _Principles.pdf. [Accessed: 31-Mar-2018].

[109] S. Seelecke, P. Motzki, J. Kunze, and B. Holz, "Adaptive Handhabungssysteme für Großbauteile," in *Produktivität, Qualität, Effizienz – Innovative Prozesse für die Produktion von morgen*, R. Müller and J. Flackus, Eds. Aachen, Germany: Shaker, 2015, pp. 444–463.

[110] J. Kunze, "Entwurf und Konstruktion eines FGL betätigten Vakuumgreifers zur Werkstückmanipulation," Saarland University, 2015.

[111] M. Hodgins, G. Rizzello, D. Naso, A. York, and S. Seelecke, "An electro-mechanically coupled model for the dynamic behavior of a dielectric electro-active polymer actuator," *Smart Mater. Struct.*, vol. 23, no. 10, 2014.

[112] D. Gross, W. Hauger, J. Schröder, and W. A. Wall, *Technische Mechanik 2: Elastostatik*. Springer Vieweg, 2017.

[113] G. Schuh, R. Anderl, J. Gausemeier, M. ten Hompel, and W. Wahlster, "Industrie 4.0 Maturity Index. Managing the Digital Transformation of Companies (acatech STUDY)," Herbert Utz Verlag, Munich, 2017.

[114] J. Jasperneite, "Was hinter Begriffen wie Industrie 4.0 steckt," *Computer & Automation*, Stuttgart, 2012.

[115] S. Wang, J. Wan, D. Li, and C. Zhang, "Implementing Smart Factory of Industrie 4.0: An Outlook," *Int. J. Distrib. Sens. Networks*, vol. 12, no. 1, p. 3159805, Jan. 2016.

[116] A. Radziwon, A. Bilberg, M. Bogers, and E. S. Madsen, "The Smart Factory: Exploring Adaptive and Flexible Manufacturing Solutions," *Procedia Eng.*, vol. 69, no. Supplement C, pp. 1184–1190, 2014.

[117] R. Müller, M. Vette, and O. Mailahn, "Empowering of Assembly Processes for Human-Robot-Cooperation in Terms of Task Assignment," *SAE Tech. Pap.*, vol. 2016-01-20, 2016.

[118] R. Müller, M. Vette, M. Scholer, and J. Ball, "Assembly Assistance and Position Data Feedback by Means of Projection Lasers," *SAE Tech. Pap.*, no. 2016-01-2107, 2016.

[119] Destaco, "Lightweight End Effector Tooling," 2017. [Online]. Available: http://www.destaco.com/lightweight-tooling.html. [Accessed: 10-Jan-2018].

[120] D. Hwang and T. Higuchi, "A rotary actuator using shape memory alloy (SMA) wires," *IEEE/ASME Trans. Mechatronics*, vol. 19, no. 5, pp. 1625–1635, 2014.

[121] Z. Zhakypov, J. L. Huang, and J. Paik, "A Novel Torsional Shape Memory Alloy Actuator: Modeling, Characterization, and Control," *IEEE Robot. Autom. Mag.*, vol. 23, no. 3, pp. 65–74, 2016.

[122] A. D. Johnson, "Shape memory alloy rotary actuator," US 4965545 A, 1990.

[123] J. T. Bloch, "Rotary actuator utilizing a shape memory alloy," US 4761955 A, 1988.

[124] C. C. Lan, J. H. Wang, and C. H. Fan, "Optimal design of rotary manipulators using shape memory alloy wire actuated flexures," *Sensors Actuators, A Phys.*, vol. 153, no. 2, pp. 258–266, 2009.

[125] P. Motzki, R. Britz, and S. Seelecke, "Modular SMA-Based Bi-directional Rotational Actuator," in *ASME 2016 Conference on Smart Materials, Adaptive Structures and Intelligent Systems - SMASIS16*, 2016, p. V001T04A001.

[126] R. Britz, P. Motzki, and S. Seelecke, "Rotationsaktor auf FGL-Basis," *VDI-Expertenforum: Smart Materials – kompakte, intelligente Systeme für eine innovative Industrie*. Potsdam, Germany, 2016.

[127] R. Britz, P. Motzki, and S. Seelecke, "Skalierbarer Rotationsaktor auf Basis von Formgedächtnislegierungs- drähten - Scalable SMA-based Rotational Actuator," in *Fachtagung Mechatronik 2017*, 2017, pp. 73–78.

[128] P. Motzki, F. Khelfa, L. Zimmer, M. Schmidt, and S. Seelecke, "Design and Validation of a Reconfigurable Robotic End-effector Based on Shape Memory Alloys," *IEEE/ASME Trans. Mechatronics*.

[129] P. Motzki and S. Seelecke, "Bistabile Aktorvorrichtung mit einem Formgedächtniselement," DE 10 2016 108 627 A1, 2016.

[130] P. Motzki and S. Seelecke, "BISTABLE ACTUATOR DEVICE HAVING A SHAPE MEMORY ELEMENT," WO 2017/194591 A1, 2016.

[131] P. Motzki and S. Seelecke, "Bi-stable SMA Actuator," in *Actuator 16 - 15th International Conference on New Actuators*, 2016, pp. 317–320.

[132] D. Scholtes, "Experimentelle Untersuchung von gelenkig gelagerten bistabilen Blattfedern zur Anwendung in Formgedächtnis-Aktoren," Saarland University, 2017.

[133] H. Troger and A. Steindl, *Nonlinear Stability and Bifurcation Theory*. Vienna: Springer, 1991.

[134] H. A. Mang and G. Hofstetter, *Festigkeitslehre*, 53rd ed. Berlin: Springer Verlag, 2013.

[135] G. Holzmann, H. Meyer, and G. Schumpich, *Technische Mechanik Festigkeitslehre*. Wiesbaden: Vieweg+Teubner Verlag, 2012.

[136] C. Petersen, *Stahlbau*. Wiesbaden: Springer Fachmedien, 2013.

[137] B. Camescasse, A. Fernandes, and J. Pouget, "Bistable buckled beam: Elastica modeling and analysis of static actuation," *Int. J. Solids Struct.*, 2013.

[138] B. Camescasse, A. Fernandes, and J. Pouget, "Bistable buckled beam and force actuation: Experimental validations," *Int. J. Solids Struct.*, 2014.

[139] C. Kirsch, "Entwicklung, Herstellung und Charakterisierung eines bistabilen mikromechanischen Schaltaktors in Siliziumtechnik," Saarland University, 2014.

[140] M. Vangbo and Y. Bäcklund, "A lateral symmetrically bistable buckled beam," *J. Micromechanics Microengineering*, 1998.

[141] Qualcomm, "Interferometric Modulator Technology Overview," *White paper*, 2009. [Online]. Available: https://www.qualcomm.com/media/documents/files/mirasol-imod-tech-overview.pdf. [Accessed: 30-Mar-2018].

[142] R. Vitushinsky, "Entwicklung , Herstellung und Charakterisierung von bistabilen

FGL-Dünnschichtaktoren für ein taktiles grafisches Display und mikrosystemtechnische Anwendungen," Ruhr-Universität Bochum, 2009.

[143] G. P. McKnight, "BISTABLE ACTUATOR MECHANISM," US 8,584,456 B1, 2013.

[144] G. Jobst, "Gehärteter Federbandstahl W.-Nr. 1.1274." [Online]. Available: http://www.jobst-georg.de/2016/artikel/technisch/11274.pdf. [Accessed: 30-Mar-2018].

[145] DEW-Stahl, "Werkstoffdatenblatt 1.4310," 2016. [Online]. Available: https://www.dew-stahl.com/fileadmin/files/dew-stahl.com/documents/Publikationen/Werkstoffdatenblaetter/RSH/1.4310_de.pdf. [Accessed: 30-Mar-2018].

[146] Dubbel, *Taschenbuch für den Maschinenbau*, 22nd ed. Berlin Heidelberg: Springer Verlag, 1989.

[147] P. Motzki, T. Gorges, M. Kappel, M. Schmidt, G. Rizzello, and S. Seelecke, "High-Speed and High-Efficiency Shape Memory Alloy Actuation," *Smart Mater. Struct.*, vol. 27, no. 7, p. 075047, 2018.

[148] P. Motzki, T. Gorges, T. Würtz, and S. Seelecke, "Experimental Investigation of High-Speed/High-Voltage SMA Actuation," in *ASME 2017 Conference on Smart Materials, Adaptive Structures and Intelligent Systems - SMASIS17*, 2017, p. V001T02A002.

[149] P. Motzki, T. Gorges, T. Würtz, and S. Seelecke, "Experimentelle Untersuchung von Hochvolt FGL-Ansteuerung," in *Smarte Strukturen und Systeme - Tagungsband des 4SMARTS-Symposiums 2017*, 2017.

[150] P. Motzki, T. Gorges, and S. Seelecke, "Hoch-Volt Ansteuerung: Ultraschnelle FGL-Aktorik," *VDI-Expertenforum: Smart Materials – kompakte, intelligente Systeme für eine innovative Industrie*. Potsdam, Germany, 2016.

[151] R. A. Russell and R. B. Gorbet, "Improving the response of SMA actuators," *Robot. Autom. 1995. Proceedings., 1995 IEEE Int. Conf.*, 1995.

[152] C. S. Loh, H. Yokoi, and T. Arai, "Natural Heat-Sinking Control Method for High-Speed Actuation of the SMA," *Int. J. Adv. Robot. Syst.*, vol. 3, no. 4, p. 42, Dec. 2006.

[153] J. Qiu, J. Tani, D. Osanai, Y. Urushiyama, and D. Lewinnek, "High-speed response of SMA actuators," *Int. J. Appl. Electromagn. Mech.*, 2000.

[154] R. Featherstone and Y. H. Teh, "Improving the speed of shape memory alloy actuators by faster electrical heating," *Springer Tracts Adv. Robot.*, 2006.

[155] S. J. Furst, J. H. Crews, and S. Seelecke, "Numerical and experimental analysis of inhomogeneities in SMA wires induced by thermal boundary conditions," *Contin. Mech. Thermodyn.*, vol. 24, no. 4, pp. 485–504, 2012.

[156] V. Shankar, G. N. Dayananda, P. Senthil Kumar, M. Subba Rao, and R. Balasubramaniam, "Development of electronic actuation system for shape-memory-alloy-based aerospace structures," in *SPIE, Smart Materials, Structures, and Systems*, 2003, vol. 5062, pp. 914–921.

[157] N. Ma and G. Song, "Control of shape memory alloy actuator using pulse width modulation," *Smart Mater. Struct.*, vol. 12, no. 5, p. 712, 2003.

[158] Z. Guo, Y. Pan, L. B. Wee, and H. Yu, "Design and control of a novel compliant differential shape memory alloy actuator," *Sensors Actuators A Phys.*, vol. 225, pp. 71–80, Apr. 2015.

[159] A. Ianagui and E. A. Tannuri, "A sliding mode torque and position controller for an antagonistic SMA actuator," *Mechatronics*, vol. 30, pp. 126–139, Sep. 2015.

[160] N. T. Tai and K. K. Ahn, "A hysteresis functional link artificial neural network for identification and model predictive control of SMA actuator," *J. Process Control*, vol. 22, no. 4, pp. 766–777, Apr. 2012.

[161] Y. M. Alsayed, A. A. Abouelsoud, and A. M. R. Fath El Bab, "Hybrid sliding mode fuzzy logic-based PI controller design and implementation of shape memory alloy actuator," in *2016 8th International Congress on Ultra Modern Telecommunications and Control Systems and Workshops (ICUMT)*, 2016, pp. 10–15.

[162] Z. Shi, T. Wang, D. Liu, C. Ma, and X. Yuan, "A fuzzy PID-controlled SMA actuator for a two-DOF joint," *Chinese J. Aeronaut.*, vol. 27, no. 2, pp. 453–460, Apr. 2014.

[163] T. Ross Lambert, A. Gurley, and D. Beale, "SMA actuator material model with self-sensing and sliding-mode control; experiment and multibody dynamics model," *Smart Mater. Struct.*, vol. 26, no. 3, p. 35004, 2017.

[164] A. Gurley, T. Ross Lambert, D. Beale, and R. Broughton, "Dual measurement self-sensing technique of NiTi actuators for use in robust control," *Smart Mater. Struct.*, vol. 26, no. 10, p. 105050, 2017.

[165] S. Vollach and D. Shilo, "The mechanical response of shape memory alloys under a rapid heating pulse," *Exp. Mech.*, vol. 50, no. 6, pp. 803–811, 2010.

[166] S. Vollach, D. Shilo, and H. Shlagman, "Mechanical Response of Shape Memory Alloys Under a Rapid Heating Pulse - Part II," *Exp. Mech.*, vol. 56, no. 8, pp. 1465–1475, 2016.

[167] S. Vollach, R. Caciularu, and D. Shilo, "Equilibrium stress during the response of shape memory alloys to an abrupt heat pulse," *Scr. Mater.*, vol. 141, pp. 50–53, Dec. 2017.

[168] Y. Malka and D. Shilo, "A fast and powerful release mechanism based on pulse heating of shape memory wires," *Smart Mater. Struct.*, vol. 26, no. 9, p. 095061, Sep. 2017.

Appendix: Systematic High-Speed Measurements

This appendix presents an overview of the complete systematic high-speed measurement study. Figure A.1 shows a summary of the conducted experiments. In the following, the resulting values for force, stroke and actuation time are displayed in Figures A.2-A.4.
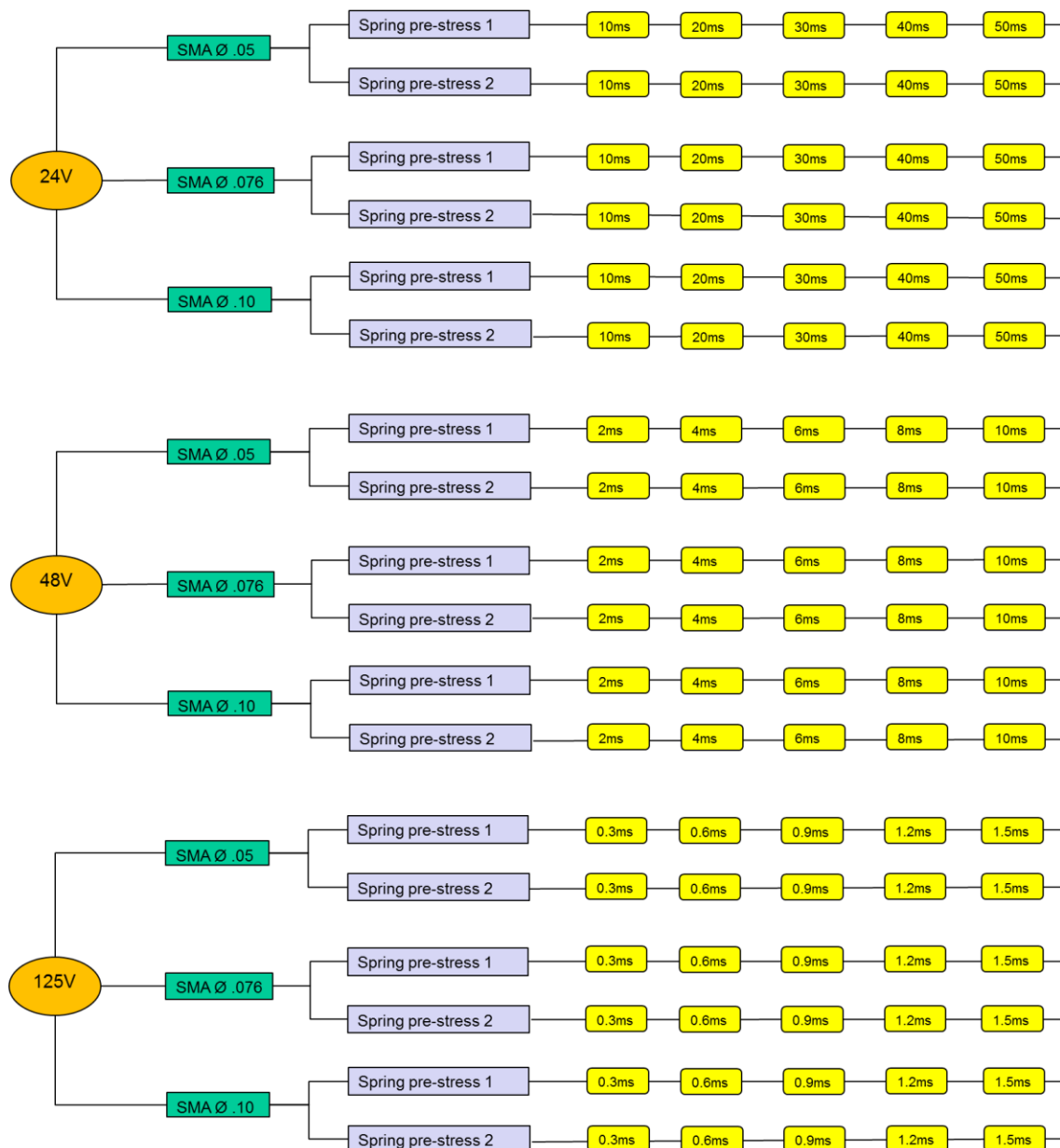
Figure A.1: Summary of the high-speed SMA activation experiments.

24V Max. Stroke

24V Max. Force

24V Time to max. Stroke

Figure A.2: Measurement results of the high-speed experiments at 24 V.

48V Max. Stroke

48V Max. Force

48V Time to max. Stroke
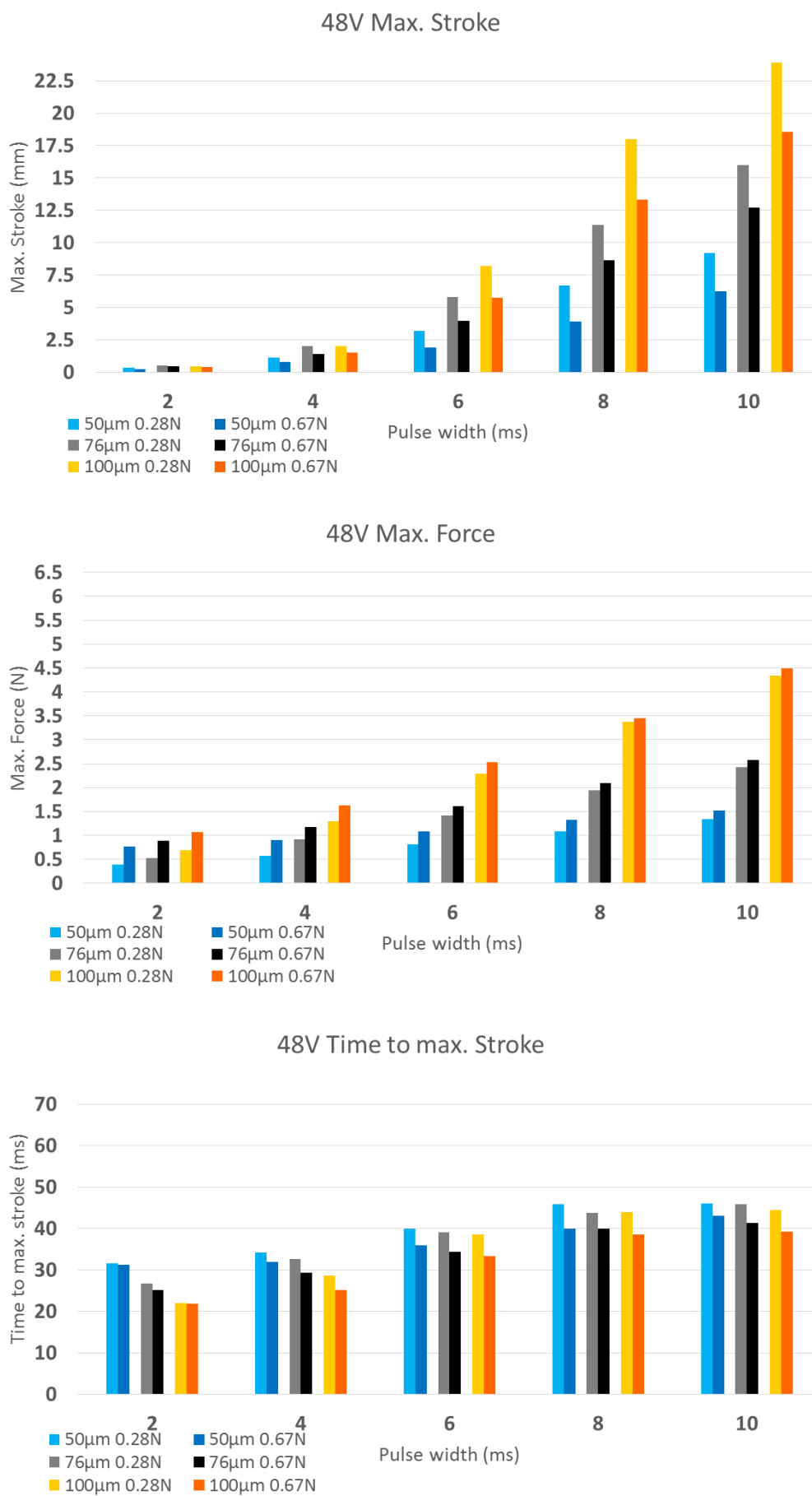
Figure A.3: Measurement results of the high-speed experiments at 48 V.

125V Max. Stroke

125V Max. Force

125V Time to max. Stroke

Figure A.4: Measurement results of the high-speed experiments at 125 V.

List of Figures

List of Tables

List of Abbreviations

CAD	computer-aided design
DOF	degree of freedom
EAP	electro-active polymer
FEM	finite element method
FSMA	ferro-magnetic shape memory alloy
M^+	martensite plus phase
M^-	martensite minus phase
MSM	magnetic shape memory (alloy)
NI	National Instruments
NiTi	nickel-titanium
PTFE	polytetrafluoroethylene (Teflon)
SMA	shape memory alloy
SME	shape memory effect

Biography

Paul Motzki was born and raised alongside his older brother Felix and younger sister Nele in Saarbrücken, Germany. At that time, Paul's mother worked as a therapist and his father was a stage actor in local and regional theaters. Growing up, athletics had always played a major role in his life. At the age of eight, Paul started to focus on fencing as his main sport and emerged as one of the top fencers in the state, which qualified him for German Championships and international tournaments. After an exchange year at Onsted High School, MI, in 11th grade, he switched his sport to American Football.

Paul graduated from Otto Hahn Gymnasium in Saarbrücken in 2007 and served his civilian service at Malteser Hilfsdienst gGmbH in the following year. In 2009, he started his studies of Mechatronics at Saarland University in cooperation with a trainee program at HYDAC INTERNATIONAL GMBH. There, he earned his BS and graduated with a MS in Mechatronics with honors in 2013.

Paul began his PhD work at Prof. Seelecke's lab in the fall of 2013 with emphasis on shape memory alloy research. In 2014, he was named starting cornerback for the German National Team in American Football and represented his country in an international game in Japan and in the European Championship Tournament in Austria, where he became European Champion. Also in the summer of 2014, he got married to his wife Stephanie, who gave birth to their first daughter Maureen Akosua in fall of the same year. In 2016, Paul became the group leader of the sector "Sensorik & Aktorik" at the Center for Mechatronics and Automation Systems (ZeMA gGmbH) and in spring of 2017, his second daughter Zola Afia was born. In the summer of 2018, Paul will defend his dissertation to earn his PhD title.

Publications

Patents

[p.1] P. Motzki and S. Seelecke, "BISTABLE ACTUATOR DEVICE HAVING A SHAPE MEMORY ELEMENT," WO 2017/194591 A1, 2016.

[p.2] P. Motzki and S. Seelecke, "Bistabile Aktorvorrichtung mit einem Formgedächtniselement," DE 10 2016 108 627 A1, 2016

Peer-reviewed Journal Papers

[j.1] P. Motzki, T. Gorges, M. Kappel, M. Schmidt, G. Rizzello, and S. Seelecke, "High-speed and high-efficiency shape memory alloy actuation," Smart Mater. Struct., vol. 27, no. 7, p. 075047, Jul. 2018.

[j.2] P. Motzki, S. Hau, M. Schmidt, and S. Seelecke, "Künstliche Muskeln und Nerven in Industrie 4.0 Konzepten - Multifunktionale Aktor-Sensor-Systeme mit Formgedächtnislegierungen und Dielektrischen Elastomeren." Industrie 4.0 Management, vol. 4, pp. 38-41, Aug. 2018.

[j.3] P. Motzki, F. Khelfa, L. Zimmer, M. Schmidt, and S. Seelecke, "Design and Validation of a Reconfigurable Robotic End-effector Based on Shape Memory Alloys." IEEE/AMSE Transactions on Mechatronics.

[j.4] S. Hau, D. Bruch, G. Rizzello, P. Motzki, and S. Seelecke, "Silicone based dielectric elastomer strip actuators coupled with nonlinear biasing elements for large actuation strains," Smart Mater. Struct., vol. 27, no. 7, p. 074003, Jul. 2018.

Book Sections

[b.1] S. Seelecke, P. Motzki, J. Kunze, and B. Holz, "Adaptive Handhabungssysteme für Großbauteile," in Produktivität, Qualität, Effizienz – Innovative Prozesse für die Produktion von morgen, R. Müller and J. Flackus, Eds. Aachen, Germany: Shaker, 2015, pp. 444–463.

[b.2] F. Simone, P. Motzki, B. Holz, and S. Seelecke, "Bio-inspirierter Drei-Finger-Greifer mit Formgedächtnisaktorik," in Technische Unterstützungssysteme, R. Weidner, T. Redlich, and J. P. Wulfsberg, Eds. Hamburg, Germany: Springer Berlin Heidelberg, 2015, pp. 194–195.

Conference Papers and Presentations

[c.1]   J. Kunze, P. Motzki, B. Holz, A. York, and S. Seelecke, "Realization of a Vacuum Gripper System Using Shape Memory Alloy Wires," in Actuator 14 - 14th International Conference on New Actuators, 2014, pp. 210–213.

[c.2] O. Mailahn, P. Motzki, R. Müller, and S. Seelecke, "Innovative Greifplanungskonzepte und rekonfigurierbare Greiftechnologie," VDI-Fachtagung Industrielle Robotik 2014. Baden-Baden, Germany, 2014.

[c.3]   P. Motzki, F. Simone, and S. Seelecke, "Shape Memory Alloy Actuators in Industrial Applications," GMA-FA 4.16 "Unkonventionelle Aktorik" im VDI/VDE-Fachbereich Mechatronik, Robotik und Aktorik, Workshop der Nachwuchswissenschaftler. VDI, Saarbrücken, Germany, 2014.

[c.4]   R. Müller, S. Seelecke, M. Vette, O. Mailahn, and P. Motzki, "Rekonfigurierbares Handhabungssystem zur Handhabung von Großbauteilen mit adaptiven Sauggreifern bestehend aus Formgedächtnislegierungen," in Bewegungstechnik 2014, 2014, pp. 117–134.

[c.5]   F. Simone, P. Motzki, B. Holz, and S. Seelecke, "Ein bio-inspirierter 3-Finger-Greifer mit Formgedächtnisaktorik - A Bio-Inspired SMA-Based 3-Finger-Gripper," in Erste transdisziplinäre Konferenz zum Thema "Technische Unterstützungssysteme, die die Menschen wirklich wollen," 2014, pp. 420–426.

[c.6]   P. Motzki, B. Holz, F. Simone, and S. Seelecke, "Formgedächtnislegierungen in Applikationen der Greif- und Handhabungstechnologie - Shape Memory Alloys in Applications of Gripping- and Material-Handling-Technology," in Fachtagung Mechatronik 2015, 2015, pp. 55–60.

[c.7]   P. Motzki, J. Kunze, B. Holz, A. York, and S. Seelecke, "Adaptive and Energy efficient SMA-based Handling Systems," in SPIE - Active and Passive Smart Structures and Integrated Systems 2015, 2015, vol. 9431, p. 943116.

[c.8]   S. Nalbach, P. Motzki, and S. Seelecke, "SMA-BASED HYDRAULIC SWITCHING VALVE," in ASME 2015 Conference on Smart Materials, Adaptive Structures and Intelligent Systems - SMASIS2015, 2015, p. V002T04A006.

[c.9]   R. Britz, P. Motzki, and S. Seelecke, "Rotationsaktor auf FGL-Basis," VDI-Expertenforum: Smart Materials – kompakte, intelligente Systeme für eine innovative Industrie. Potsdam, Germany, 2016.

[c.10] P. Motzki, T. Gorges, and S. Seelecke, "Hoch-Volt Ansteuerung: Ultraschnelle FGL-Aktorik," VDI-Expertenforum: Smart Materials – kompakte, intelligente Systeme für eine innovative Industrie. Potsdam, Germany, 2016.

[c.11] P. Motzki, R. Britz, and S. Seelecke, "Modular SMA-Based Bi-directional Rotational Actuator," in ASME 2016 Conference on Smart Materials, Adaptive Structures and Intelligent Systems - SMASIS16, 2016, p. V001T04A001.

[c.12] P. Motzki, Y. Goergen, A. York, and S. Seelecke, "Reconfigurable SMA End-effector for Material Handling," in Actuator 16 - 15th International Conference on New Actuators, 2016, pp. 522–525.

[c.13] P. Motzki, J. Kunze, A. York, and S. Seelecke, "Energy-efficient SMA Vacuum Gripper System," in Actuator 16 - 15th International Conference on New Actuators, 2016, pp. 526–529.

[c.14] P. Motzki and S. Seelecke, "Bi-stable SMA Actuator," in Actuator 16 - 15th International Conference on New Actuators, 2016, pp. 317–320.

[c.15] P. Motzki, S. Nalbach, and S. Seelecke, "Hydraulisches Schaltventil mit FGL-Draht Aktoren," in Smarte Strukturen und Systeme - Tagungsband des 4SMARTS-Symposiums, 2016, pp. 296–307.

[c.16] R. Britz, P. Motzki, and S. Seelecke, "Skalierbarer Rotationsaktor auf Basis von Formgedächtnislegierungs- drähten - Scalable SMA-based Rotational Actuator," in Fachtagung Mechatronik 2017, 2017, pp. 73–78.

[c.17] M. Brill, P. Loew, P. Motzki, and S. Seelecke, "Entwicklung eines FGL basierten smarten Positionierungsaktors," in Smarte Strukturen und Systeme - Tagungsband des 4SMARTS-Symposiums 2017, 2017, pp. 269–278.

[c.18] P. Motzki, T. Gorges, T. Würtz, and S. Seelecke, "Experimentelle Untersuchung von Hochvolt FGL-Ansteuerung," in Smarte Strukturen und Systeme - Tagungsband des 4SMARTS-Symposiums 2017, 2017.

[c.19] F. Khelfa, L. Zimmer, P. Motzki, and S. Seelecke, "Development of a Reconfigurable End-Effector Prototype," in ASME 2017 Conference on Smart Materials, Adaptive Structures and Intelligent Systems - SMASIS17, 2017, p. V002T04A011.

[c.20] P. Motzki, T. Gorges, T. Würtz, and S. Seelecke, "Experimental Investigation of High-Speed/High-Voltage SMA Actuation," in ASME 2017 Conference on Smart Materials, Adaptive Structures and Intelligent Systems - SMASIS17, 2017, p. V001T02A002.

[c.21] S.-M. Kirsch, F. Welsch, M. Schmidt, P. Motzki, and S. Seelecke, "Bistable SMA Vacuum Suction Cup," in Actuator 18 - 16th International Conference on New Actuators, 2018.

[c.22] S. Lenz, B. Holz, S. Hau, P. Motzki, and S. Seelecke, "Development of a High Voltage Source for Dielectric Elastomer Actuators (DEA)," in Actuator 18 - 16th International Conference on New Actuators, 2018.

[c.23] P. Linnebach, S. Hau, G. Rizzello, P. Motzki, and S. Seelecke, "Stroke Magnification in Dielectric Elastomer Actuators with Dynamic Excitation," in Actuator 18 - 16th International Conference on New Actuators, 2018.

[c.24] D. Bruch, M. Hill, S. Hau, P. Motzki, and S. Seelecke, "Electromechanical Fatique Testing Device for Dielectric Elastomers under Controllable Environmental Conditions," in Actuator 18 - 16th International Conference on New Actuators, 2018.

[c.25] L. Zimmer, Y. Goergen, F. Khelfa, M. Schmidt, P. Motzki, and S. Seelecke, "Development and Control of a 2-DOF Reconfigurable SMA End-effector," in Actuator 18 - 16th International Conference on New Actuators, 2018.

[c.26] D. Scholtes, R. Zäh, M. Schmidt, P. Motzki, B. Faupel, and S. Seelecke, "Resistance Welding of NiTi Actuator Wires," in Actuator 18 - 16th International Conference on New Actuators, 2018.

[c.27] R. Britz et al., "SMA Wire Bundles – Mechanical and Electrical Concepts," in Actuator 18 - 16th International Conference on New Actuators, 2018.

Eidesstattliche Versicherung

Hiermit versichere ich an Eides statt, dass ich die vorliegende Arbeit selbstständig und ohne Benutzung anderer als der angegebenen Hilfsmittel angefertigt habe. Die aus anderen Quellen oder indirekt übernommenen Daten und Konzepte sind unter Angabe der Quelle gekennzeichnet. Die Arbeit wurde bisher weder im In- noch im Ausland in gleicher oder ähnlicher Form in einem Verfahren zur Erlangung eines akademischen Grades vorgelegt.

Ort, Datum

_____

Unterschrift

_____